Università degli Studi di Ferrara

DOTTORATO DI RICERCA
in FISICA

CICLO XXX

COORDINATORE Prof. GUIDI Vincenzo

Search for hidden-strangeness pentaquark in $\Lambda_c \to p\phi\pi^0$ at BESIII.

Settore Scientifico Disciplinare FIS/04

Tutore
Dott. Bettoni Diego

Dottorando
Dott. Mezzadri Giulio

Co-Tutore
Dott. Cibinetto Gianluigi

Anni 2014/2017

Contents

List of Figures

List of Tables

Abstract

The observation of the elusive parts of the Quark Model helps to shed more light on the non-perturbative part of the Quantum Chromodynamics (QCD). In fact, our understanding of the strong interaction at its maximum strength relies on the development of more precise effective field theories. The larger is the part of the experimental spectrum unveiled, the higher is the precision of these theories can reach.

The search for bound states with structures more complicated than standard mesons and baryons is one of most active fields in high energy physics. Even if most of such states are expected since the first days of the Quark Model, there are no clear indication of their existence. In the past decades several candidates that can be interpreted with the possible exotic combinations (tetraquarks, pentaquarks, glueballs) were found. More indications are coming, and one of the most vital goals is to try to make connections between these states, in order to create a new spectroscopy. The hunt for these states is being entrusted to the flavour-factories, either in the bottomonium sector (BELLE, BELLE-II, and BaBar) or in $\tau-charm$ one (BESIII), and at the hadrons collider (LHCb, and in the future $\bar{\text{P}}$ANDA) and the photoproduction one (GLUEX, CLAS12).

Among all the exotics, pentaquark candidates seem to be more elusive particles. The only two candidates that fit the 5 quarks pictures are the ones observed by LHCb Collaboration [1]. LHCb reported two structures in the pJ/ψ invariant mass, studying the decay $\Lambda_b \to pJ/\psi K^-$, as shown in Fig. 1.

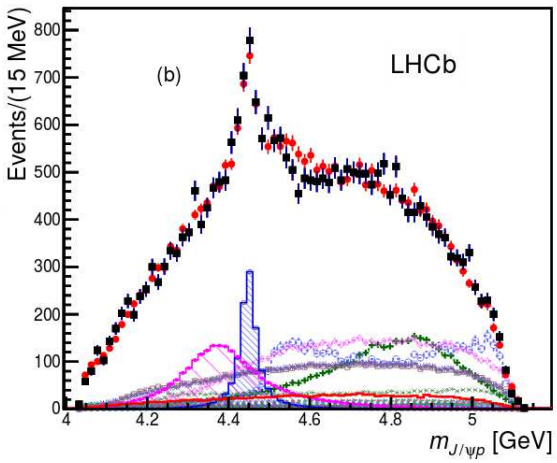

Figure 1: Invariant mass of pJ/ψ in the partial wave analysis done by LHCb collaboration, taken from Ref. [1]. The shaded blue and magenta histograms represent the two pentaquark candidates

A natural step forward in understanding the nature of such states is to search for partners in other flavour sectors. Recently, a model was proposed by R.F. Lebed [2], in which the possibility to search for hidden-strangeness pentaquark siblings in the decay of $\Lambda_c \to p\phi\pi^0$, with the pentaquark emerging in the $p\phi$ pair invariant mass is shown. A second model was then proposed by Xie and Guo [3] to investigate the dynamics of such decay; in this work it is shown that the presence of opening of thresholds can create triangular singularities, that can mask the presence of the possible pentaquark candidates.

The aim of this work is to search for exotic hidden-strangeness pentaquarks with BESIII data. BESIII experiments is a central detector optimized for τ and *charm* physics. In 2014 the experiment has collected a sample of data at the $\Lambda_c\bar{\Lambda}_c$ baryon threshold thanks to the upgraded center-of-mass energies of the lepton collider BEPCII.

The work is divided in two parts. The first part will be a general introduction to exotic multiquarks states and is organized as follows: in Chapter 1, a review of the Quark Model, the construction of the hadrons, and general aspects of the lagrangian of QCD will be presented. In Chapter 2 a brief review of the known experimental results on the exotic multiquark candidates and a description of the recent model to extend the pentaquark picture to the strange sector will be discussed. In the second part, the focus will be on BESIII data analysis: in Chapter 3 a detailed description of the BESIII detector will be done. Chapter 4 will show the BESIII capabilities to fullfill its own wide scientific program. Chapter 5 will describe the analysis of the $567\,\mathrm{pb}^{-1}$ data collected at $\Lambda_c\bar{\Lambda}_c$ baryon pair threshold and the discussion of the obtained results and the implication on the present knowledge of hidden-strangeness pentaquarks.

Part I

Introduction to the exotic multiquark states

Chapter 1

Quark model and QCD lagrangian

The forces of nature are described by relativistic quantum field theories that predict the interactions among the matter constituents, that can be tested in experimental observations. Quantum Chromodynamics (QCD) is the well-accepted theory to describe the strong interaction and is used to describe the dynamics of quarks and gluons. Both quarks and gluons are color-charged; this feature complicates the description of the dynamics more than in the case of the Quantum ElectroDynamics (QED).

Particles that interact via the strong force are called hadrons. However, the QCD lagrangian does not explain how these particles bind. This is described with an impressive good agreement by the Quark Model, an effective theory developed by Gell-Mann [4] and Zweig [5]. Based on the group theory approach, this model describes the hadrons in terms of pointlike constituents called quarks. With this model, in the hypothesis of three quarks (u, d and s) they were able not only to arrange the already observed particle in multiplets based on the spins, but also to predict the masses of new states.

In this first chapter, a brief review of the QCD features and of the Quark Model will be presented. This introduction is aimed to point out the successes of the theories and to act as a bridge towards the experimental observations that started to appear from the beginning of the new century.

1.1 Quark Model

After the first mesons observations, and especially after the discovery of the Λ baryon, it became clear that all observed particles can be organized following some simple rules. This is the origin of the Quark Model, developed by Gell-Mann and Zweig in 1964. The underlying idea is that the observed particles consist of more fundamental elements.

These objects must be fermions with baryon number $B = 1/3$. These objects were called *quarks* in the Gell-Mann paper, while Zweig identified them with the name *aces*. Hereafter they will be referred to as quarks, as they are called nowadays.

The original Quark Model is built around the SU(3) symmetry group, of which the 3 quarks are the fundamental triplet. These three quarks are identified as $u^{\frac{2}{3}}$, $d^{-\frac{1}{3}}$ and $s^{-\frac{1}{3}}$, where the superscript represents the charge. This SU(3) symmetry is nowadays called flavor SU(3) (or $SU(3)_F$) not to be confused with the color SU(3), that is the symmetry group of QCD. The charge of the quarks is related to the third component of the isospin and the baryon number:

$$Q/e = \frac{1}{2}(B + S) + I_z \tag{1.1}$$

where B is the baryon number, S is the strangeness quantum number, defined to be $S = -1$ for the strange quark, and I_z that is the third component of the isospin, that is $I_z = +1/2$ for the u quark, $I_z = -1/2$ for the d and $I_z = 0$ for the s quark. With these quantum number assignments the quarks turn out to have fractional electric charge.

Even if the Quark Model was able to reproduce the known particle masses and spins with very good accuracy, there was no direct experimental evidence in the data of the existence of quarks, until the first deep inelastic scattering experiments, which showed that the nucleons appear to be built by quasi-free, light pointlike constituents (partons). It became clear quite soon that the quarks can be identified with the partons.

1.1.1 Building the observed spectra

Starting from the three quarks and following the relationship between charge, isospin and strangeness of Eq. 1.1 it is possible to build the spectrum of the observed particles. The minimal quark combinations to reproduce the spectra are $q_1q_2q_3$ for the baryons and $q_1\bar{q_2}$ for the mesons, where the subscript indicates one of the possible flavors. The core of the quark model is the multiplets structure.

For a meson it is possible to determine the parity P of the state as $P = (-1)^{l+1}$ For the neutral mesons it is possible to determine the charge conjugation C, defined as $C \equiv (-1)^{l+s}$ where l and s are the orbital angular momentum and spin of the $q\bar{q}$ pair. The meson spin J is the total angular momentum defined using the conventional relation $|l - s| < J < |l + s|$.

In the following two subsections we are going to build the conventional mesons and baryons. This exercise is quite simple, but it is useful to show the features of the conventional hadrons.

Mesons

Mesons have baryon number $B = 0$. Following the $SU(3)_F$ algebra,

$$\mathbf{3} \otimes \bar{\mathbf{3}} = \mathbf{8} \oplus \mathbf{1}$$

i.e. the combination of three quarks and three antiquark produces a flavor octet and a flavor singlet. Combinations with different spin alignment and angular momentum between the quark-antiquarks pair produce the different multiplets, as shown in Fig. 1.1a and Fig. 1.1b in which the pseudoscalar and the vector mesons composed of light quarks are shown respectively.

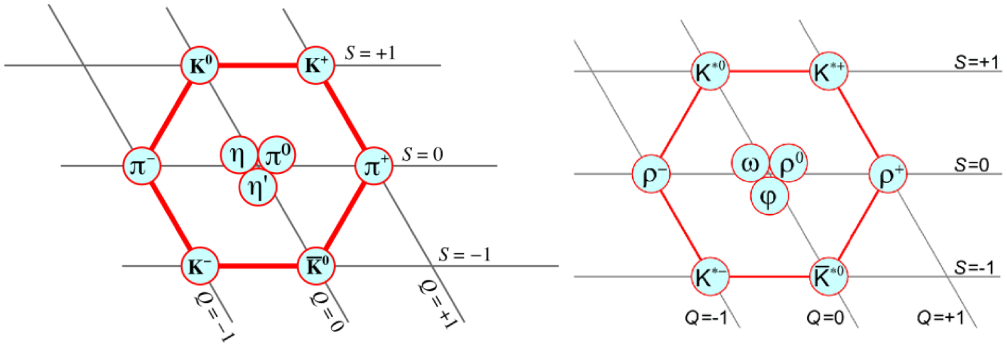

(a) Pseudoscalar meson multiplet.

(b) Vector meson multiplet.

Figure 1.1: Meson octets.

Baryons

To build a baryon, it is necessary to combine three quarks: using the $SU(3)_F$ algebra

$$\mathbf{3} \otimes \mathbf{3} \otimes \mathbf{3} = \mathbf{10}_S \oplus \mathbf{8}_M \oplus \mathbf{8}_M \oplus \mathbf{1}_A$$

so that the combination of three quarks in three flavors gives an anti-symmetric flavor singlet, two mixed-symmetric flavor octets, and one symmetric flavor decuplet. The symmetric decuplet is shown in Fig. 1.2.

The decuplet shows an interesting feature: the $J = 3/2$ Ω^- baryon has a fully symmetrical spin structure, fully symmetrical orbital wave and fully symmetrical flavor structure. This violates the Pauli principle: the three quarks are exactly in the same quantum state. This means that an additional contribution must be present: this was solved by Han and Nambu in Ref. [6] by adding another SU(3) triplet. This new triplet shall be in an anti-symmetric configuration. In this new picture, the three quarks of the Ω^- baryon are not anymore in the same state, thus the Pauli principle is conserved. With respect

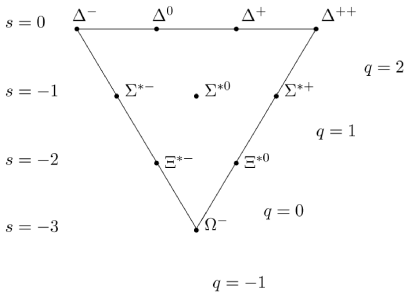

Figure 1.2: Baryon decuplet multiplet.

to this new symmetry, all particles must form a neutral combination, since there is no experimental evidence of this additional quantum number. This model was verified in the experimental measurement of the total cross section for $e^+e^- \to$ hadrons: data were consistent with the existence of three additional degrees of freedom. The original idea of Han and Nambu is at the origin of the color degree of freedom and thus of QCD, whose features will be discussed later.

1.1.2 Hadron masses

If the $SU(3)_F$ were an exact symmetry, each state in the same multiplet should have the same mass. Instead, the flavor SU(3) is just approximate: taking as example the vector mesons, the mass of the ω meson and the ρ meson are similar ($m_\omega \sim m_\rho = 0.78\,\mathrm{GeV}/c^2$), but they quite differ from the K^* meson one ($m_{K^*} = 0.89\,\mathrm{GeV}/c^2$) and the ϕ meson ($m_\phi = 1.02\,\mathrm{GeV}/c^2$).

The proposed model implies that the hadron masses are built entirely by the sum of the constituent quark masses. In this way the broken flavor symmetry, for which the s quark is heavier than the u and d, can justify some differences. This seems to be a good explanation, since $m_p(uud) \sim 3m_{u,d}$ and $m_\Sigma(uds) \sim 2m_{u,d} + m_s$. However this model cannot explain the mass difference of the Δ^+ baryon ($m_\Delta = 1232\,\mathrm{MeV}/c^2$) and the proton ($m_p = 938.27\,\mathrm{MeV}/c^2$). This issue is present also in the meson sector, for the case of ρ meson and π meson ($m_\pi = 139.57\,\mathrm{MeV}/c^2$). The only difference between the heavier (Δ baryon, ρ meson) and the lighter (proton, π meson) is the value of total angular momentum. Thus, the quark-quark interactions modify the mass of the hadron. In analogy with the hydrogen atom it is possible to construct an hyperfine correction to the hadron masses. In this scheme the hadron masses can be written as

$$m(q_1\bar{q}_2) = m_1 + m_2 + \frac{a}{m_1 m_2}\overrightarrow{\sigma}_1 \cdot \overrightarrow{\sigma}_2$$

$$m(q_1 q_2 q_3) = m_1 + m_2 + m_3 + \frac{a'}{2}\sum_{i>j}\frac{\overrightarrow{\sigma}_i \cdot \overrightarrow{\sigma}_j}{m_i m_j}$$

where m_i is the mass of the constituent quarks ($i = 1, 2, 3$) for the baryons, $i = 1, 2$ for the mesons), σ_i is the spin of the quark i and a and a' are the correction factors that shall be determined with experimental data.

The spin-spin correction almost justifies all the differences. There exists another contribution to explain the difference between the proton and the neutron mass. The difference comes from the isospin symmetry breaking of the electromagnetic interaction. This is a small effect that is due to the little difference between the mass of the u and the d, and this is why the neutron is slightly heavier than the proton.

1.1.3 Charmonium spectrum

In order to better understand why the states that are the main topic of this work are called exotic, it is useful to introduce a description of the conventional charmonium spectrum: only by excluding any possible conventional explanation is it possible to determine the exotic nature of those states.

The charmonium system was discovered in 1974, when almost simultaneously two experiments, at Brookhaven and SLAC, announced the discovery of a very narrow state, called J and ψ respectively. The observation of a second state narrow state by SLAC followed immediately. This resonance was interpreted as bound state of a new quark, the charm (c) and its anti-quark ($\bar{c}$): the existence of this new constituent quark was predicted several years before by Glashow, Iliopoulos and Maiani [7] to explain the absence of flavor changing neutral currents. The high mass of the c quark ($m_c \approx 1.5\,\mathrm{GeV}/c^2$) allows to attempt a description of the dynamical properties of the $c\bar{c}$ in terms of non-relativistic potential models. The potential used follows the properties of QCD (that will be detailed in Sec. 1.2.1), and the free parameters are determined by the comparison with the experimental measurements.

However, the potential model can only describe the basic features of the charmonium spectrum. It has been shown by Godfrey and Isgur [8] that the relativistic corrections are generally important. Moreover, it has become manifest that the presence of open charm threshold can modify the spectrum: these effects are frequently called coupled channel corrections [9]. Recently, the Non Relativistic QCD (NRQCD) [10] effective field theory has achieved great progress in the description of the spectrum and the decay properties.

1.1.4 Extension to a generalized multiflavor model

After the discovery of the J/ψ it is necessary to extend the quark model to the other quark quantum numbers. The extension is quite straightforward. To express the new quark charges it is possible to use the Eq. 1.1 and extend it to the generalized Gell-Mann-Nishijima formula:

$$Q/e = I_z + \frac{\mathcal{B} + S + C + B + T}{2}$$

where, C represents the charm quantum number, B represents the bottomness quantum number, T the topness quantum number.

The schematic representation of the multiplets with the addition of the charm quark, it is illustrated in Fig. 1.3a and Fig. 1.3b.

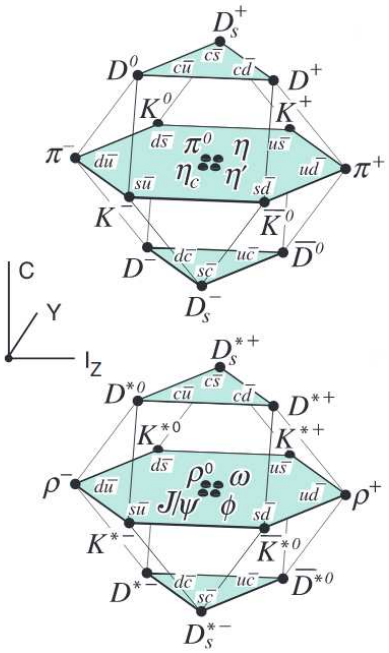

(a) Meson octets with the addition of the quark charm. (top) Pseudoscalar mesons. (bottom) Vector meson.

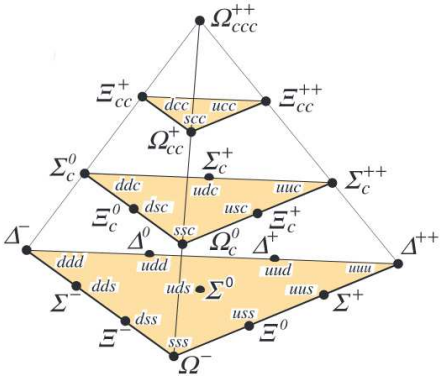

(b) Baryon decuplet with the addition of the quark charm.

Figure 1.3: Extended quark model mesons and baryons. The axis represents the charm quantum number C, the hypercharge Y and the third components of the isospin I_z.

1.2 An introduction to the features of the QCD

Quantum ChromoDynamics (QCD) is a gauge field theory that describes the strong interaction by means of the color-charged gluons and quarks and represents the SU(3) component of the SU(3) × SU(2) × U(1) Standard Model of Particle Physics.

The QCD lagrangian is given by

$$\mathcal{L} = \sum_q \bar{\psi}_{q,a}(i\gamma^\mu \partial_\mu \delta_{ab} - g_s \gamma^\mu t^C_{ab} \mathcal{A}^C_\mu - m_q \delta_{ab})\psi_{q,b} - \frac{1}{4} F^A_{\mu\nu} F^{A\,\mu\nu}$$

where repeated indices are summed over. The γ^μ are the Dirac γ-matrices. The $\psi_{q,a}$ are quark field spinors for a quark of flavor q and mass m_q. The color-index a runs from 1 to $N_c = 3$, where N_c is the number of colors. This degree of freedom is called color, in analogy with the three color (R, G, B) with which you can build images. Each quark can appear in one of the three colors that is the same degree of freedom predicted by Han and Nambu. The m_q, that appears in the lagrangians, are not the masses of the constituent quarks, that are approximate degree of freedom to justify the data. The m_q are called *bare* quark masses and are one of the parameters of the Standard Model that need to be extracted from data. Indication of the nature of the constituent masses can be found considering spontaneous and explicit breaking of the chiral symmetry of the QCD lagrangian. More details can be found in Ref. [11] and Ref. [12].

The $\mathcal{A}^C_\mu$ are the gluon terms, with C running from 1 to $N_c^2 - 1 = 8$, that is the number of the adjoint representation of $SU(3)$ color group: this means that there are eight gluon fields. The t^C_{ab} are eight 3×3 matrices that generates the rotation in SU(3): the interaction between a quark and a gluon rotates the charge color from the state a to the state b. g_s is the coupling constant of the QCD and together with the quark masses is one of the fundamental parameters of the QCD, that cannot be predicted from first principles but only extracted from the experiments.

The term $F^A_{\mu\nu}$ encodes the dynamics of the gluons fields and is given by:

$$F^A_{\mu\nu} = \partial_\mu \mathcal{A}^A_\mu - \partial_\nu \mathcal{A}^A_\mu - g_s f_{ABC} \mathcal{A}^B_\mu A^C_\nu$$

where the relation $[t^A, t^B] = i f_{ABC} t^C$ is satisfied when the f_{ABC} are the structure constants of the SU(3) group: these are due to the non-abelian structure of SU(3). This feature will influence also an important characteristic of the QCD: the confinement. This will be discussed later in more details in Sec. 1.2.1.

There is no experimental evidence of free colored quarks or gluons: so far, they bound together to form color-singlet (hadrons). It is possible to calculate the Feynman rules starting from the lagrangian. In particular, three different vertices appear:

- the quark-antiquark-gluon vertex (proportional to $\sqrt{g_s}$),
- the 3-gluons vertex (proportional to g_s)
- the 4-gluons vertex (proportional to g_s^2)

that are depicted in Fig. 1.4. The first vertex is similar to the one that appears in the Quantum ElectroDynamics (QED), while the other two are the results of the non-abelian algebra of SU(3) and thus do not appear in QED. This effect can be explained by the fact that gluons, unlike photons, carry a color charge: thus, they can interact with each other.

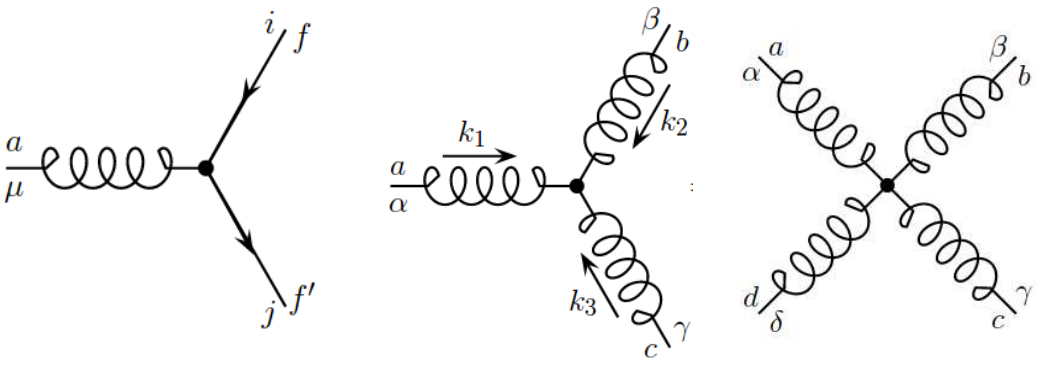

(a) Quark-Antiquark-gluon vertex.

(b) 3 gluons vertex.

(c) 4 gluons vertex.

Figure 1.4: QCD vertices that can be extracted from the lagrangian.

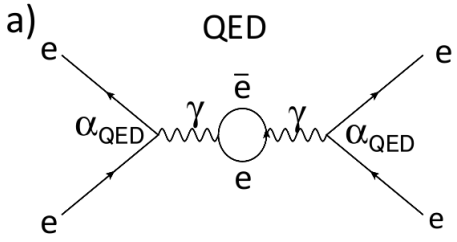

Figure 1.5: Vacuum polarization contribution in QED at first perturbative order.

1.2.1 Running coupling constant and confinement

In the pure QCD lagrangian description loops give divergent contributions, similarly to QED. They appear in vertices and in the boson propagator. In QED there is only one diagram that contributes at first order to the vacuum polarization in the propagator of the photon and it is shown in Fig. 1.5. The issue of the infinities in the loops was masterly solved by a mechanism that it is now called renormalization: the coupling constant becomes function of a nonphysical parameter. In this way, the divergent contribution can be cut-off from the calculations. The introduction of a scale results in a modification of the coupling strength at different values of this scale. In the QED example, the QED coupling constant at low energies is $\alpha_{QED} \sim 1/137$, while at the peak of the Z^0 this value is $\alpha_{QED} \sim 1/125$. The coupling strength increases as the energy scale increases.

In QCD, the possible contributions to the gluon propagator are two: the first one is the analogous of the QED term, while the second is due to the gluon-gluon interaction as shown in Fig. 1.6.

The coupling strength ($\alpha_s = \frac{g_s^2}{4\pi}$) as a function of the energy scale (μ_R) can be calculated

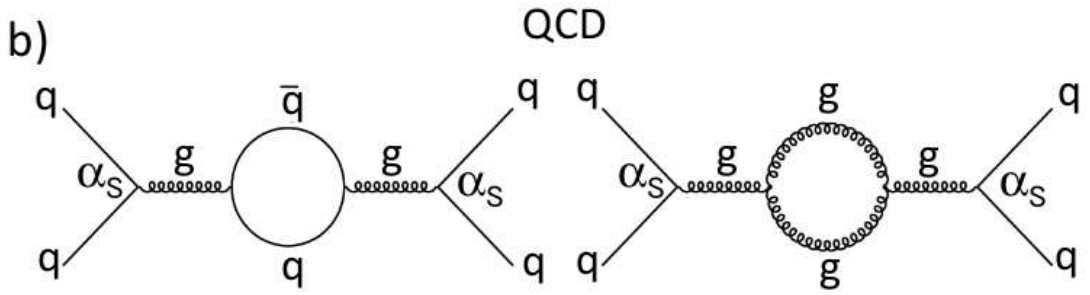

Figure 1.6: Vacuum polarization contribution in QCD at first perturbative order. (Left) A quark-antiquark loop in the gluon propagator. (Right) Two gluons loop.

using a simple formula

$$\mu_R^2 \frac{d\alpha_s}{d\mu_R} = \beta(\alpha_s) = -(b_0 \alpha_s^2 + \cdots)$$

where $b_0 = (11C_A - 4n_f T_R)$ is the 1-loop coefficient, $C_A \equiv N_c = 3$ is the color factor associated with gluon emission from a gluon and $T_R = 1/2$ is the color factor for a gluon to split to a $q\bar{q}$ pair, and n_f is the number of flavors accessible at the energy scale considered. The most characteristic feature is the minus sign, which is due to the second contribution in Fig. 1.6: this indicates that the coupling strength in QCD decreases at higher energies (*e.g.* $\alpha_s = 0.1185$ at the energy of the Z^0; $\alpha_s \sim= 0.4$ at the 1 GeV). This feature is called asymptotic freedom: in high energy processes it is possible to consider the quarks and gluons as free during the interaction, thus the rule of the perturbation theory well tested in QED can be also be applied for QCD. This is the basis of what is called perturbative QCD.

On the other hand, for very low energies, the coupling constant becomes so large that any perturbative approach becomes unfeasible. This effect is called confinement and it is the source of the binding of quarks and gluons inside the hadrons.

The mathematical expression of QCD potential takes into consideration both confinement and asymptotic freedom and it is usually defined as

$$V(r) = -\frac{4\alpha_s}{3r} + \sigma r$$

where the first term represents the asymptotic freedom and the second term takes into consideration the confinement effect.

1.2.2 Effective field theory and Lattice QCD

The QCD lagrangian gives precise prescriptions of the interaction of quarks and gluons. The perturbative approach, that works fine for the high energy regime, cannot work in the low-energy regime, since the higher terms of the perturbative expansion give larger (and larger) contributions with respect to the first order calculation. Potential models, like the one used to describe the charmonium spectrum, have become less predictive, as it will be shown in the next chapter.

In order to calculate the properties of hadrons directly from the QCD in the non-perturbative regime only two ways remain viable. On one side, it is possible to constrain the interaction on a lattice. In Lattice QCD [13], there are no approximations except for the masses of hadrons, especially pions: this is the closest approach to the QCD lagrangian available to describe the data. On the other hand, it is possible to add approximations at the full lagrangian and thus be able to describe the available data: the theory will be valid only in a precise energy spectrum, and extensions can become more complicated. These theories are called effective theories. Some examples are the cited NRQCD, or the HQEFT [14]. A review of some of the effective theories available for the exotic states is presented in Appendix A.

1.3 Outlook on QCD and Quark model

While the successes of the perturbative QCD are many (Deep inelastic scattering, jets description), the non-perturbative part of the QCD is hopelessly complicated to be calculated from the first principles: in recent years, the advent of the Lattice QCD has brought chance that in a (not so far) future we will be able to shed new light on the mysteries of the strong interaction at its maximum strength.

The composition of hadrons in terms of quarks and gluons is even more complicated: the quark model has surely brought a clear picture in the zoo of the particles. On the other hand, there are unsolved puzzles: for example the positive parity of the $N^*(1440)$ (the Roper resonance) [15] or the mass of the lowest-lying excitation of the Λ hyperon, the $\Lambda(1405)$.

Waiting for the Lattice QCD to develop interesting values for the physical variables (the typical pion mass used in the lattice is three times the physical one), we are left with effective theories to describe the features of the non perturbative QCD. These models provide good understanding of a particular energy regime, but fail when they try to describe the whole picture. As experimentalists, our role is to search for new particles and measure their properties, decays and transitions to enlighten new patterns that may help guide the refinement of these theoretical models. This is the case for the experimental observation of the exotic multiquarks, tetraquarks and pentaquarks. This series of observations will be discussed in the next chapter.

Chapter 2

Experimental observations

The discovery or the observation of one single state is a great result per se, even though it has not to be the final objective: the final goal is to deepen the knowledge of QCD, especially in the non-perturbative regime, in order to refine our knowledge of the features of the strong interaction. The field of the exotic searches is very broad, and a full review is beyond the scope of this thesis. For such extended review, it is possible to look in Ref. [16] and Ref. [17]. Instead, the aim of this part is to provide the background to which the search for hidden-strangeness belongs.

In order to understand the complexity of the hadron spectroscopy in recent years, recent pictures of the charmonium and bottomonium spectroscopic lines and the known transition among them taken from Ref. [16] are shown in Fig. 2.1 and Fig. 2.2 respectively.

A difference arises from the figures: while the charmonium spectrum flourish of exotics, called XYZ states, we do not have many counterparts in the bottomonium spectrum. This is mainly due to the fact that our knowledge of the spectrum above $B\bar{B}$ threshold is limited, due to the difficulty to increase the center of mass energy at the B-factories or to extrapolate information for these states from very high energy collider experiments.

On the other hand, the relative lightness on the strange quark allows to copiously produce the states with strangeness in many accelerators. Search for hidden and open strangeness counterpart of the exotic discovered in the charmonium spectrum can be used to test the present knowledge of the theoretical models in a energy region in which the mass of the constituent is comparable with Λ_{QCD}.

In the next sections, the aim is to point out some features of the XYZ states. The attention will be focused on those states with known transition between each other, in order to enlighten connections among these different states and thus to deepen our knowledge of the strong interaction. The review will cover the $X(3872)$, the $Y(4260)$, the $Z_c(3900)^+$ and onto the bottom counterpart the Y_b and the Z_bs. The $Z(4430)^+$, that

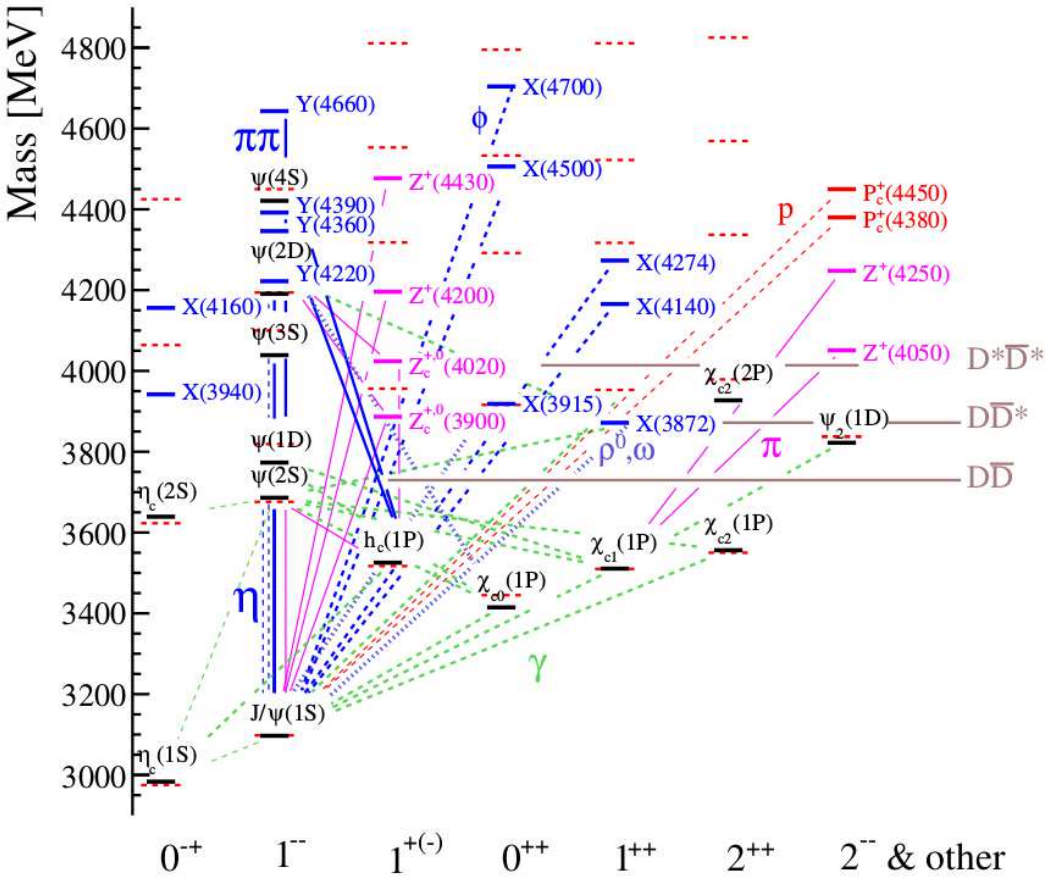

Figure 2.1: The charmonium and charmonium-like spectrum taken from Ref. [16]. The states are organized as follows: the black lines represent the experimentally established conventional charmonia, while the red dashed lines represent the mass extracted from a recent calculation [18] based on the Godfrey-Isgur potential [8]. The exotic charmonium-like states are in blue (neutral states)) and magenta (charged states). Solid brown lines represent the thresholds for the open charm production. The possible transitions are presented as dashed-green (electromagnetic E1 and M1), solid-magenta (π), solid-blue ($\pi\pi$), dashed-red (proton), dashed-blue (η or ϕ) lines. States without an established J^{PC} and pentaquarks are placed in the last column, while all other states are in the respective J^{PC} spectroscopy assignment column.

is the first confirmed tetraquark structure, observed by Belle [19] in the $B \to \psi(2S)\pi K$ in the $\psi(2S)\pi$ invariant mass and later by LHCb [20] and not excluded by BaBar [21], will not be discussed since there is no observed connection between this state and other exotics.

The last part of this chapter will be used to discussed in details the pentaquarks' observa-

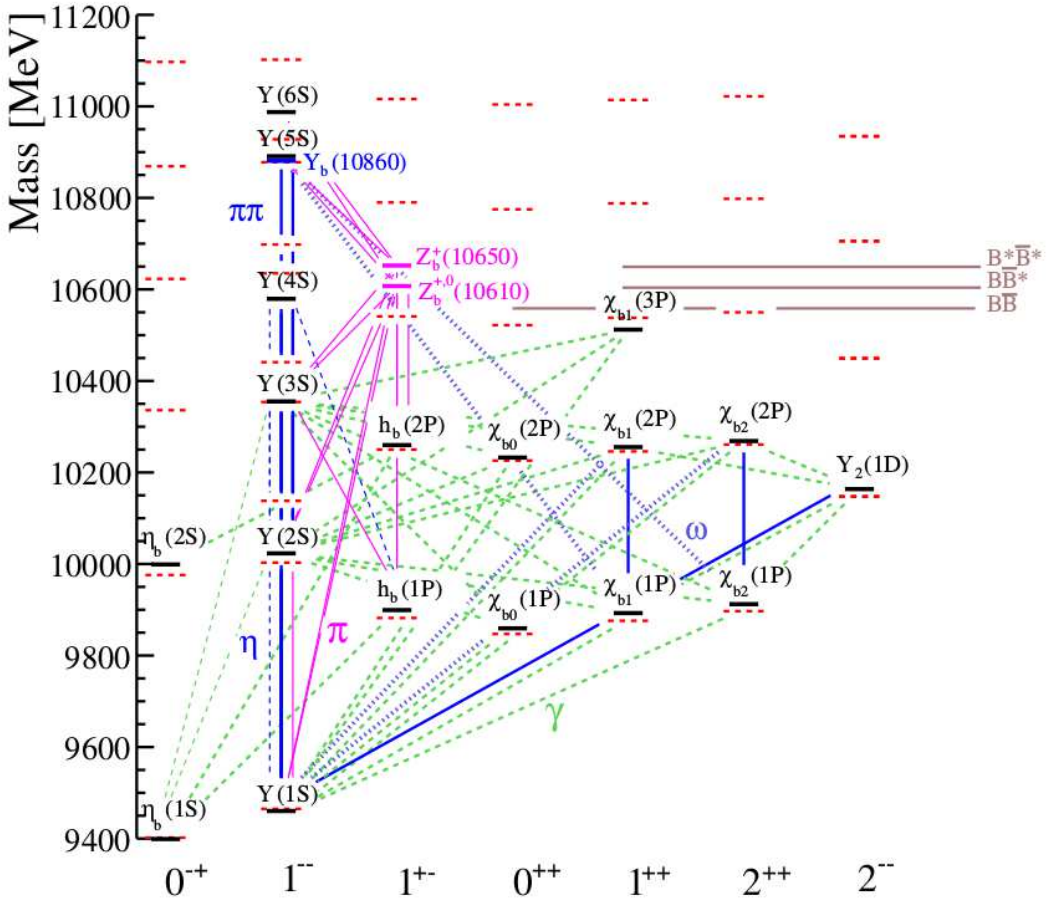

Figure 2.2: The bottomonium and bottomonium-like spectrum. The color convention follows the one of Fig. 2.1 and it is taken from Ref. [16]. Experimentally established conventional bottomonium state are shown as solid black lines. Neutral exotic candidate is shown as a blue solid line, while the charged exotics states are shown as magenta solid lines. the masses predicted from the Godfrey-Isgur model [8] are shown as dashed-red lines. Solid brown lines represents the thresholds for the open bottom production. The transitions among the states are represented as dashed-green (electromagnetic), solid-blue ($\pi\pi$, η), dashed-blue (ω), solid-magenta (π) lines.

tions, with a particular focus on the hidden-strangeness structure: the phenomenological model, a discussion of the lone experimental result before this work, and a recently proposed model to describe the dynamics.

2.1 Experimental four quarks candidates and transitions

2.1.1 The $X(3872)$ state

The $X(3872)$ is the first ever observed candidate of this new family of states. It was discovered by BELLE in 2003 in $B \to K\pi^+\pi^- J/\psi$ decay [22] as a peak in the $\pi^+\pi^- J/\psi$ invariant mass, as shown in Fig. 2.3.

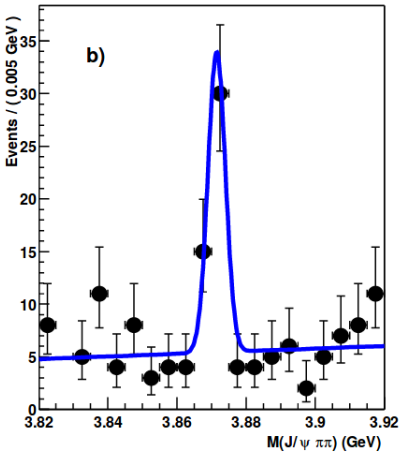

Figure 2.3: $\pi\pi J/\psi$ invariant mass peaking at the $X(3872)$ taken from Ref. [22].

Its mass from the PDG 2016 world-average is experimentally indistinguishable from the mass threshold of DD^* at the present level of precision, being $\delta m_{00} \equiv (m_{D^0} + m_{D^{*0}}) - M(X(3872)) = -0.01 \pm 0.18\,\mathrm{MeV}/c^2$ [24]. There is quite good experimental consensus on the spin-parity assignment to be 1^{++}. This measurement was carried out by LHCb ([25],[26]) with overall 16σ significance. The only possible conventional charmonium state above threshold is the 2^3P_1, commonly known as the $\chi_{c1}(2P)$. The possibility of the $X(3872)$ to be identified as the $\chi_{c1}(2P)$ is precluded by the presence of the isospin-allowed $\pi\pi J/\psi$ decay mode of the $X(3872)$, that the $\chi_{c1}(2P)$ do not have. [27].

The exotic nature of the $X(3872)$ was clear since the first observation: some narrow states may exist above open charm threshold (like the $\psi_2(1^3D_2)$, the $\eta_{c2}(1^1D_2)$, and the $\psi_3(1^3D_3)$), but none of these states had the expected quantum number similar to the measured $X(3872)$ ones. The most stringent upper limit on its width was reported by BELLE [22] to be $\Gamma(X(3872)) < 1.2\,\mathrm{MeV}$. Recently, CMS Collaboration has measured the prompt production differential cross section. The observed cross section is four times lower than the leading order NRQCD calculation [28], even if the transverse momentum p_T dependence seems to be well reproduced [29], as shown in Fig. 2.4.

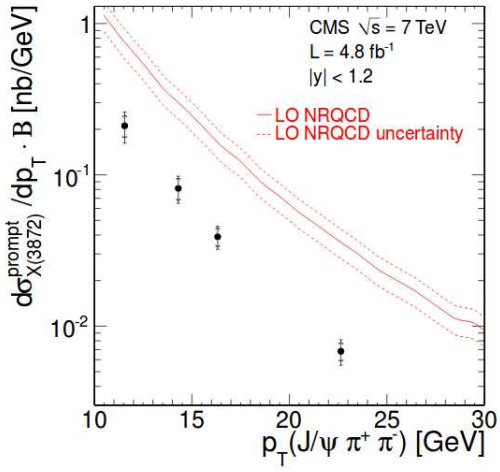

Figure 2.4: p_T dependence of the prompt differential cross section as measured by CMS in Ref. [29]. The solid and the dashed lines represent the central value and the uncertainty of the NRQCD prediction respectively.

$X(3872)$ transitions

Along with the first observation of the state, also the first two transitions between the $X(3872)$ and the J/ψ were discovered. In addition to the pure $\pi\pi$, the pions pair invariant mass shows a large ρ component, as shown in Fig. 2.5 taken from the BELLE work [22].

Another observed transition connects the $X(3872)$ and the J/ψ via ω. This was observed by BELLE [30] and BaBar [31].
The ratio $\mathcal{B}(X(3872) \to \omega J/\psi)/\mathcal{B}(X(3872) \to \pi^+\pi^- J/\psi) = 0.8 \pm 0.3$ is compatible with one. Since $X(3872)$ can decay with the same strength in $\rho J/\psi$ and in $\omega J/\psi$, that have different isospin assignment, this experimental observation is an evidence of explicit strong isospin violation for the $X(3872)$ decays. Search for charged isospin partner of the $X(3872)$ were performed, but the limits found tend to disfavour the isospin assignment $I = 1$ for the $X(3872)$, suggesting that it is indeed an iso-singlet and that the $\rho J/\psi$ decay mode causes the isospin symmetry violation.

The radiative decay into J/ψ was also measured by BELLE [32] and BaBar [33], and strong evidence of radiative decay into $\psi(2S)$ were found by BaBar [34] and by LHCb [35]. The former process has a relative branching fraction that is the 0.24 ± 0.05 of the $\pi\pi J/\psi$ one. The combined radiative decays favour an even charge conjugation parity assignment for the $X(3872)$. The radiative decays work also as diagnostic on the possible nature of the $X(3872)$. Molecular state models predict that the coupling to the $\gamma\psi(2S)$ shall be strongly suppressed with respect to the $\gamma J/\psi$ one [36]. However, the quite high ratio (2.46 ± 0.70) seems to favour the hypothesis that it is a 1^{++} charmonium, following

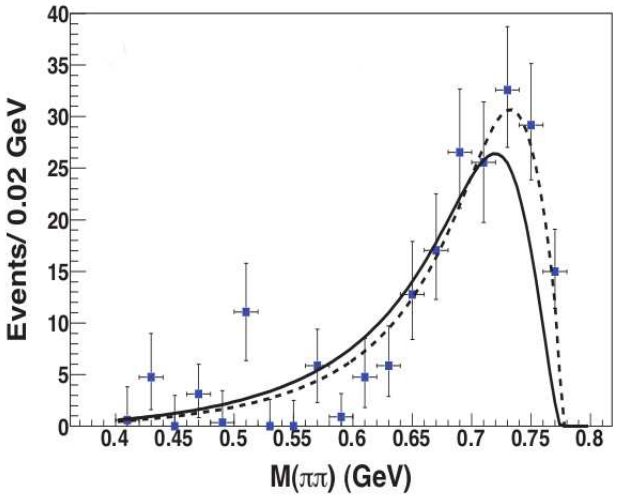

Figure 2.5: Invariant mass distribution of the $\pi\pi$ pair produced along with the J/ψ in the decay of $X(3872)$. The curves show the results of a fit for $\rho \to \pi^+\pi^-$. The dashed (solid) curve test the even (odd) $X(3872)$ parity.

what happens between the $\chi(2P)_{c1} \to \gamma\psi'$ and $\chi(2P)_{c1} \to \gamma J/\psi$ E1 transition: the latter should be suppressed by the mismatch of the initial- and final-state wave functions.

2.1.2 The $Y(4260)$ state

Right after the discovery of the $X(3872)$ different hypothesis were tested to shed light on its spin-parity. One test, that was performed by BaBar, was to search for the $\pi^+\pi^- J/\psi$ final state by means of the Initial State Radiation (ISR) events. No evidence of the $X(3872)$ were found in the process $e^+e^- \to \gamma_{ISR}\pi^+\pi^- J/\psi$. So the 1^{--} assignment for the $X(3872)$ seemed to be excluded. However, the search was not unfruitful: a new structure, peaking at $4.26\,\mathrm{GeV}/c^2$ in the $\pi^+\pi^- J/\psi$ final state, was found [37], as shown in Fig. 2.6.

The signal was subsequently confirmed by BELLE [38]. The structure is nowadays known as $Y(4260)$ and has a very interesting feature: its spin-parity assignment is 1^{--}, the same of the photon. This makes the $Y(4260)$ extremely easy to be produced at lepton colliders. Moreover, the strong coupling with the $\pi^+\pi^- J/\psi$ final state underlines the $c\bar{c}$ components. The exotic nature of the $Y(4260)$ is proven by one, albeit striking, evidence: although the mass is well above the mass threshold for the open charm $D^{(*)}\bar{D}^{(0)}$ decay, there is no evidence of such decay in the $e^+e^- \to hadrons$, as recently shown in Fig. 2.7 produced by BESII [39]. In the plot, it is possible to clearly identify the conventional charmonia. Instead, it seems that the ratio R dips in correspondence of the $Y(4260)$.

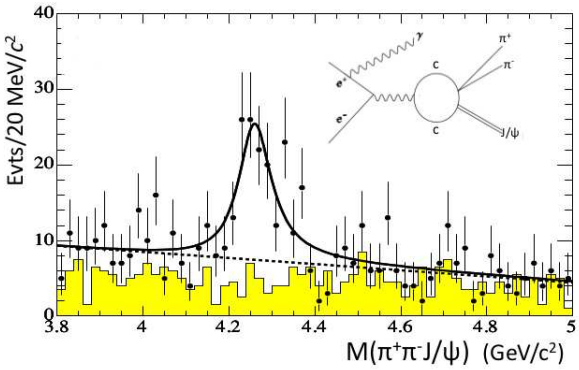

Figure 2.6: $\pi^+\pi^- J/\psi$ invariant mass in BaBar data. In the box, the ISR production is depicted.

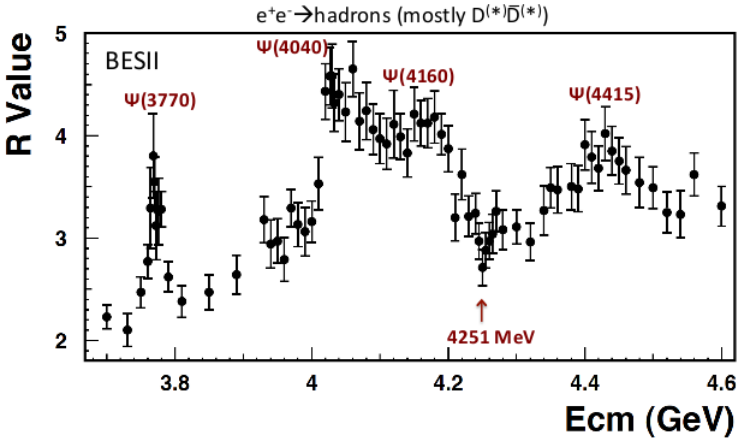

Figure 2.7: Measurement of the ratio R taken from Ref. [39]. The known conventional charmonia are shown. In the expected position of the $Y(4260)$ (marked with an brown arrow at $4251\,\mathrm{MeV}/c^2$) the ratio R has a dip.

The evidence of strong correlation with $\pi\pi J/\psi$ and the very low coupling to open charm has brought to the formulation of different models in which the $Y(4260)$ is described as multi-quark meson or $c\bar{c}-$gluon hybrid state. More details can be found in Appendix A.1.4.

One natural step is to search for similar structure in $\pi^+\pi^-\psi(2S)$. BELLE [40] and BaBar [**?**] Collaboration found no events for the $Y(4260)$ signal, but other two clear peaks were found around 4.32 and 4.66 GeV. These states are nowadays called $Y(4360)$ and $Y(4660)$: these two states represent just an example of the many states that appears in the same mass spectrum of $Y(4260)$.

Hint of $Y(4260) \to \gamma X(3872)$

Differently from the $X(3872)$, the search for $Y(4260)$ transitions seems more complicated, apart from the obvious $\pi\pi J/\psi$. In the same invariant mass region several peaks with slightly different masses were observed: experimentally it is not clear if all these peaks are either different decay modes of the same particle or different states.

Recently, the BESIII collaboration has reported the evidence of the $X(3872)$ in the $e^+e^- \to \gamma\pi^+\pi^- J/\psi$ process at four different energy values around the $Y(4260)$ peak [42]. The combined statistical significance of the $X(3872)$ for the different energy values is 6.3σ, and the signal is quite clear, as shown in Fig. 2.8a. More interestingly, studying the $X(3872)$ production rate there is some indication that the production may be associated with the $Y(4260)$, as shown in Fig. 2.8b. The presence of this transition shows a common nature between these two states.

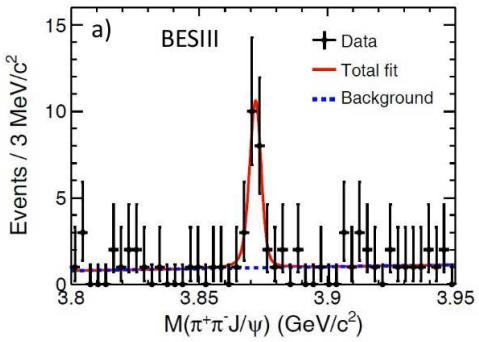

(a) $\pi^+\pi^- J/\psi$ combined invariant mass. The black dots represent the data, the solid-red line shows the total fit, while the background is represented by a dashed blue line.

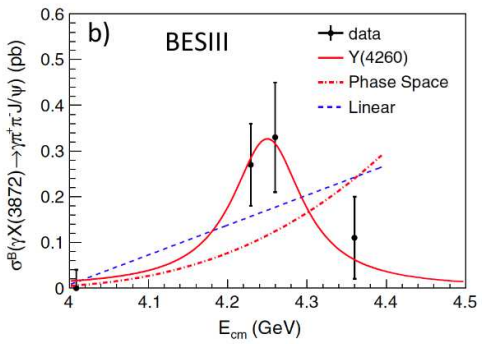

(b) Production cross section of $X(3872)$ around $Y(4260)$ center of mass. The cross section is fitted with three different production dependence hypotheses.

Figure 2.8: BESIII recent work on the measurement of the $e^+e^- \to \gamma\pi^+\pi^- J/\psi$ cross section at different center of mass energies.

BESIII lineshape scan

In order to deepen the knowledge on the $Y(4260)$ it can be helpful to study the production cross section and the lineshape. The spin-parity of the $Y(4260)$ allows the direct production at e^+e^- colliders: differently from other exotics it is indeed much easier for these machines to accumulate large statistics and study the production cross section at different center-of-mass energies. If the B-factories profit of the ISR to collect the $Y(4260)$, BESIII can directly move the center of mass energy of the collision around the peak, and perform precision scans. This justify why sometimes BESIII is called a $Y(4260)$-factory.

BESIII has recently reported the measurement of the cross section of the process $e^+e^- \to \pi^+\pi^- J/\psi$ using two different set of energy scan data [43]. The two datasets differ for the number of collected center of mass energies and the luminosity per each energy value. A first set of data, called XYZ-data, has 9 different energies with high luminosity ($40\,\mathrm{pb}^{-1}$ per energy value). The second set of data, called *Scan*-data, is a fine scan of the $Y(4260)$ region with lower luminosity (7-9 pb^{-1} per energy value) used for R ratio measurements. The results of simultaneous fits at the two datasets are shown in Fig. 2.9a and Fig. 2.9b for the XYZ and *Scan* data respectively.

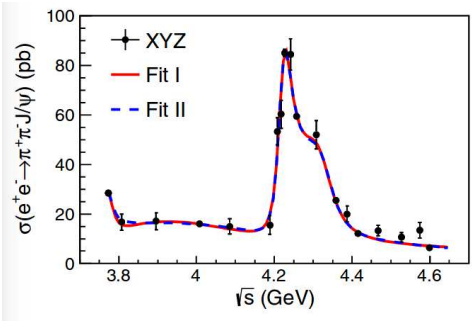

(a) $e^+e^- \to \pi^+\pi^- J/\psi$ cross section with the high statistics sample. The red line represents the best fit.

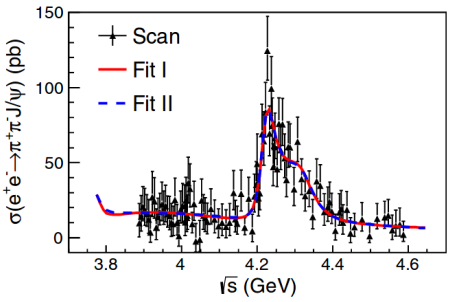

(b) $e^+e^- \to \pi^+\pi^- J/\psi$ cross section with the low statistics sample. The red line represents the best fit.

Figure 2.9: Study of the $Y(4260)$ lineshape by BESIII collaboration.

The results are a breakthrough: the signal around 4.26 GeV is a combination of two different resonances. The lighter one is narrow and the width and mass agree with the BaBar parameters of the $Y(4260)$ [44], and the heavier one is wider and has a mass compatible with the exotic $Y(4360)$, a resonance observed by BELLE [40] and BaBar [41] in $e^+e^- \to \pi^+\pi^-\psi'$. Moreover, BESIII data do not confirm the signal of a lighter Y state, the $Y(4008)$ observed by BELLE [38]. In the next few years, BESIII plans to perform a fine scan of the center of mass energy region between 4.2 and 4.6 GeV in 10 MeV steps. These sets of data will allow BESIII to play a major role in understanding the features of $Y(4260)$ and its connection with the other exotics.

2.1.3 The $Z_c(3900)^+$ state

The $\pi^+\pi^- J/\psi$ final state seems to be a good test bench for the searches of charmonium-like exotics and their transitions. The re-analysis of the full phase space revealed another interesting feature.

Indeed, the BESIII collaboration reported the existence of a new structure in the in the $J/\psi\pi^\pm$ mass spectrum, from the $\pi^+\pi^- J/\psi$ system at center of mass energy of 4.26 GeV. Fig. 2.10. shows the plot taken from Ref. [45].

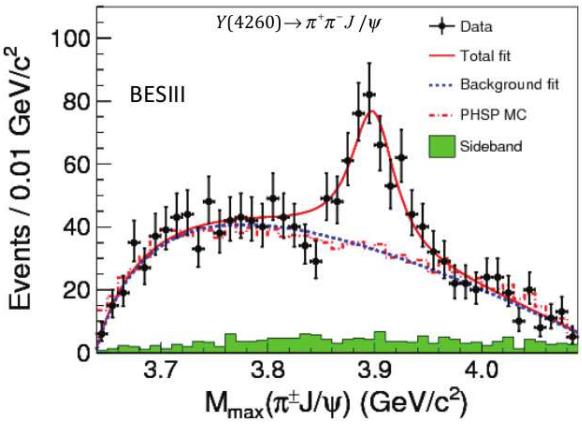

Figure 2.10: Invariant mass distribution of the $\pi^{\pm}J/\psi$ pair collected by BESIII and reported in Ref. [45]. The green histogram represents the background level due to the J/ψ sideband events, while the red dashed histogram shows the expected phase space distribution.

The $Z_c(3900)^+$, being charged, cannot be accommodated in any conventional charmonium picture. Moreover, it is the only exotic candidate in which a complete isospin triplet has been observed [46]. The mass $M(Z_c(3900)^+) = 3899.0 \pm 6.1\,\mathrm{MeV}/c^2$ is $24\,\mathrm{MeV}/c^2$ above the $D^{*+}\bar{D}^0$ threshold, so it can decay into open charm. Such final state was observed by BESIII in $e^+e^- \to \pi^+ D^- D^{*0}$ [47],[48], as shown in Fig. 2.11. Since the mass of this new particle is $\sim 2\sigma$ away from the mass of the $Z_c(3900)$, the new state was called $Z_c(3885)$.

The quite large signal observed allowed BESIII also to determine the spin-parity assignment of the $Z_c(3885)$, as shown in Fig. 2.12. The 1^+ hypothesis is preferred and the 0^- and 1^- assignments are quite confidently ruled out.

Recently BESIII published a new measurement of the $Z_c(3900)$ that allowed to extract the spin-parity by means of a partial wave analysis [49]. The favoured assignment is 1^+ as shown in Fig. 2.13.

This new measurement of BESIII strongly supports the hypothesis that the $Z_c(3885)$ and the $Z_c(3900)$ are the same state. If this is the case, the $Z_c \to D^* D$ partial wave is 6 times larger than the one in $\pi J/\psi$. This feature is typical also of the $X(3872)$. However, the ratio is quite small compared to the one calculated for above-threshold charmonia. On the nature of this charged state several models are on the market, but none can fit all the properties. Some more details about the theoretical models can be found in Appendix A.

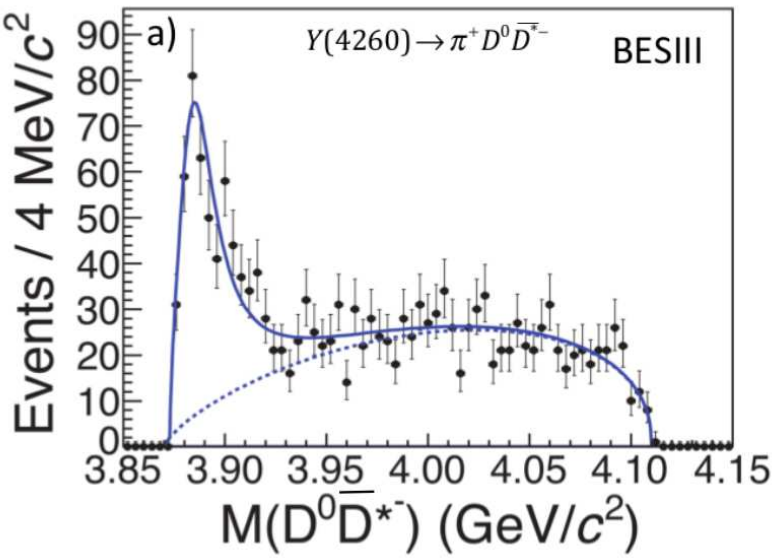

Figure 2.11: The $D^0\bar{D}^*-$ invariant mass as observed by BESIII in Ref. [48]

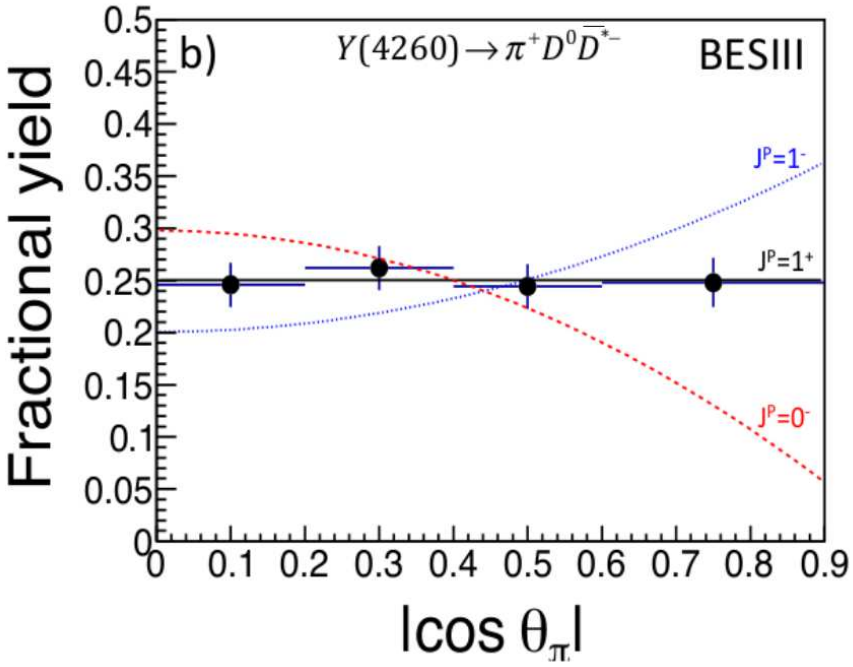

Figure 2.12: Efficiency corrected angular distribution for the $Z_c(3885)$ compared to the different spin-parity assignment taken from Ref. [48].

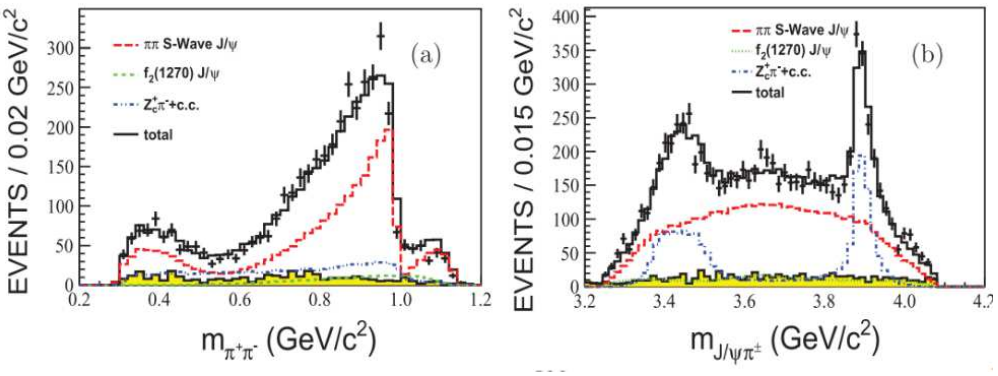

Figure 2.13: PWA of the $\pi^+\pi^- J/\psi$ invariant mass at 4.26 GeV as taken from Ref. [49]. a) $\pi^+\pi^-$ invariant mass distribution. b) $J/\psi\pi^\pm$ invariant mass distribution. The black dots represents the data, while the black histogram the total fit components. The $Z_c(3900)$ components is shown as a blue-dashed histograms. The PWA shows that the signal is dominated by the S-wave $(\pi^+\pi^-)$ J/ψ components (red histogram) plus the $Z_c(3900)$ one.

2.1.4 Exotics in the bottomonium spectrum

The limited available energy at the B-factories and the difficulties to study such exotic states at experiments at higher energy collider do not allow to have similar knowledge of the above-threshold part of the bottomonium spectrum as of the charmonium one. The only exotics are the $Z_b(10610)^+$, the $Z_b(10650)^+$ and the $\Upsilon_b(10860)$. The latter state was discoverer by BELLE [50] in the search of a counter-part of the $Y(4260)$ in the $\pi^+\pi^-\Upsilon(n_rS)$ $(n_r = 1, 2, 3)$. The results for these searches are shown in Fig. 2.14, in which the R ratio for the production cross section in the vicinity of the expected mass of the $\Upsilon(5S)$ is presented. Whether this new state is an equivalent in the b quark sector of the $Y(4260)$ or an overlap of the standard $\Upsilon(5S)$ and a equivalent of the $Y(4260)$ is still to be understood; even if it shows some of the expected properties of the standard bottomonia (*e.g-* an increase in the $e^+e^- \to b\bar{b}$ cross section), its partial widths to lower bottomonia are two orders of magnitude larger than the theoretical prediction, and they are also larger than the measured value of the $\Upsilon(4S)$ width.

Enhanced transition to the lower bottomonia

In order to understand the nature of the $\Upsilon(10860)$, the BELLE collaboration accumulated a large statistics at 10.866 GeV. The distribution of the masses that recoils against a $\pi^+\pi^-$ pair are plotted in Fig. 2.15. Other than the lower 1^{--} $\Upsilon(n_rS)$ $(n_r = 1, 2, 3)$, two additional peaks were observed: the $h_b(1P)$ and the $h_b(2P)$ were finally detected for the first time [51]. The observation of the P-wave spin-singlet states in this particular decay mode is another proof of the exotic nature of the $\Upsilon(10860)$, since the processes

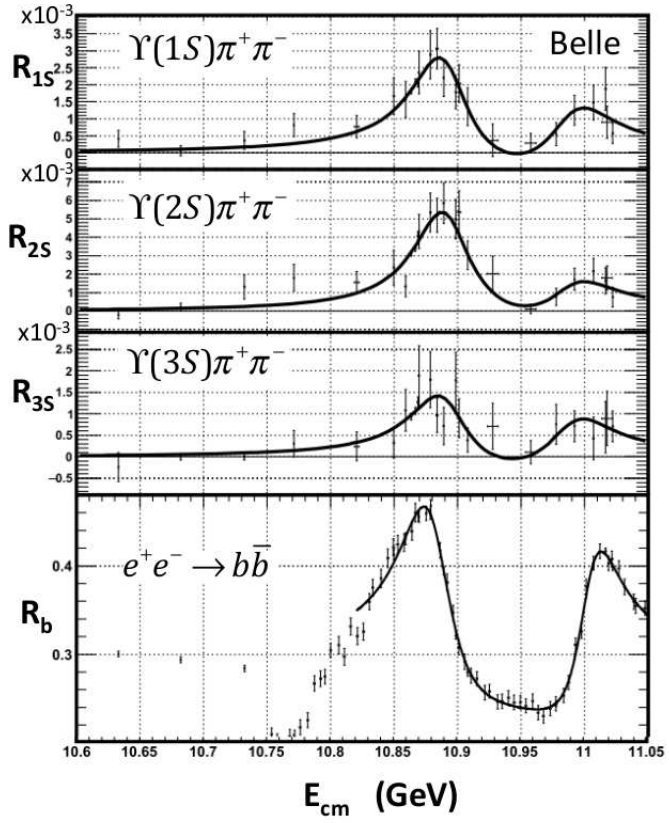

Figure 2.14: Ratio R measurements for the $e^+e^- \to \pi^+\pi^-\Upsilon(n_rS)$ ($n_r = 1, 2, 3$) (upper parts) and $e^+e^- \to b\bar{b}$ (lower part) in the vicinity of the $\Upsilon(5S)$ resonance from Ref. [50]

$\pi^+\pi^-\Upsilon(n_rS)$ and $\pi^+\pi^-h_b(m_rP)$ ($m_r = 1, 2$) have similar production rates, even though the latter process should be suppressed by the heavy-quark spin flip mechanism.

Studying the Dalitz plot BELLE discovered that the production of the $h_b(m_rP)$ was mediated by the production of two new particles: the Z_bs, that appear in the $\pi^\pm h_b$ systems. These new two particles have masses $2\,\mathrm{MeV}/c^2$ above the open bottom decay threshold: the lighter one, the $Z_b(10610)$ is just above the BB^* threshold, while the heavier, the $Z_b(10650)$ is just above the B^*B^* threshold. This connection between the $\Upsilon(5S)$ and the lower bottomonia is now used to study in more detail the least accessible states below threshold.

The spin-parity assignment for the Z_bs is 1^+, same as the Z_c, suggesting that they may have a common nature. However, as for the other states presented in these sections, there is no clear understanding of their structure. The branching ratios of $Z_b(10610)$ to BB^* and to B^*B^*, and the absence of BB^* decay mode for the $Z_b(10650)$ suggest that the molecular state hypothesis is strongly supported by the experimental observations

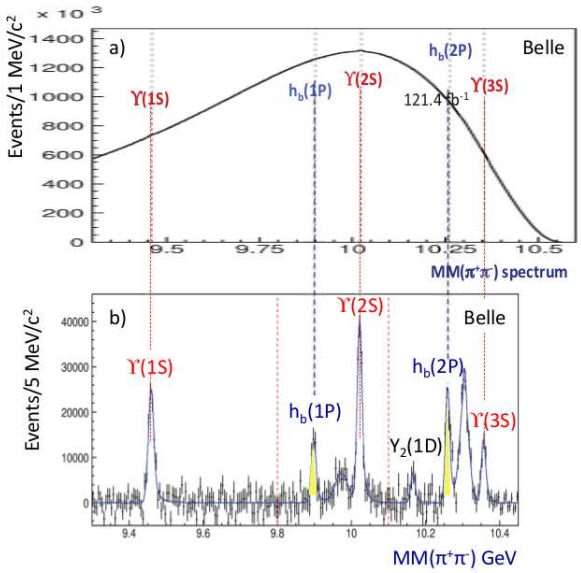

Figure 2.15: Distribution of the masses recoiling against $\pi\pi$ pairs taken from Ref. [51]. a) The full spectrum. b) the spectrum after background subtraction. The lines connect the peaks in the two plots.

[52].

2.2 Pentaquark searches

The story of the observation of pentaquark candidates goes back to the 70s. Two channels were particularly used for this searches, K^+p and K^+d (where d stands for the deuteron). Precise scrutiny of the cross section were performed to search for evidence of state with positive strangeness ($\mathcal{S} = +1$) quantum number. The search was focused to particles that may contain an $\bar{s}$ quark in a $qud\bar{s}u$ five-quarks structure. The first claims were two candidates with isospin $I = 0$, named $Z_0(1780)$ and $Z_0(1865)$, and three with $I = 1$, the $Z_1(1900)$, the $Z_1(2150)$ and the $Z_1(2500)$ and were reported in the 1976 version of the PDG [53]. However, all of them were not confirmed by the 1994 PDG review [54].

Probably, the most famous pentaquark claim was the $\theta(1540)^+$, observed by 4 different experiments with statistical significance around 5σ. However, each of these candidates turned out to be inconsistent after an analysis with larger statistics. The enthusiasm followed by such huge disappointment can be easily summarized by the final sentences of the 2006 PDG report on exotic pentaquark [55]:

> all the attempts to confirm the two other claimed pentaquark states have

led to negative results. The conclusion, that pentaquarks in general, and the θ^+, in particular, do not exist, appears compelling.

Even if the pentaquarks were too elusive for the early experimental techniques, the present generation of detectors and accelerators has brought a new hope to these searches. In the summer of 2015 the LHCb collaboration announced the observation with very large statistical significance of two structure compatible with the five-quark picture [1]. The following sections begin with a brief review of the LHCb pentaquarks. After that, an extended section on the hidden-strangeness pentaquarks is presented. Theoretical models and the lone experimental result will be discussed.

2.2.1 Pentaquark candidates at LHC

The existence of states with 5 quarks seemed to be quite over after the disappointing results of the $\theta^+(1540)$. And the search for exotic candidates was more focused on the XYZ states.

In 2015, the LHCb collaboration reported the observation of two structure compatible with a minimal configuration of 5 quarks in the process $\Lambda_b^0 \to pJ/\psi K^-$ [1]. The new signal appeared as a band in the Dalitz plot of $M^2(pJ/\psi)$ versus $M^2(K^-p)$ in the pJ/ψ invariant mass, as shown in Fig. 2.16a and in Fig. 2.16b.

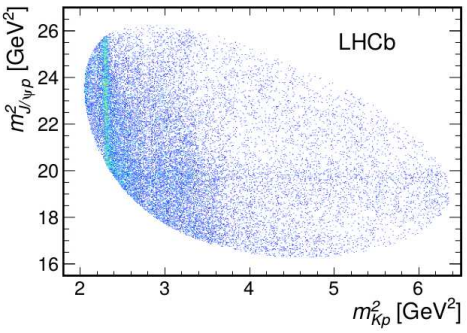

(a) $\Lambda_b^0 \to pJ/\psi K^-$ Dalitz plot as observed by LHCb. A straight continuous horizontal band is visible in $M^2(pJ/\psi)$, as well as the Λ^* signal as a vertical band.

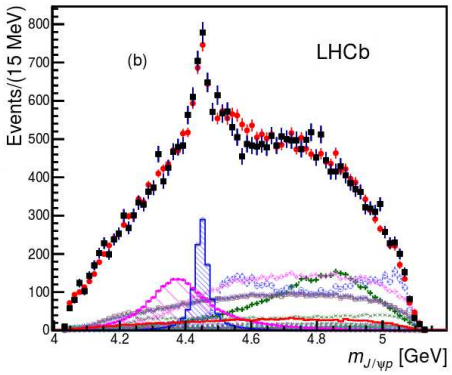

(b) pJ/ψ invariant mass. The black dots represent the data, while the red ones represents the best fit from the PWA. The shaded histograms represents the two pentaquark candidates: the $P_c(4450)$ and the $P_c(4380)$.

Figure 2.16: Study of the process $\Lambda_b^0 \to pJ/\psi K^-$.

In order to understand the nature of this signal, LHCb performed a partial wave analysis based on the helicity formalism. The decay was parametrized as a function of the masses and the angles of the decaying particles. All the lower and well-know Λ^* amplitudes

were included taken from the 2014 PDG tables [56]: this parametrization was not able to reproduce the data. Only by adding two new components in the pJ/ψ amplitude it was possible for LHCb to fit the data, as shown in Fig. 2.16b.

The higher mass state appears properly described as a clear peak in the invariant mass. It is now called $P_c^+(4450)$ and has a fitted mass $M(P_c(4450)^+) = (4449.8 \pm 1.7 \pm 2.5)\,\mathrm{MeV}/c^2$ and a width $\Gamma(P_c(4450)^+) = (39 \pm 5 \pm 19)\,\mathrm{MeV}$, a significance of 12σ and a fit fraction of 4.1%. Even if one single resonance seems enough, the presence of a second state improves the global fit significance. The lower mass state, dubbed $P_c(4380^+)$, has a fitted mass of $M(4380) = (4380 \pm 8 \pm 29)\,\mathrm{MeV}/c^2$ and width of $\Gamma(P_c(4380)^+) = (205 \pm 18 \pm 86)\,\mathrm{MeV}$, a significance of 9σ and a fit fraction of 8.4%. In the same work the spin-parity is discussed. The assignment is not clear, but the most favoured hypotheses are $(3/2^-, 5/2^+)$ and $(5/2^+, 3/2^-)$ for the (lighter, heavier) candidate combinations.

One (but not the only) method to understand if a peak in the invariant mass is produced by a real resonance is to study the Argand plot. In this plot, the single amplitude is substituted by a combination of independent complex amplitudes at six equidistant points in the Γ range to be fit simultaneously with the other parameters. The results for the $P_c(4450)^+$ and $P_c(4380)^+$ are shown in Fig. 2.17.

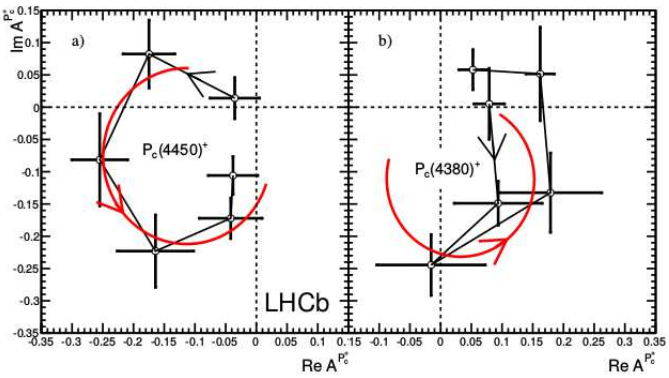

Figure 2.17: Results of the fit for the real and imaginary parts of the complex amplitude used to describe the $P_c(4450)^+$ (left) and $P_c(4380)^+$ (right) plotted in counter-clockwise order. The red lines shows the expected behaviour for a Breit-Wigner resonance.

The counter-clockwise movement of the $P_c(4450)^+$ amplitude is well described by the LHCb data, while for the $P_c(4380)^+$ the result is less clear. This is caused by larger uncertainties on the first two points. Only with larger data sample will be possible to point out if the $P_c(4380)^+$ is a real resonance and not a kinematic effect.

Since the discovery, the LHCb collaboration has performed several independent tests to confirm the existence of the pentaquark candidates. A first test was performed by constructing the Dalitz plane using the measured $M(Kp)$ distribution and the Legendre polynomial moments of the Λ^* helicity angles [57]. The hypothesis that the observed mass distribution can be reproduced by means of only the Λ^* final states was ruled out

with 9σ significance. Another test was performed searching exotic contribution in the singly Cabibbo-suppress decay $\Lambda_b^0 \to J/\psi p\pi$: the very limited statistics yielded to a 3.1σ evidence of a summed presence of non-standard hadronic contribution [58].

Even if there are several models available to explain the production and the nature of these pentaquarks, it is important to wait for more data to have a more solid evidence of the features of these states, with the J^{PC} assignment as first important missing element. More data and more decay modes will surely provide more conclusive information on the existence of these states. On the other hand, the mere observation of the two strong pentaquark candidates have restarted the search for new states. One of the most natural path to follow is to search for hidden-strangeness siblings of the hidden-charm pentaquark by simply adjusting the decay in order to substitute the J/ψ with a ϕ and use the charmed baryons as source. The resulting final state shown by Lebed [2] is $\Lambda_c^+ \to p\phi\pi^0$, which is a Cabibbo-suppressed decay. The resulting Feynman diagram are shown in Fig. 2.18.

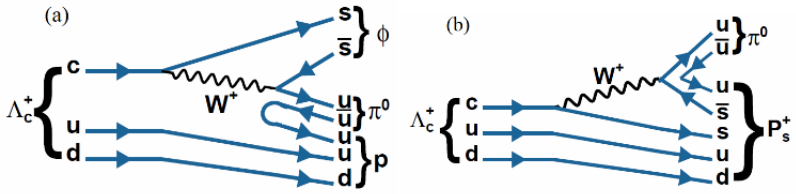

Figure 2.18: Feynman diagrams for the a) non-resonant singly Cabibbo suppressed $\Lambda_c^+ \to p\phi\pi^0$ final state b) resonant pentaquark P_s^+ production, taken from Ref. [59].

2.3 The hidden-strangeness pentaquarks

The enthusiasm that the discovery of such a plethora of different states has created, especially following the observation of the pentaquarks, has brought the theoretical community to produce models to predict new states. In the following, we will briefly present works that discuss the possibility to search for hidden-strangeness siblings of the P_c^+ pentaquark and their final state dynamics. Finally, the lone experimental search, done by the BELLE collaboration will be discussed with the aim to enlighten the differences with the BESIII experimental search that will be later discussed.

2.3.1 Lebed production model

The first work totally dedicated to the hidden-strangeness siblings of the LHCb pentaquark was proposed by R.F. Lebed [2]. The idea beyond this model is clear and

simple: substitute the $b \to c$ transition with the $c \to sW^{*+} \to s\bar{s}u$ process and follow the scheme that brought to the discovery of the P_c^+ pentaquarks: this brings to the $\Lambda_c^+ \to p\phi\pi^0$ process and the hidden-strangeness pentaquark, dubbed P_s^+ is created in the $p\phi$ invariant mass to have a quark content of $P_s^+ = s\bar{s}uud$. The expected decay scheme follows the diquark picture (more information will be discussed in Appendix A.1.3) and it is represented in Fig. 2.19.

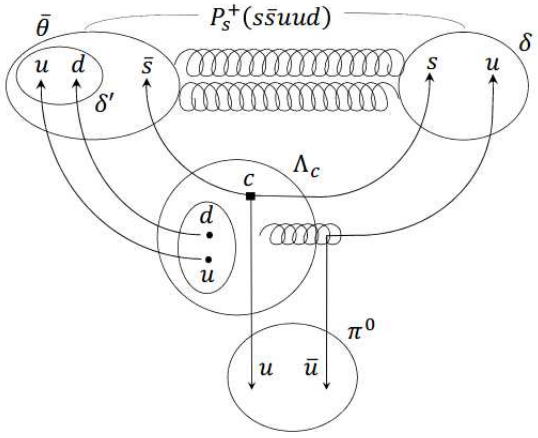

Figure 2.19: Schematically representation of the decay $\Lambda_c^+ \to p\phi\pi^0$.

The entire work provides a clear explanation why the P_s pentaquark should exist, after the discovery of the P_c^+. First, the charmed decays are less CKM suppressed that the bottom counterparts, being the $|V_{cb}V_{cs}^*|^2/|V_{cs}^*V_{us}| \simeq \frac{1}{30}$. Therefore, the branching fractions should be enhanced. Moreover, it is possible to calculate the ratio of the resonant and non-resonant content of the P_c^+:

$$\frac{\mathcal{B}(\Lambda_b \to P_c^+ K^-)}{\mathcal{B}(\Lambda_b \to pJ/\psi K^-)} = \begin{cases} (8.4 \pm 0.7 \pm 4.2)\% \\ (4.1 \pm 0.5 \pm 1.1)\% \end{cases} \tag{2.1}$$

for the $P_c(4380)^+$ and $P_c(4450)^+$ respectively: the value of the resonant component, given the large available phase space, is considerable; thus, the P_s^+ production should not be uncommon considered the tiny phase space available. In fact, unlikely the Λ_b decay, the available phase space is quite reduced

$$m_{\Lambda_c} - m_\phi - m_p - m_{\pi^0} = (193.75 \pm 0.14)\,\mathrm{MeV}/c^2$$

compared to more than 1 GeV for the Λ_b decays. The effect is largely magnified also from the fact that, if the production mechanism is flavor independent, the produced peak will be outside the accessible phase space for Λ_c decays. In fact, the P_c^+ lies roughly 400 MeV above the $J/\psi p$ threshold: if the number is in the same order of magnitude the Λ_c

would not be heavy enough to permit the decay. However, there are two considerations that may arise at this point: first, the low tail of very-broad $P_c(4380)^+$ counterpart could, in principle, be observable in the higher region of the Λ_c phase space (if the mechanism holds exactly). Second, the states observed by the LHCb collaboration are excited spin states: there is no particular reason why the P_s^+ should appear with the same spin quantum numbers or lie at the same distance from threshold of the hidden-charm counterpart. In these last two sentences lies largely the motivation of the BELLE search and of the work presented in this thesis.

2.3.2 BELLE searches

Motivated by the first observations at LHCb, and following the Lebed [2] prescriptions, BELLE started an analysis to search for hidden-strangeness siblings of the LHCb pentaquarks. Since the analysis is very similar to the one that it will be shown later, it is discussed in more details.

BELLE profit of the $915\,\mathrm{fb}^{-1}$ collected at, or near, the $\Upsilon(4S)$ and $\Upsilon(5S)$, recorded by BELLE detector at the KEKB asymmetric energy e^+e^- collider. BELLE's analysis strategy makes use of the identification of the two photons from the π^0 decays, and then identify the kaons and the protons by means of the PID likelihood ratio method. ϕ candidates are formed by taking two opposite charged tracks identified as kaons. Events are accepted if the charged kaons pairs fall in the wide range $(0.99, 1.13)\,\mathrm{GeV/c^2}$. To reduce the combinatorial background from B decays, BELLE required the scaled momentum, defined as $\mathrm{x_b} = Pc/\sqrt{E_{CM}^2/4 - M^2c^4}$, to be greater than 0.45, where E_{CM} is the energy of the center of mass, P and M are the momentum and the invariant mass of the candidate. To further reduce the background, a vertex fit is applied. The process $\Lambda_c^+ \to \Sigma^+\phi$ has the same final state of the decay of interest, and it can be removed by requiring that the invariant mass of the $p\pi^0$ pairs are outside a $10\,\mathrm{MeV}/c^2$ interval around the PDG value of Σ^+ mass [24]. The Λ_c^+ signal region is then identified has an interval of 2.5σ around the nominal mass. In order to extract the signal yield, a 2D fit performed. Fig. 2.20a and Fig. 2.20b show the fit projections along the $K^+K^-p\pi^0$ and K^+K^- invariant masses respectively.

To search for the pentaquark, only the events whose K^+K^- is in a $20\,\mathrm{MeV/c^2}$ interval around the ϕ nominal mass are preserved. Finally, after all these cuts BELLE obtains 77.6 ± 28.1 pentaquark candidates events, that are represented as a function of the invariant mass background-subtracted of the $p\phi$ pairs as shown in Fig. 2.21.

The fit results points toward an indication of a possible structure with mass $M = (2.025 \pm 0.005)\,\mathrm{GeV}/c^2$ and width $\Gamma = (0.022 \pm 0.012)\,\mathrm{GeV}$. However, the statistical significance is below 3 sigma, so BELLE report only the upper limit $\mathcal{B}(\Lambda_c^+ \to P_s^+\pi^0) \times \mathcal{B}(P_s^+ \to \phi p) < 8.3 \times 10^{-5}$ at 90% C.L..

In order to start the process to identify a new possible spectroscopy of exotic states, the

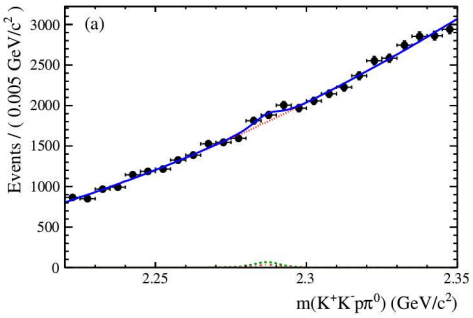

(a) Invariant mass of the $K^+K^-p\pi^0$. A very small bump is observed around the expected Λ_c mass region. The black dots are data and the red-dashed line represents the background.

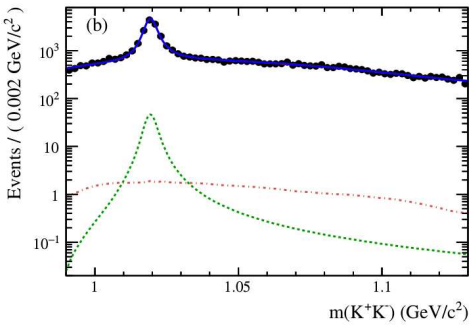

(b) K^+K^- invariant mass. The black dots represent the data. A clear ϕ signal is observed over the background, represented as red-dotted line.

Figure 2.20: Two dimensional fit at KK and $KKp\pi^0$ invariant masses to extract the signal yield.

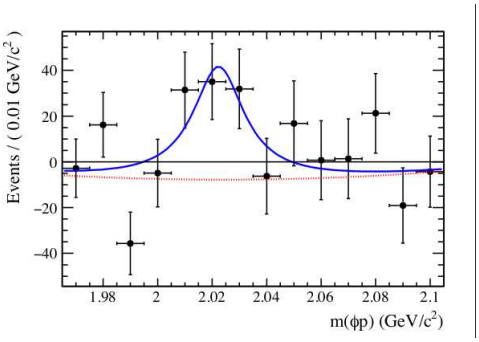

Figure 2.21: ϕp invariant mass from BELLE data. The black dots represents the data, the blue line shows the total fit, while the red line represents the phase space components. No clear structure is observed. The fit is minimized by adding a structure around $2.025\,\mathrm{GeV}/c^2$.

result shall be compared with the one of LHCb: this upper limit is six times larger than the product of the branching ratios observed for the analogous hidden-charm pentaquark state.

The BELLE and BESIII analysis started almost at the same time. The BESIII environment provides the best characteristic to perform such task. As it will shown later during this work, one of the most interesting feature is that BESIII Λ_c events are produced at threshold, in a much cleaner environment compared to the one of BELLE. This feature allows BESIII to be competitive, in terms of precision, against the B-factories, even with a smaller integrated luminosity.

2.3.3 Triangular singularity in $p\phi$ mass

As explained for the other kinematics effects in Sec. A.1.5 and A.2.1, triangular singularities arises when an interaction among the events in some final states occurs. In the specific case of the $p\phi$ pentaquark, J.J Xie and F.K Guo [3] propose that a triangular singularity can modify the final state dynamics of the Λ_c decay into $p\phi\pi^0$. The authors point out that an enhancement can be caused by the opening of the threshold of the $K^*\Sigma^*(1385)$, with the subsequently decay of the $\Sigma^*(1385)$ into $\pi^0\Sigma$ (or Λ) and then $K*\Sigma$ (or Λ) rescatters into the ϕp final states, as shown in Fig. 2.22.

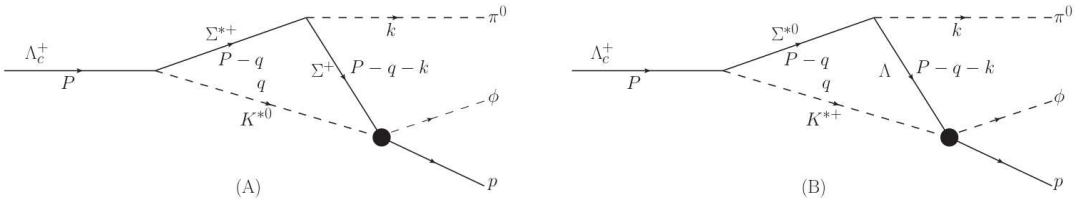

Figure 2.22: Triangular singularities as proposed by Xie and Guo [3].The triangle produces the final state via (A) Σ^+-exchange, (B) Λ-exchange. The kinematical variables (P, q, k) are also shown.

If a P_s exist, it must couple to both $p\phi$ and to $K^*\Sigma/\Lambda$. This effect, combined with the reduced phase space available, can make a clear identification of such state more complicated.

In their work, the authors test three different models: Model I is constructed considering both the contribution from a model P_s^+ and the FSI (final state interactions) effects as taken from Ref. [60]; Model II represents the case with only the triangular singularity; Model III shows the pure phase space contribution. The numerical results are shown in Fig. 2.23. The results are normalized to the BELLE data [59] to compare to only available experimental results.

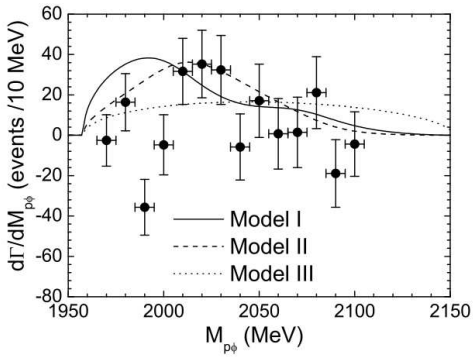

Figure 2.23: Numerical results for the models proposed in Ref. [3]. The black dots represent the BELLE data taken from Ref. [59].

Model II seems to almost fit the BELLE data. The data seems to favour the hypothesis that the peak is generated indeed by the $K^*\Lambda$ exchange (part B of Fig. 2.22). This points towards the possibility that, if it exists, the P_s^+ can be difficult to find, due to triangular singularities shown by the authors. The authors produce also a prediction of the order of magnitude of the expected branching ratio for Model II, $\mathcal{B}(\Lambda_c^+ \to \pi^0 \phi p)_{II} = \mathcal{O}(10^{-4})$, that it is of the same order of magnitude of the BELLE result.

Part II

Pentaquark search with BESIII data

Chapter 3

BEPCII and BESIII detector

3.1 BEPCII

The Beijing Electron Positron Collider II [61] (BEPCII) is a major upgrade of the existing BEPC, hosted at the Institute of High Energy Physics (IHEP) of the Chinese Academy of Science in Beijing, PRC. It has been operating successfully since March 2009 [62], when the first physics collisions were performed. It consists of a double ring, with two crossing points. In one of the interaction points the BESIII experiment records the fragments of the collisions, while in the other point the Beam Energy Monitor System (BEMS) checks the energy and the status of the beams via Compton backscattering [63]. The electron and positron beam energy spans from 1 to 2.3 GeV and thus the center of mass energy accessible ranges between 2 and 4.6 GeV: this allows BESIII to successfully pursue its very broad physics program, with a unique window on the charmonium and on the exotic states.

The accelerating structure is composed of a LINAC plus two accumulation rings. A bird's-eye view of the structure is shown in Fig. 3.1. To achieve larger luminosity with respect to its predecessor, BEPCII exploits multi-bunches (93 per ring) operations, with higher beam current and squeezed bunches, using micro-β quadrupoles [62]. The electron and positron cross the interaction pion with a angle of $\pm 11\,\mathrm{mrad}$. The z direction is identified along the beam direction.

The design luminosity of $10^{33}\,\mathrm{cm}^{-2}\mathrm{s}^{-1}$ is optimized at a beam energy of 1.89 GeV [62]. During the 2016 data taking, in a dedicated run for the machine development, the design luminosity was finally achieved, setting a new world record for collider in this energy regime [64].

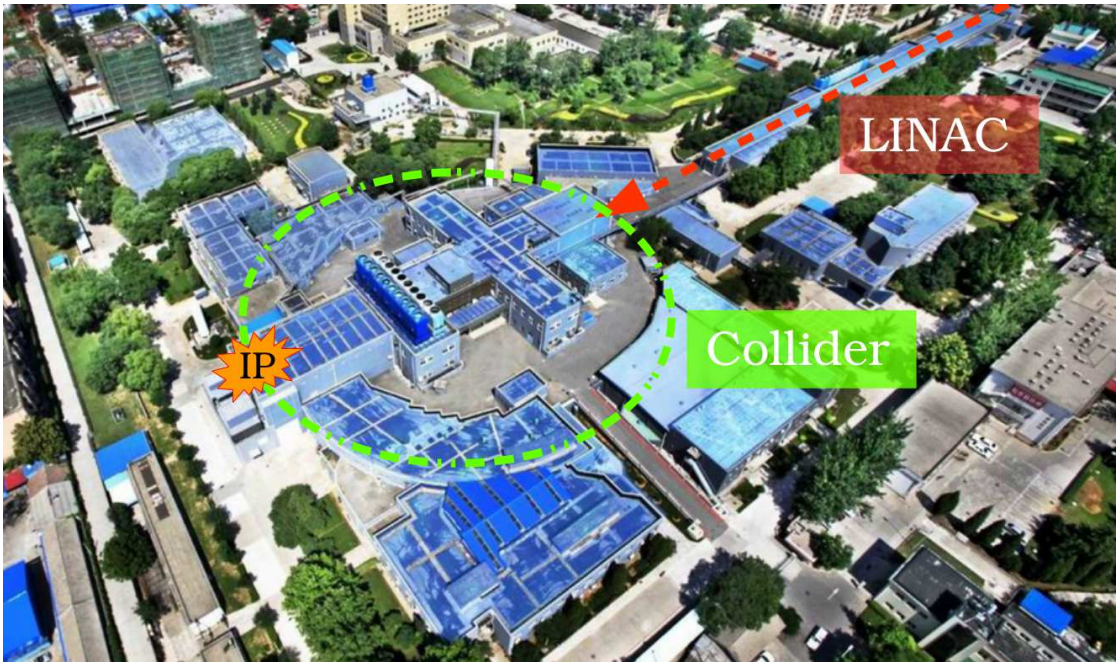

Figure 3.1: Bird's-eye view of the BEPCII accelerating structure. The red line indicates the LINAC, while the green circle shows the position of the accumulation ring where electrons and positrons run before colliding in the interaction point, where the BESIII detector is hosted.

3.2 BESIII detector

The BESIII spectrometer presents a classical scheme for central detectors designed for flavor physics. From the interaction point to the outside it is composed of: beryllium beam pipe, that is used to contain the circulating beams; Multilayer Drift Chamber (MDC), used as the tracking element for the charged particles; scintillators that are used as Time-Of-Flight (TOF) detectors; a CsI(Tl) electromagnetic calorimeter (EMC), to measure the energy of neutral and charged particles; the superconductive solenoid, that provides the 1 T axial magnetic field; Resistive Plate Chambers (RPCs) are placed in the return yoke of the magnet to operate as Muon Counters (MUC). A schematic view of the detector is shown in Fig. 3.2. The detector covers 93% of the 4π and it is divided in two parts: the barrel ($|\cos\theta| < 0.82$) and the endcaps ($0.86 < |\cos\theta| < 0.93$).

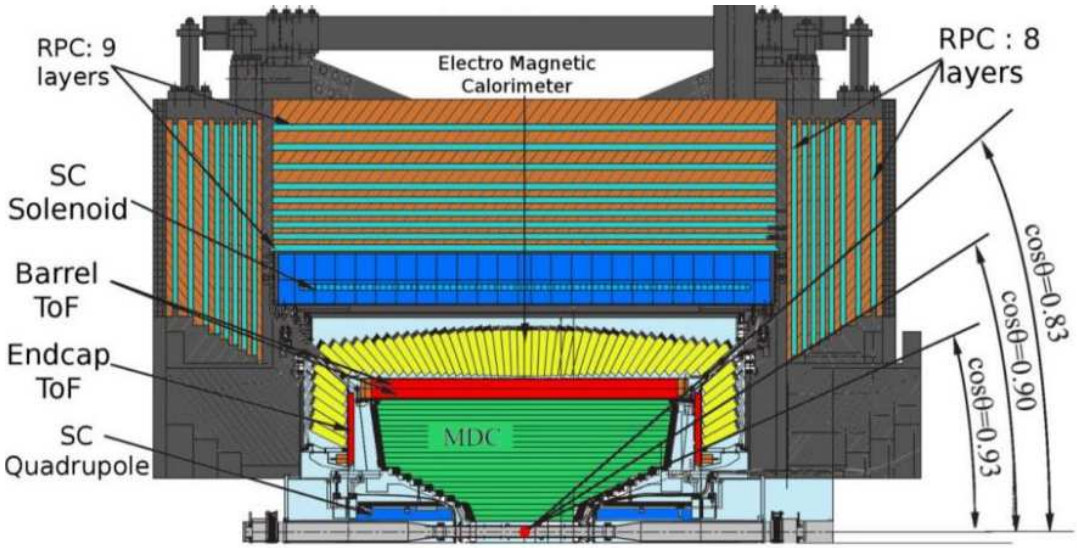

Figure 3.2: Schematic representation of the whole BESIII detector.

The Particle Identification is given by the dE/dx information from the MDC and from the time-of-flight by the TOF detectors. In the following sections, a brief description of the BESIII detector components will be presented. For more details, it is possible to refer to the BESIII NIM paper in Ref. [62].

3.2.1 Beam Pipe

The beam pipe has to host electrons and the positrons just before and during the collisions. It is located at the center of the BESIII experiment and is composed of two different parts: the central beryllium part and two supporting copper pipes. A schematic representation of the beam pipe is presented in Fig. 3.3 [65].

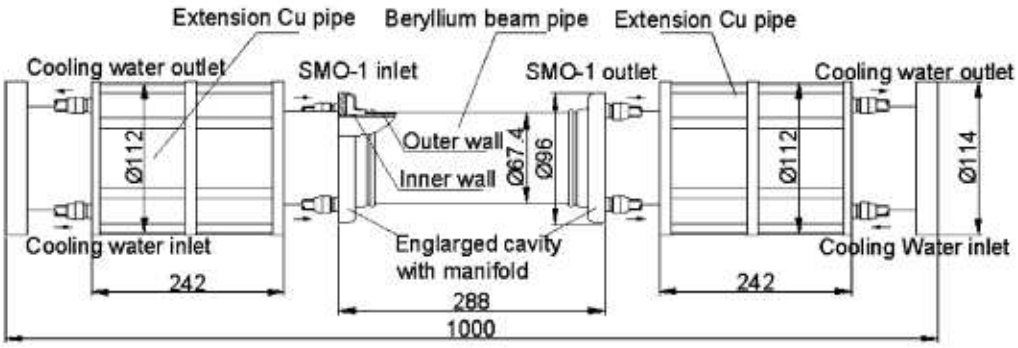

Figure 3.3: Sketch of the BESIII beam pipe.

It is designed following two leading principles: minimize the thickness of the central beryllium core, in order to minimize the multiple scattering; maximize the extension of support copper pipes, in order to shield the detector from secondary particles due to beam effect [66]. The cooling system is designed in order to control the heat coming from the pipe outer wall to the inner MDC, which is just 29.3 mm away from the beam pipe [65].

3.2.2 Multilayer Drift Chamber

The MDC is the innermost detector of the BESIII spectrometer and within the constraint of costs, material budget (to retain the performance of the calorimeter) and available space within the solenoid magnet, it has to provide a 3D tracking of charged particle, *i.e.* information where the single tracks are gone through the detector, extrapolate the points to other detectors, and identify the secondary vertices of long-lived neutral particles, *e.g.* K_S^0 or Λ. Moreover, it provides dE/dx information to contribute to the particle identification. At last, it is also used to start the L1 trigger, the first hardware-based trigger of the BESIII Data Acquisition System [67].

As for the CLEO-II Drift Chamber [68], it is composed of two separated parts sharing the same gas volume: an Inner Drift Chamber (I-DC) and an Outer Drift Chamber (O-DC). The inner part could be removed in case of radiation damage. The two parts are hold together by end-plates. A schematic representation of the BESIII MDC is shown in Fig. 3.4.

Forty three layers of sense wires are organized in order to create an almost square small cell design. Each single sense wire is surrounded by 8 field wires to create the cell. Considered the 1 Tesla magnetic field and the center-of-mass energy range provided by BEPCII, the typical momentum of the single particles will be lower than 1 GeV/c: this implies that the multiple scattering plays an important role in the determination of final spatial and momentum resolution, along with the intrinsic ones of the sense wires. In

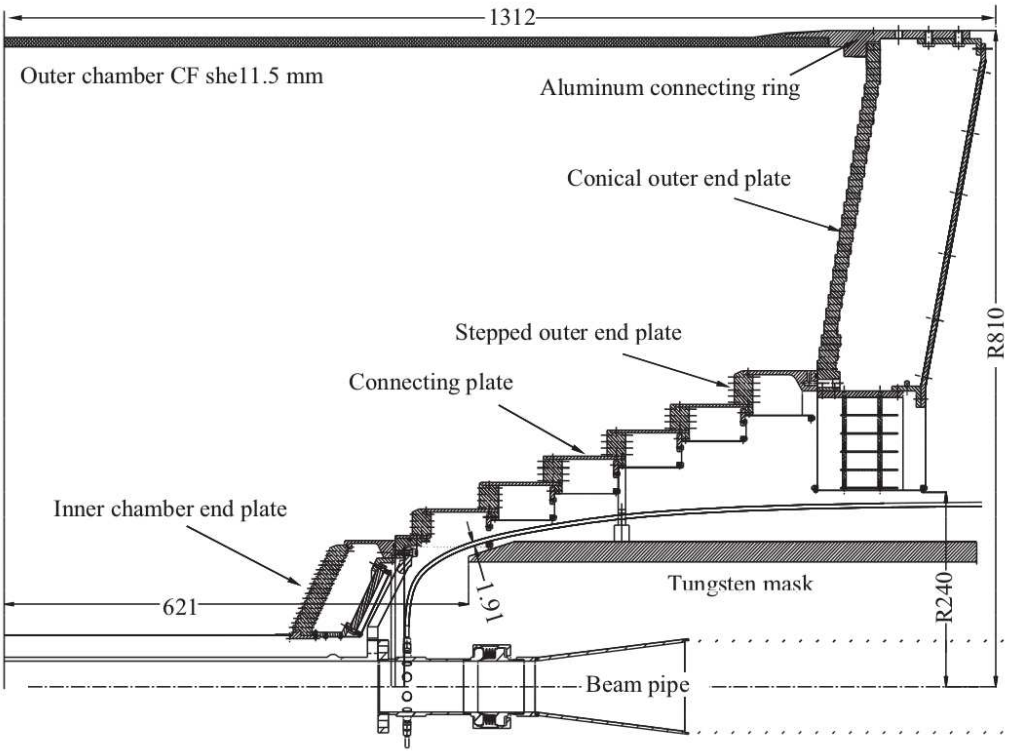

Figure 3.4: Schematic representation of the BESIII Multilayer Drift Chamber. All the quotes are expressed in mm [62].

order to guarantee the desired performance, for both energy deposition and tracking, the gas chosen is a He-based mixture (He/C_3H_8) (60/40)).

For tracking purposes the 43 layers are organized in 11 superlayers. There are 4 sense wires for each superlayer numbered between 1 and 10 and 3 sense wires for the remaining superlayers. Layers 1-8 and 21-36 have a small (few degrees) stereo angle, while 9-20 and 37-43 are axial. The single wire resolution is expected to be $\leq 130\,\mu$m in the xy plane, and around few millimeter for the z.

The expected momentum resolution can be inferred using the following formula [62]:

$$\frac{\sigma_{p_t}}{p_t} = \sqrt{\left(\frac{\sigma_{p_t}^{wire}}{p_t}\right)^2 + \left(\frac{\sigma_{p_t}^{ms}}{p_t}\right)^2} \tag{3.1}$$

where p_t is the transverse momentum of particles, $\sigma_{p_t}^{wire}$ is the momentum resolution from the uncertainties of position measurement of single wires and $\sigma_{p_t}^{ms}$ is the momentum resolution due to the multiple scattering. Each single term can be easily calculated as explained in the following lines [62]. The multiple scattering term is calculated as:

$$\frac{\sigma_{p_t}^{ms}}{p_t} = \frac{0.05}{\mathrm{B} \times \mathrm{L}} \times \sqrt{1.43 \frac{L}{X_0}} \left(1 + 0.038 \ln \frac{L}{X_0}\right) \tag{3.2}$$

where X_0 is the radiation length in meters of the material, L is the length of the track path in meters, p_t is the transverse momentum express in GeV/c, and B is the magnetic field in Tesla. On the other hand, the single wire term is calculated as:

$$\frac{\sigma_{p_t}^{wire}}{pt} = \frac{3.3 \times 10^2 \times \sigma_x}{\mathrm{B} \times \mathrm{L}^2} \times p_t \times \sqrt{\frac{720}{n+5}} \tag{3.3}$$

where B, L and p_t are defined similarly as before, while n is the total number of sense wire layers, and σ_x the position resolution of single wire in meters. By replacing $p_t = 1\,\mathrm{GeV/c}$, $B = 1\,\mathrm{T}$, $\sigma_x = 130\,\mu\mathrm{m}$, $L = 70\,\mathrm{cm}$ (for a 90° track) in Eq. 3.2 and in Eq. 3.3 is it possible to find $\sigma_{p_t}^{ms} = 0.35\%$ and $\sigma_{p_t}^{wire} = 0.32\%$. By plugging those results in Eq. 3.1, the final transverse momentum resolution for a 1 GeV/c particle is expected to be $\sigma_{p_t} = 0.47\%$. This calculation agrees with the results from Monte Carlo simulations [69].

The expected dE/dx resolution is about 6%. Several factors contribute to this result: the most relevant ones are the fluctuation of number of primary ionization along the track and the recombination losses of ion-electron pairs. Simulations shows that the achieved resolution allows 3σ π/K separation up to momenta of $\sim 770\,\mathrm{MeV/c}$ [62].

Aging problems

The inner part of the MDC is showing several issues related to an unexpected aging. The main effect is related to the very high luminosity of the BEPCII collider: with the constant of the number of collision per second, the level of radiation due to background particle intensifies. The year-by-year aging effect is depicted in Fig. 3.5a and Fig. 3.5b, where the calculations of the gain based on Bhabha events and on the gain reduction are represented respectively. From the two different calculations it is clear that the effect is increasing and it is as large as the $\sim 35\%$ reduction for the first layer till $\sim 9\%$ reduction for the eighth one [70]. In order to match a schedule that foresees BESIII detector operating since 2022, with possible extension to 2028, it has become necessary to plan for an upgrade. In 2014, the BESIII collaboration has approved the proposal to upgrade the present Inner Drift Chamber (I-DC) with a new Inner Tracker (IT) based on the Cylindrical Gas Electron Multipliers (CGEM).

The CGEM-IT upgrade

The CGEM-IT project is based on the technology of the Gas Electron Multiplier (GEMs) and it will deploy several innovations with respect the state-of-art of the gas detectors. The project, led by the Italian collaboration, is also funded by the European Commission

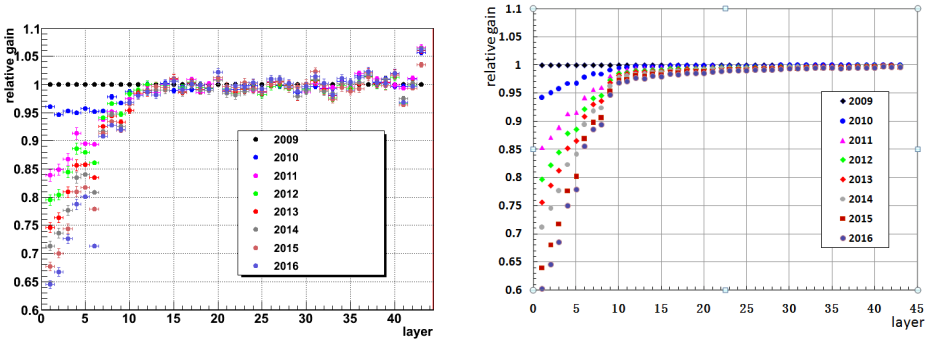

(a) Measurements with Bhabha events

(b) Measurements with accumulated charge

Figure 3.5: Relative gain with respect to the number of layers. Different colors represents different years [70].

within the 2014-RISE-MSCA-H2020 call, with the acronym BESIIICGEM. The formed consortium BESIIICGEM involves INFN Ferrara and INFN Torino, the INFN Frascati National Laboratory, Mainz and Uppsala University, and IHEP.

Gas Electron Multipliers GEMs were first developed by Fabio Sauli at CERN workshop in 1997 [71]. The multiplication structures are metal coated polymer foils (50 μm of kapton + 5 μm of copper) with small conical or by-conical holes (typical diameter 50 μm) to which a high voltage is applied. A photolitographic etching produces the holes in the copper; a second acid etching allow the holes to be extended through the kapton. With respect to traditional gas detectors, GEMs have the advantage to have lower discharge probability and reduced ions backflow [72]. In Fig. 3.6 the typical structure of the electric field inside a GEM hole is shown. The detector structure is then sandwiched in between two electrodes: the first one is at higher potential and is called called cathode; the second one is called anode and generically at ground. The anode is segmented with pads or strips on which the signal is collected.

Typical structures are with one, two or three amplification stages in between the cathode and the anode, and therefore named single, double and triple GEM detector respectively. The advantages to have multiple multiplication stages is that is possible to reach higher gains with lower voltages on the single electrode, and therefore less discharge probability, as shown in Fig. 3.7.

Figure 3.8 shows the typical structure of a triple GEM detector. It is possible to identify four gaps: the drift gap, that typically is few millimeters (5 mm in the CGEM-IT example) wide, and is the region in which the primary ionization occurs; the transfer gaps, typically 2 mm wide, where the avalanche is transferred to the next amplification stage; the induction/collection gap, typically 2 mm wide, where the avalanche induces the electrical signal on the anode circuit. In between these gaps an electric field of hun-

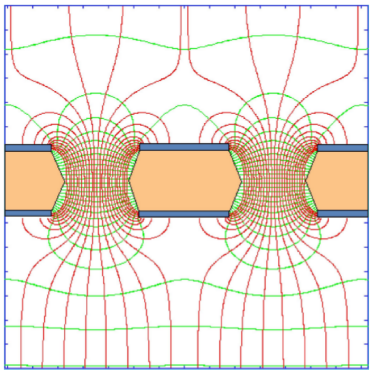

Figure 3.6: Typical structure of a single GEM hole. The blue area represents the copper deposition over the kapton (orange area). The red lines represents the electric field lines: accumulation of lines indicates an higher field [72].

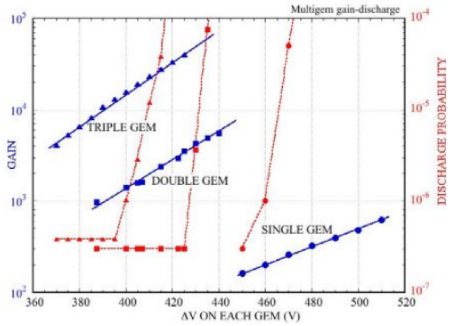

Figure 3.7: Comparison of gain (in blue) and discharge probability (in red) for single, double and triple GEM detectors. With the same voltage applied to a single GEM foil is possible to reach higher gain with the multi-stage amplification [72].

dreds of volts is applied: variations of such fields impact on the final performance of the GEM detector, as shown in Ref. [73].

Features and Innovations of the BESIII CGEM-IT The CGEM-IT project has its own origin in the Cylindrical GEM detector developed for the KLOE-2 experiment [75]. The main feature of the construction technique is derived from the expertise of the KLOE-2 collaboration. The CGEM-IT detector has to satisfy a series of requirements to match the BESIII physics need. The list is shown in Tab. 3.1.

The final detector will be composed by three layers of triple GEM detectors cylindrically shaped, for a total of 15 electrodes. A schematic representation of the detector is presented in Fig. 3.9.

The final dimensions of the detector [70] are:

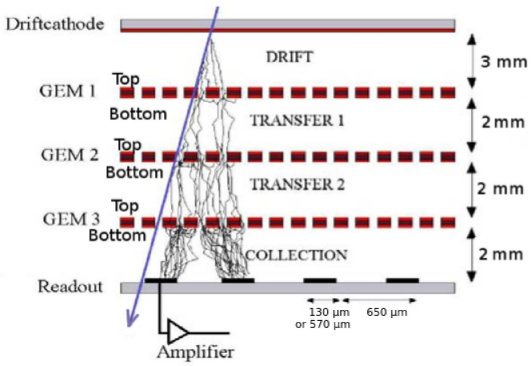

Figure 3.8: Typical structure of a triple GEM detector and the typical structure of the avalanche when no magnetic field is applied. The particle trajectory that creates the primary ionization is shown in blue [72].

Value	Requirements
σ_{xy}	$\leq 130\,\mu$m
σ_z	≤ 1 mm
dp/p @ 1 GeV/c	0.5%
Material Budget	$X_0 \leq 1.5\%$
Angular Coverage	93% of 4π
Particle Rate	$\sim 10^4$ Hz/cm^2
Minimum Radius	65.5 mm
Maximum Radius	180.7 mm

Table 3.1: List of the requirements provided by the BESIII collaboration for the new Inner Tracker.

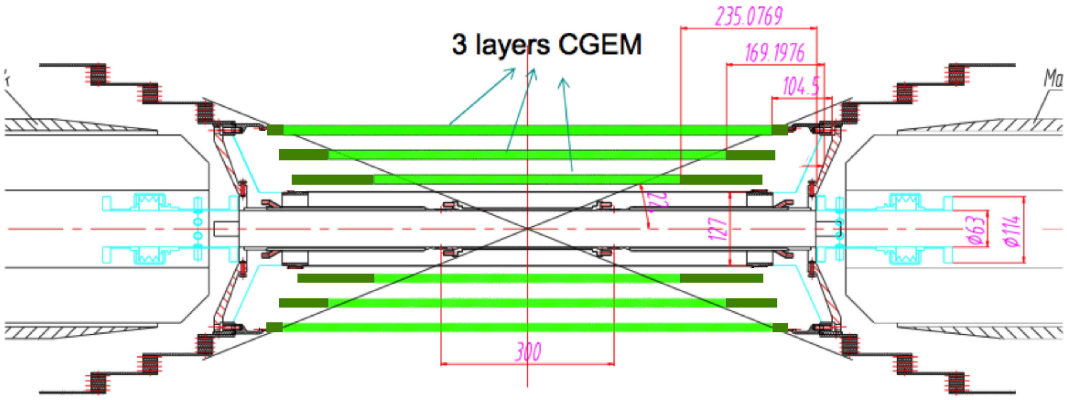

Figure 3.9: Pictorial view of the CGEM-IT detector [70]

- $R_{min} = 65.5\,mm$;
- $R_{max} = 180.7\,mm$;
- $L_{max} = 1036.6\,mm$.

In order to comply to the requirements, CGEM-IT detector deploys several innovation with respect to the KLOE-2 inner tracker and to the other planar GEM detectors:

- *Rohacell* To give mechanical rigidity to cathode and anode, a polymethacrylimide (PMI) foam, Rohacell [76], is used, instead of the classical Honeycomb material. This material is extremely light, homogeneous, and allows the single layer material budget to be only 0.4% of X_0.
- *Time and analog readout* With respect to the KLOE-II case, a time and charge readout will be used. This is the best compromise between the number of readout channels, the dimensions of the strips (pitch = 650 μm) and the final performance. This required the development of a dedicated ASIC, named TIGER (Torino Integrated GEM Electronic Readout) [77]. In fact, it is shown that only combining the classical charge centroid readout (based on the weighted mean of the charge of the strips of a cluster) and the innovative μTPC readout (based on the time of arrival of the inducted charge on the strip) is it possible to reach the required performance in the BESIII magnetic field [73].
- *Jagged readout* The anode will be also segmented in a so-called jagged configuration, as shown in Fig. 3.10. This allows to reduce the inter-strip capacitance by 30% [78]. The spatial resolution on the xy plane will match the performance of the present I-DC, while the spatial resolution along the beam axis (z coordinate) will improve till $\sim 300\,\mu$m thanks to the much larger stereo angle of the three layers ($\sim 35° - 45°$).

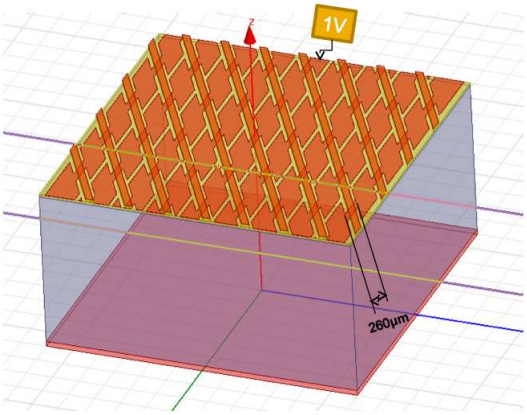

Figure 3.10: Jagged configuration for the BESIII CGEM-IT anode [78].

The detector will be installed during the 2018 summer shutdown of the BESIII experiment and it will be commissioned in the following cosmic and physics runs.

Factor	**Definition**	**Barrel** (ps)	**Endcap** (ps)
σ_i	counter intrinsic time resolution	80-90	90
σ_l	uncertainty from 15 mm bunch length	35	35
σ_b	uncertainty from the clock system	~ 20	~ 20
σ_e	uncertainty from electronics	25	25
σ_θ	uncertainty from θ-angle	25	50
σ_t	uncertainty in expected flight time	30	30
σ_w	uncertainty from time walk	10	10
$\sigma_\mathbf{1}$	**total time resolution, one layer**	**100-110**	**110**
$\sigma_\mathbf{2}$	**combined time resolution, two layers**	**80-90**	-

Table 3.2: Time resolution analysis for 1 GeV/c muons. The terms σ_1 and σ_2 are obtained from equation 3.4

3.2.3 Time-Of-Flight detectors

Time-Of-Flight (TOF) detectors along providing information for the charged-particles identification (and with some calibration also for neutron), are often used to regulate the low level trigger thanks to their quick response. The BESIII choice of plastic scintillator results from a compromise from space (the TOF is placed between the MDC and the EMC), cost and technical complexity. The space constraint prevents BESIII to use other hadron identification system as a DIRC (Doubly Imaging Ring Cherenkov) [79] or a RICH (Ring Imaging Cherenkov counter) [80] as used in BaBar or CLEO-II. The final configuration deployed is a double layer for the barrel and two single layers for the endcaps. The expected benefit in the time resolution (of the order of $1/\sqrt{2}$ factor of improvement) from the use of two single layers instead of one is not fully achieved, due to correlated error sources.

Plastic scintillator counters (BC-408 in the barrel, BC-404 in the endcaps) are used to cover a polar angle $|cos\theta| < 0.82$ in the barrel, and $0.85 < |cos\theta| < 0.95$ in the endcaps. In the barrel, 88 trapezoidal plastic scintillators are coupled with two PMTs (Hamamatsu R5924); in the endcaps, 48 scintillator counters are coupled with only one PMT and arranged in a single circular layer.

The final time resolutions σ depends from several factor and can be expressed as:

$$\sigma = \sqrt{\sigma_i^2 + \sigma_b^2 + \sigma_l^2 + \sigma_\theta^2 + \sigma_e^2 + \sigma_t^2 + \sigma_w^2}, \tag{3.4}$$

and in Tab. 3.2 all the single term are defined and an estimation of the uncertainty is given for 1 GeV/c muons. The time resolution for protons, pions and kaons is calculated to be $\sim$ 20% larger than the one for muons. As it can be seen from the table, the main difference is related to the polar angle of the track. Moreover the double layer structure of the barrel allows to reduce the final resolution combining the two layers measurements.

The π/K separation depends on the momentum and on the incident angles of the tracks. The results, based on single layer time resolution $\sigma_1 = 125\,\text{ps}$ and double layer time resolution $\sigma_2 = 105\,\text{ps}$, are shown in Fig. 3.11a, where the thick black solid line and the large black dashed line represents the single and double layer 3σ π/K separation respectively [62].

A likelihood analysis is used to estimate the particle identification capability. The results are based on $\sigma_1 = 90\,\text{ps}$ and $\sigma_2 = 120\,\text{ps}$, combined with dE/dx of the MDC assuming a 6% resolution. The results of kaons identification efficiency and kaons misidentification as pions, as function of kaons momentum, are shown in Fig. 3.11b [62].

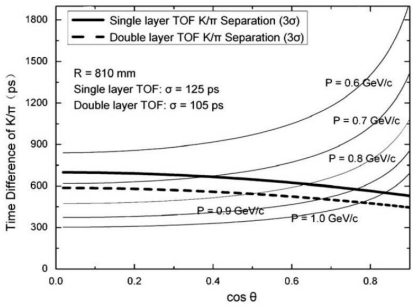

(a) π/K separation as a function of $cos\theta$ with different momentum

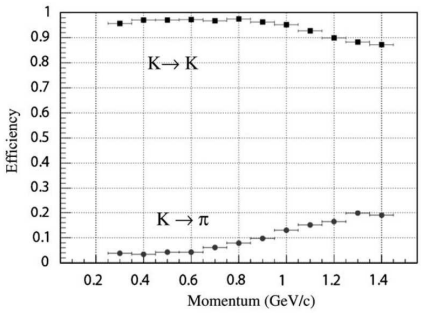

(b) K identification efficiency and misidentification rate as a function of the kaon momentum

Figure 3.11: PID performance of the BESIII TOF for π/K particles [62].

In order to improve the performance of the endcap part, a new system was installed in 2015, based on Multi-gap Resistive Plate Chambers (MRPC).

3.2.4 Electromagnetic calorimeter

The ElectroMagnetic Calorimeter (EMC) collects the information on the energy of charged and neutral particles, that live long enough to exit the TOF walls. In the physics case of BESIII it is essential to identify the radiative photons from the main charmonia and D decays and also photons from the neutral particles such π^0, η, ρ, etc. The energy range of the photons is quite wide, and ranges from the $\sim 20\,\text{MeV}$ for the more complicated decays to 2.3 GeV for the process $e^+e^- \to \gamma\gamma$. Moreover, a good design for e/π separation is needed, since both these charged tracks produce similar showers in the EMC. Finally, the position resolution is not an important constraint, but it has to provide clear separation between the γs coming from the same particle in the highest energetic case, *i.e.* the decay of a 1.5 GeV π^0, where the photons have $\sim 10°$ separation [62]. The design of a complex structure has to take in account also the cost of the production of the materials and the total dimension. For the BESIII EMC the final choice was to use sufficiently segmented CsI(Tl) crystal laced inside the superconducting

solenoid, readout by large area photodiodes [62].

The choice of CsI(Tl) crystals as scintillating material is driven by the parameters that may affect the energy resolution of the detector: primarily the shower energy leakage from backs of the crystal, the dead material between the crystals and the possible non-uniformities of the light production. The total of 6240 crystals were shaped to be 28 cm long (15.1 X_0), arranged in 56 rings (44 in the barrel, 2×6 in the endcaps). The barrel crystals point toward the interaction point, covering the angular region included in the $|cos\theta| < 0.82$, where θ is the polar angle. They have a small tilt that allows to cover 3° in both polar and azimuth direction. The endcap crystals are separated by 5 cm gaps from the barrel part to allow the support structures and the service lines of the inner detector to pass through. Therefore, the angular coverage of the endcaps parts is limited to the region $0.83 < |\cos\theta| < 0.93$.

From the performance point of view, the requirements are defined by the hit position resolution $\sigma_{x,y} \leq 6$ mm$/\sqrt{\mathrm{E(GeV)}}$ and energy resolution $dE/E \sim 2.5\%$ at 1 GeV and ~ 4 MeV at 100 MeV. The depth of the crystal is sufficient to reach the desired energy resolution at 1 GeV. Effect of transverse crystal dimensions was studied by means of Monte Carlo simulations. A segmentation of $5 \times 5\,\mathrm{cm}^2$ was chosen, since it is sufficient to match the desired spatial and energy resolution, as shown by Fig. 3.12a and Fig. 3.12b respectively.

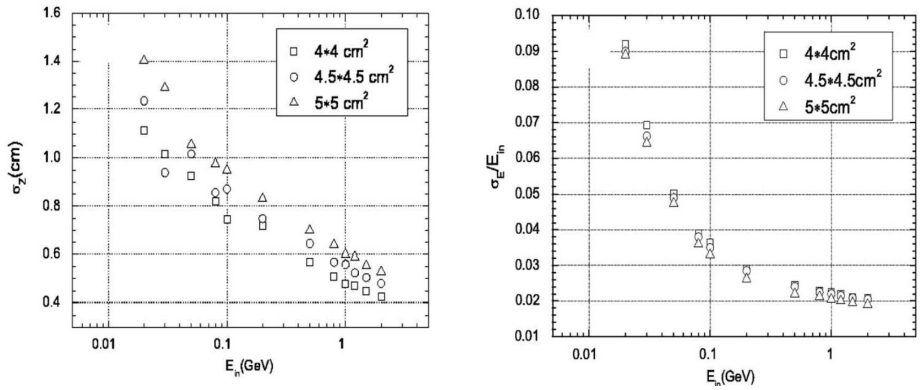

(a) Spatial resolution of the EMC with three different crystals dimension hypothesis.

(b) Energy resolution of the BESIII EMC with three different crystals dimension.

Figure 3.12: Performance at different energy values for the crystals of the EMC. Three hypothesis are shown. Squares represent the $4 \times 4\mathrm{cm}^2$, circles represent the $4.5 \times 4.5\mathrm{cm}^2$, while the triangles represent the chosen hypothesis of $5 \times 5\mathrm{cm}^2$ [62].

A summary of the parameters and performance of the BESIII EMC are listed in Tab. 3.3. The performance of the CLEO-c calorimeter are also reported as reference [62].

As a proof of the goodness of the choice, it is possible to test the π^0 mass reconstruction in a channel that can be easily identified and will provide useful information also from the

Parameter	BESIII	CLEO-c
$\Delta\Omega/4\pi$	93	93
Active media	CsI(Tl)	CsI(Tl)
Depth (X_0)	15	16
σ_E at 1 GeV (MeV)	~ 25	~ 20
σ_E at 100 MeV (MeV)	3.3	4
Position resolution at 1 GeV/c (mm)	6	4

Table 3.3: Comparison between BESIII and CLEO-c electromagnetic calorimeter. The two system shows large similarities, as expected [62].

calibration point of view: the chosen channel is $J/\psi \to \rho\pi$. The found mass resolution is measured to be 7.3 MeV, as shown in Fig. 3.13.

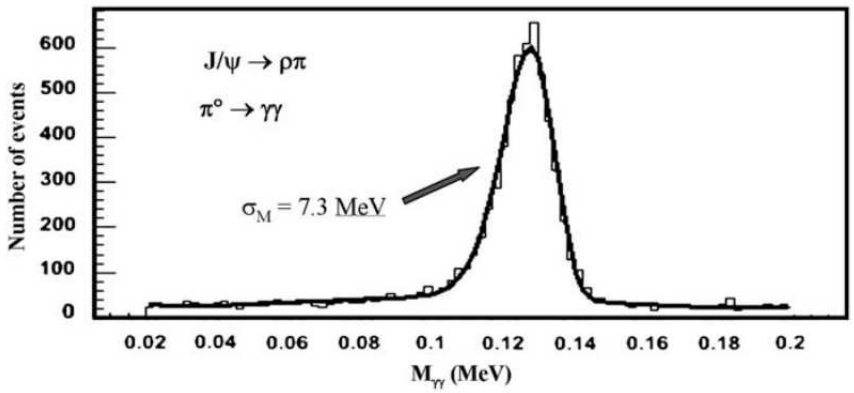

Figure 3.13: Results of the Monte Carlo study for the quality assessment of the BESIII EMC. Mass resolution of reconstructed γ pairs to form a π^0.

3.2.5 Superconductive Magnet

The 1 T superconducting solenoid magnet enables accurate measurements of charged particles produced in the collisions. The solenoid parameters are optimized to provide a uniform field for the dimension of the drift chamber. The inner diameter is limited by the dimension of the EMC. During the operation, the stored energy from the magnet is 9.8 MJ.

The steel flux return yoke is instrumented and works as absorber for hadron/muon separation. The total radiation thickness is 2.24 X_0. The forward sections can be opened to allow access to the detector. The total weight is 15 tons: the full structure operates as support for the other spectrometer components.

The mapping was performed by means of an automated field mapping device that can

move precisely in r and z direction. Three precise Hall sensors measure the three components of the magnetic field B_z, B_r and B_ϕ. The mapping was performed for seven combinations of field values of the superconductive magnet and of the superconductive quadrupoles of the beam pipe. The results for the B_z components are shown in Fig. 3.14.

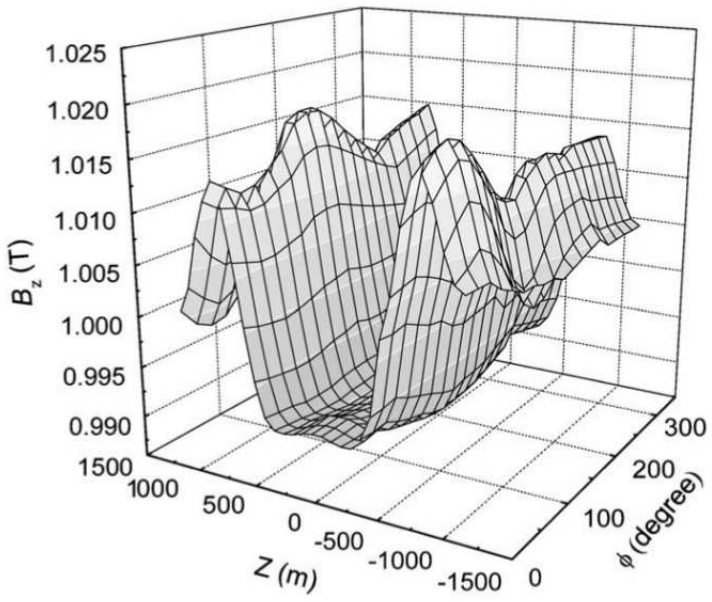

Figure 3.14: Distribution of B_z in a portion of the mapping volume.

The non-uniformity in the tracking volume is less than 2% not considering the effect of the superconductive quadrupoles; it increases up to 13% when the quadrupoles are considered, focused primarily in the region near the quadrupoles.

3.2.6 Muon Counters

The Muon Counters (MUC) are the outermost detector of BESIII spectrometer. A 3D model of the MUC is shown in Fig. 3.15.

The MUC allows to separate muons from pions and other charged tracks, whose showers are not fully contained in the EMC [62]. Indeed, muons are an important source of physics channel, since D meson decay, semileptonic decay of charmonia and τ contains at least one muon track. An example of the typical momentum range of muons in BESIII environment is shown in Fig. 3.16a and Fig. 3.16b, where it is plotted the μ momentum from D and τ decays respectively. To have a complete reconstruction of muon tracks, hits in the MUC are associated with tracks in the MDC and energy measured in the EMC; this also allow to lower the momentum cut-off, *i.e.* the minimum momentum of

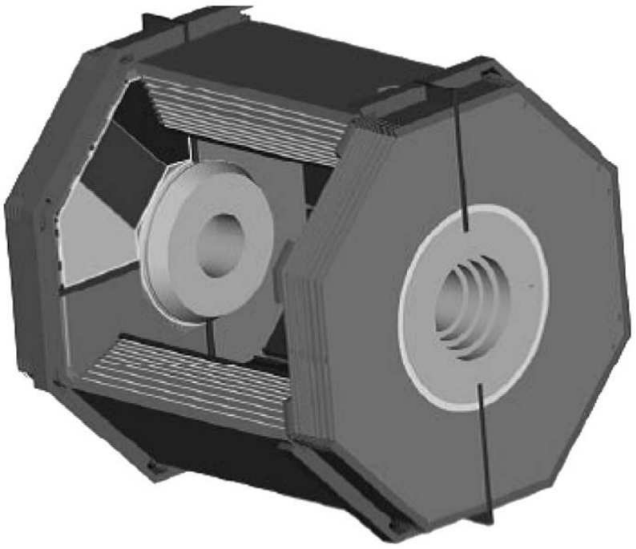

Figure 3.15: 3-dimensional model of the BESIII MUC installed in the steel return flux of the solenoid.

a muon to be identified. There are no important requirements in the spatial resolution, therefore the strip pitch is of 4 cm. However, the anode is segmented in both θ and ϕ direction, in order to provide bidimensional hits for charged tracks.

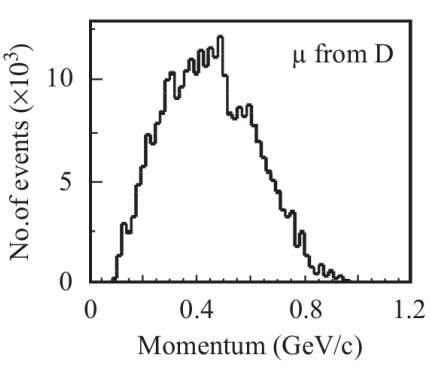

(a) μ momentum distribution from a prototype D decay at $\sqrt{s} = 3.773$ GeV.

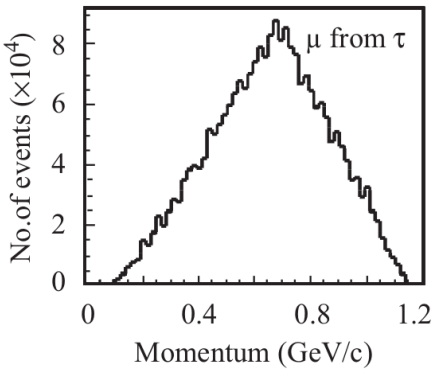

(b) μ momentum distribution from a prototype τ decay at $\sqrt{s} = 3.67$ GeV.

Figure 3.16: Momentum distribution for a muon from of typical decay from a D (left) or from a τ (right). It is important to observe the variation of the cutoff value.

In order to cover the most active area possible, the MUC detector is installed in the return flux of the solenoid magnet. Nine stations are placed in the barrel part and 8 stations are placed in the endcaps region, due to space limitations in the yoke. Technical

details of the muon detectors are shown in Tab. 3.4.

Feature	Parameters
Barrel	
Inner Radius (m)	1.7
Outer Radius (m)	2.62
Length (m)	3.94
Weight (ton)	300
Steel plate thickness (cm)	3,3,3,4,4,8,8,8,15
Single gap thickness (cm)	4
No. of RPC layers	9
Polar angle coverage	$\cos\theta \leq 0.75$
Endcap	
Inner distance to IP (m)	2.05
Outer distance to IP (m)	2.8
Weight (ton)	4×52
Steel plate thickness (cm)	4,4,3,3,3,5,8,8,5
Single gap thickness (cm)	4
No. of RPC layers	8
Polar angle coverage	$0.75 \leq \cos\theta \leq 0.89$

Table 3.4: Table of the mechanical parameter of the muon counters of BESIII Spectrometer.

They must be cost-effective and reliable, since they shall cover a very large area and are virtually inaccessible after the installation. Resistive Plate Counters (RPCs) have been chosen as active detector with innovations with respect the BaBar case [**?**]. In fact, the experience of the difficulties with linseed oil coating make the opportunity to consider new approaches in the construction of the Bakelite RPCs. The final setup was prepared with a new type of phenolic paper laminate, with the result on an improvement of the quality of the Bakelite plates with respect to the traditional RPCs.

Extensive test were performed with prototype of single gap RPCs (Fig. 3.17) with these phenolic paper laminates. The gas mixture is $Ar/C_2F_4H_2/C_4H_10$ (50:42:8). At the nominal operating working point, the efficiency is approximately 96%, with single rate $0.04\,\mathrm{Hz/cm^2}$ and dark current less than $1\,\mu\mathrm{A/m^2}$ [81].

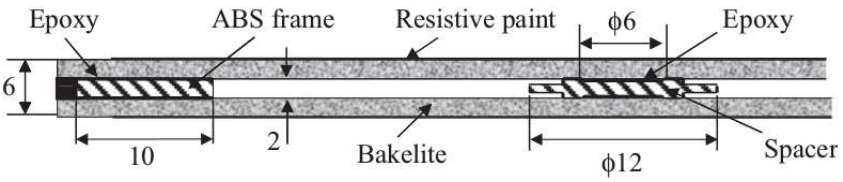

Figure 3.17: Single gap RPC cross sectional view.

Chapter 4

BESIII physics

4.1 BESIII Collaboration and dataset

In this chapter a general description of BESIII physics program will be presented. This overview aims to show the BESIII capabilities beyond this work and to introduce the main analysis topic inside the BESIII collaboration.

BESIII is expected to run until 2022, with a very likely extension up to the 2028. Since the 2009, BESIII has collected the world's largest data sample of J/ψ (1.3 billions), ψ' ($\sim$ 450 millions), $\psi(3770)$ (2.9 fb^{-1}), among other samples dedicated to the open charm and R studies. The BESIII data collected year by year is listed here:

- 2009:
  - 106M $\psi(2S)$
  - 225M J/ψ
- 2010:
  - 975 pb^{-1} at $\psi(3770)$
- 2011:
  - 2.9 pb^{-1} at $\psi(3770)$ (total 2011+2010)
- 2012:
  - 0.45B $\psi(2S)$ (total 2012 + 2009)
  - 1.3B J/ψ (total 2012 + 2009)
- 2013:
  - 1092 pb^{-1} at 4.23 GeV

  - $826\,\mathrm{pb}^{-1}$ at 4.26 GeV
  - $540\,\mathrm{pb}^{-1}$ at 4.36 GeV
  - $\sim 50\,\mathrm{pb}^{-1}$ at 3.81, 3.90, 4.09, 4.19, 4.21, 4.22, 4.245, 4.31, 4.39, 4.42 GeV
- 2014:
  - $1029\,\mathrm{pb}^{-1}$ at 4.42 GeV
  - $110\,\mathrm{pb}^{-1}$ at 4.47 GeV
  - $110\,\mathrm{pb}^{-1}$ at 4.53 GeV
  - $48\,\mathrm{pb}^{-1}$ at 4.575 GeV
  - **$567\,\mathrm{pb}^{-1}$ at 4.6 GeV**. This is the data sample that will be used for this work.
  - $0.8\,\mathrm{fb}^{-1}$ R-scan from 3.85 to 4.59 GeV (104 points)
- 2015:
  - R-scan from 2 to 3 GeV
  - 2.175 GeV data
- 2016:
  - $\sim 3\,\mathrm{fb}^{-1}$ at 4.18 GeV
- 2017:
  - $7 \times 500\,\mathrm{pb}^{-1}$ between 4190 and 4280 MeV, 10 MeV step.
  - χ_{c1} scan
  - X(3872) scan
- 2018 (expected):
  - J/ψ
  - τ scan
  - ψ' scan for relative phase measurements.

4.2 BESIII Physics Program

The BESIII physics program can be roughly divided in five topics: Charmonium spectroscopy, Open Charm decay, Light hadron spectroscopy, τ-R-QCD studies and, since

a few years, also New Physics searches. For more detailed description of the BESIII physics goal, it is possible to refer to the BESIII physics book [82].

4.2.1 Charmonium spectroscopy

Firstly hypothesized by the Glashow-Iliopoulos-Maiani (GIM) mechanism [7], the existence of the charm quark was confirmed by the J/ψ discovery in the early 70s [83], [84]. Almost immediately after, also the first radial excitation the $\psi(2S)$ was discovered [85]. The discovery of two resonances in the charmonium spectrum confirmed the possibility to describe these states similarly to what is done in the atomic structure, with a proper spectroscopy. Thus, it was possible to predict other states. This very simplified model worked great until the beginning of the new century, up to the belief that all the missing states were just not yet appeared by the limited statistics available. The experimental of the charmonium spectroscopy at the beginning of the 2003 is shown in Fig. 4.1.

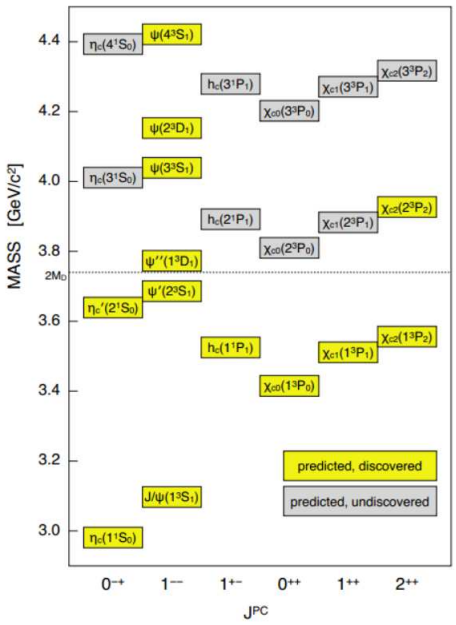

Figure 4.1: Charmonium spectrum at the beginning of the 2003. The yellow states are the discovered and the grey states represents the missing ones.

In 2003, the discovery from BELLE Collaboration of a very narrow resonance above the open charm threshold decaying mostly in $\pi^+\pi^- J/\psi$ changed the picture completely [22]. The $X(3872)$, as it is called nowadays, was only the first of several new states unpredicted by the simple Quark Model. Most of these states shows exotic features (charged charmonia, decay preferentially in other charmonia, instead of into charmed mesons) and nowadays they are grouped with the name of XYZ states. Even if several models that tries to explain the nature of the these states are available as it will be shown

in Appendix A, none can completely explain the full picture. The updated charmonium spectrum including exotic states can be seen in Fig. 4.2.

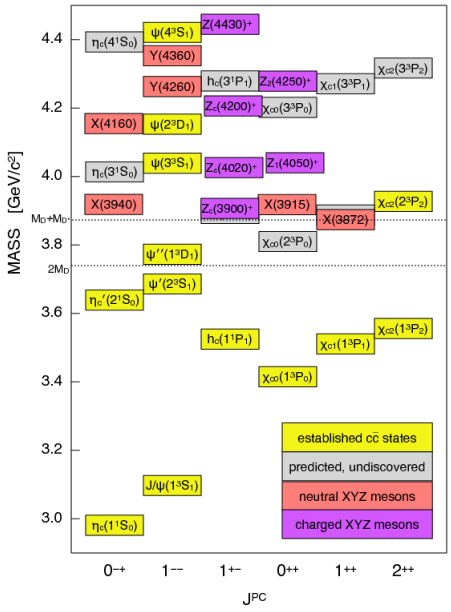

Figure 4.2: Charmonium spectrum updated in the 2015. The states are divided in: established charmonia (yellow boxes); predicted but undiscovered charmonia (grey boxes); neutral unpredicted but observed XYZ states (red boxes); charged unpredicted but observed XYZ states (purple boxes). It is possible to notice that all the unpredicted states lay over the DD^* threshold.

The role of the BESIII in the charmonium spectroscopy is dual. On one side it contributes to study the conventional states, measuring with unprecedented precision the cross sections and showing the transitions between the different charmonia. This allows to strengthen the knowledge of the charmonium potential and our ability to make predictions. Recent examples can be found in Refs.[86], [87], [88]. On the other side, it is one of the top player in the search for these new states, taking profit of the possibility to produce directly the states with $J^{PC} = 1^{--}$, like $Y(4260)$. This allows BESIII to study the transition among these states and the cross section at different energy values, in order to determine the lineshape and possible connection among them. In 2013, BESIII discovered the $Z_c(3900)^+$ the first charged charmonium-like state [45], and more recently has also measured its quantum numbers [49].

4.2.2 Open Charm decays

In the past the study of the open charm mesons seemed to have a mere interest for the mathematical point of view, since most of the more interesting phenomena that happens

in B meson physics (Cabibbo-Kobayashi-Maskawa transition, CP violation, $D^0 - \bar{D}^0$ oscillation) are weak or very small in D spectrum [82]. However, the interest in the field grew in the recent years. On one side the discovery of the D_{sj} states [**?**] revived the interest in the charmed meson spectroscopy. On the other side, being the weak forces well-known in the SM, it is possible to reach unprecedented precision in the study of the interplay between strong and weak interaction. Moreover, the tools developed for the B physics can be tuned and employed in an environment with less background. In addition, thanks to the high luminosity of the e^+e^- colliders it is possible to be sensitive to discrepancy between the SM prediction and experimental data, which can give access to New Physics. Finally, precision knowledge of the D/D_s mesons decays can reduce the systematics of the measurement in the B meson sector [82].

BESIII has collected data at the $\psi(3770)$ resonance peak for the studies of the D mesons, while has collected two samples dedicated for the D_s studies, one at 4.09 GeV (also used for the XYZ studies) and a larger sample ($3\,\text{fb}^{-1}$) at the $D_sD_s^*$ threshold at 4.18 GeV. An idea of the impact of BESIII searches in the D physics is shown in Fig. 4.3, where is highlighted the BESIII contribution to the CKM matrix element V_{cd} with respect to the other experiments.

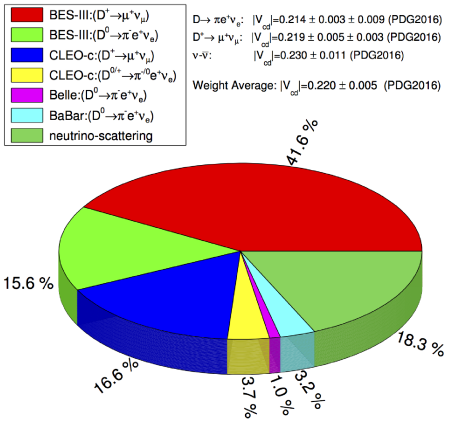

Figure 4.3: BESIII contribution to V_{cd} CKM matrix as extracted from the PDG2016 [24].

If the charmed meson are well studied, the situation is quite different for the charmed baryons. Many state have been observed in few final states and have branching ratio relative to golden channels [24]. When BESIII started the Λ_c in 2014, the knowledge of the lightest charmed baryon was limited: only the golden channel $\Lambda_c \to pK^-\pi^+$ was studied with high precision; no final state involving a neutron was observed.

Originally BEPCII center of mass energy was not able to reach the energy of the $\Lambda_c\bar{\Lambda}_c$ threshold. Eventually, BEPCII was upgraded and BESIII collected 4 samples just above the threshold. The largest samples has an integrated luminosity of $567\,\text{pb}^-1$ is just 24 MeV above threshold, at 4.6 GeV. The study of the charmed baryon pairs at threshold

has the opportunity to raise the efficiency by reconstructing only one side of the decay: the presence of the anti-particle in the other side of the decay is guaranteed by the charm quantum number conservation. On the other hand, the background level also increases.

Taking profit of these features, despite the smaller statistic with respect to the B-factories, in the time span of just two years, BESIII has started playing a major role in the Λ_c physics. It has recently reported the direct measurement of the branching fraction of several Cabibbo-Favorite final states for the first time, and has improved the precision of the golden channel [89]. Moreover, it has recently observed, for the first time, a final state involving a neutron [90]. These are just few examples of the capabilities of BESIII experiment. The work presented in this thesis is a further example of such physics reach.

4.2.3 Light hadron spectroscopy

Light hadron spectroscopy is a broad sector which includes the search for glueballs, the characterization of η/η', the search for new resonances of conventional baryon and meson. The common point of all these different branches is the interpretation of the strong interaction in the low energy regime, where the perturbative approach cannot be extended. The involved valence quarks (u, d, s) have very low mass compared to the $\Lambda_{\rm QCD}$, so their features have to be modeled with phenomenological models, such as the Chiral Perturbation Theory (ChPT) [91], Vector Meson Dominance [92] or the Lattice QCD [93].

BESIII light hadron spectroscopy program takes advantage of the world's largest sample of J/ψ and $\psi(2S)$, whose decays are gluon-rich, due to the absence of any connected diagram with these charmonia with other lower mass states (*e.g.* ϕ, ω, ρ). An example of the possibility in the search of glueballs is shown in the study of the partial wave analysis of $J/\psi \to \pi^0\pi^0$ [94].

One of the most peculiar studies of BESIII light hadron spectroscopy is the search of the exotic $X(1835)$. This state was first observed in the radiative decay $J/\psi \to \gamma\eta'\pi^+\pi^-$ by BESII [95], and then confirmed by BESIII [96]. Later, the spin-parity of this state was determined to be $J^{PC} = 0^{-+}$. In addition, a plethora of different states, with similar masses and widths were observed; Fig. 4.4 shows a summary plot of these states. The most intriguing one is the $X(p\bar{p})$, shown as enhancement at threshold of the process $J/\psi \to \gamma p\bar{p}$ by BESII [97] and later confirmed by BESIII [98] and CLEO [99].

In order to understand the nature of the $X(1835)$ and to prove the interplay between the $X(1835)$ and the $X(p\bar{p})$, a study of the $\eta'\pi^+\pi^-$ lineshape around the $p\bar{p}$ threshold was performed [100]. Even if the statistics is very large, the result provides two ambiguous solutions: a threshold effect, and the interference between a narrow and a wider resonance. In order to disentangle between the two results and to extend other searches, a

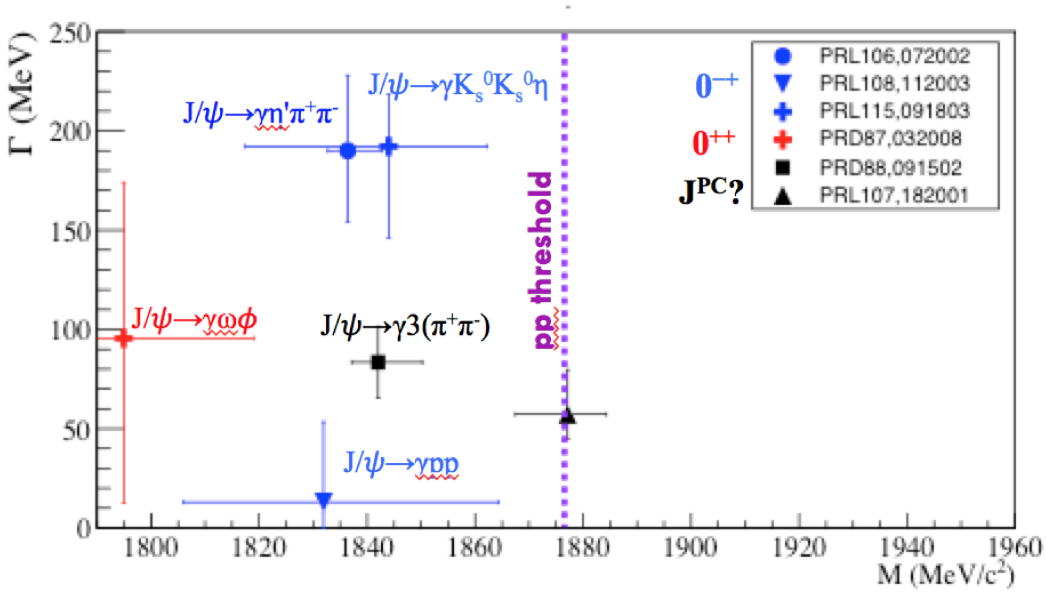

Figure 4.4: Summary plot of the BESIII studies on the $X(18xx)$ searches. The states in blue have a spin-parity assigned to be $J^{PC} = 0^{-+}$, while the state in red have spin-parity assigned to be $J^{PC} = 0^{++}$. The black states have no assigned spin-parity.

further data taking of about ten times the present statistics will undergo in the next few years (roughly $1\,\text{fb}^{-1}$ per year, for 3/4 years).

One interesting feature is the possibility to profit from the radiative decay $J/\psi \to \gamma\eta/\gamma\eta'$ to produce a large number of η/η' (roughly 6×10^6 η' in the BESIII data). This large sample can be used to study the properties of the mesons, in order to deepen the knowledge around these particular particles, *e.g* to fully understand the mixing between these two states and the dynamics of their three body decays. Few examples of the most interesting results are shown in Refs. [101], [102].

4.2.4 τ, R and QCD studies

A working group is dedicated to precise measurement of different key parameters of the Standard Model (τ properties, muon anomalous magnetic moment) and of the QCD perturbative (R value) and non-perturbative (relative phase of charmonia) regime.

Even though the QCD is a theory well tested, there are still several parameters that require extremely precise measurements: BESIII can measure with unprecedented precision hadronic contribution to the muon anomalous magnetic moment. A working group is dedicated to such precise studies in both the perturbative and non-perturbative part of the QCD spectrum.

While electrons and muons properties are well understood, τ leptons are less known. The measurements are quite complicated, since τ can decay hadronically into a large number of different final states, being heavier of many hadrons (M_τ: $(1776.86 \pm 0.12)\,\mathrm{MeV/c^2}$): the dominant decay mode is $1-$ prong that corresponds to roughly the 85% of the total branching ratio [24],followed by the decays to $3-$ and $5-$ prongs. The main difficulty is the presence of at least one neutrino in each decay (ν_τ, for lepton number conservation), so the kinematics can not be fully closed, leading to lower precision in the measurements. BESIII took advantage of the possibility to produce the τ pairs near or at threshold, and scan the lineshape to precisely measure the mass opening providing, the most precise single measurements of the τ lepton mass. [103]. A new data taking is scheduled in 2017-18 data taking in order to further improve this measurement.

In the early years of the study of the strong interaction, a key measurement was the ratio between the $e^+e^- \to hadrons$ and the $e^+e^- \to \mu^+\mu^-$, named R value. By studying this ratio, physicist confirmed the existence of a further degree of freedom, the color, and thus the first confirmation of the theory that nowadays is known as Quantum Chromo-Dynamics. After more than 40 years, the precise measurement of this ratio it is still an important parameter to study the QCD and spot any possible discrepancy leading to New Physics beyond the Standard Model. In Fig. 4.5 it is shown the status of the R measurement from PDG2017 [24]. BESIII can study the ratio in the energy interval from 2 to 4.6 GeV, and thus verify the prediction below, around and above the opening of the charm quark production.

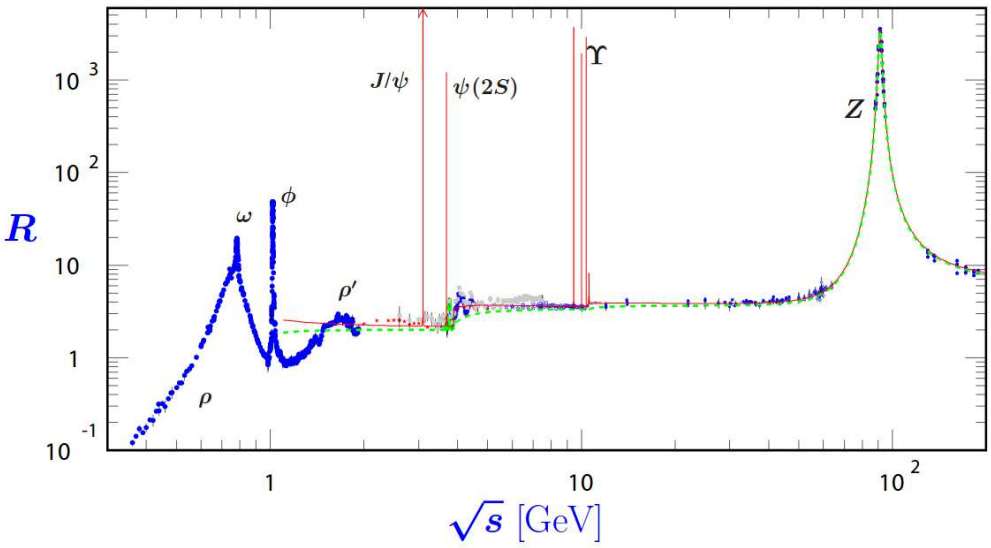

Figure 4.5: Measurement of the ratio of inclusive production cross section of hadrons over the exclusive $\mu^+\mu^-$ cross section in e^+e^- annihilation in the energy range from 0.1 MeV to Z mass peak.

4.2.5 New Physics searches

Although the Standard Model represent the most complete theory to understand the world at quantum level, there are several pieces of evidence that show that there are still some open points that are not fully understood, *e.g.* neutrino masses, naturalness, dark matter, dark energy, completeness. The typical energy regime in which such questions can be answered is usually placed between $\sim 1\,\text{TeV}$ and $\sim 100\,\text{TeV}$. This leaves most of these searches to the high energy accelerators, like LHC, and in the future to the possibly-forthcoming Circular Electron Positron Collider (CepC) in China, International Linear Collider (ILC) in Japan and Future Circular Collider (FCC-hh) at CERN.

However, in recent years, thanks to the high luminosity of the e^+e^- colliders, test for new Physics became available also for the low energy regime. Among the different theories, one foresees the existence of a massive partner of the photon, called Dark Photon [104]. This new vector boson behaves as a portal between standard and dark particles, couples directly to the SM photon [105], and can decay both in SM electron or in supersymmetric partners, like the neutralino or the WIMPs (Weakly Interacting Massive Particles). BESIII can profit of the Initial State Radiation (ISR) from the $\psi(3770)$ and search for $\gamma_{ISR}l^+l^-$ in the mass range from 0.8 to 3.5 GeV/c^2. Since both the mass and the strength of the interaction are free parameters of this model, the results are given always as a combination of the mass and the possible interaction strength. The BESIII most recent results [106] in this topic are shown in Fig. 4.6. Since no observations of such dark photon have been made so far, the band represents exclusion regions from each experiment. As it can be seen, the available phase space for the parameters is rapidly narrowing, and also the models in which the dark photon was used to describe the anomalous magnetic moment of the muon [107] seems disfavoured by the present data.

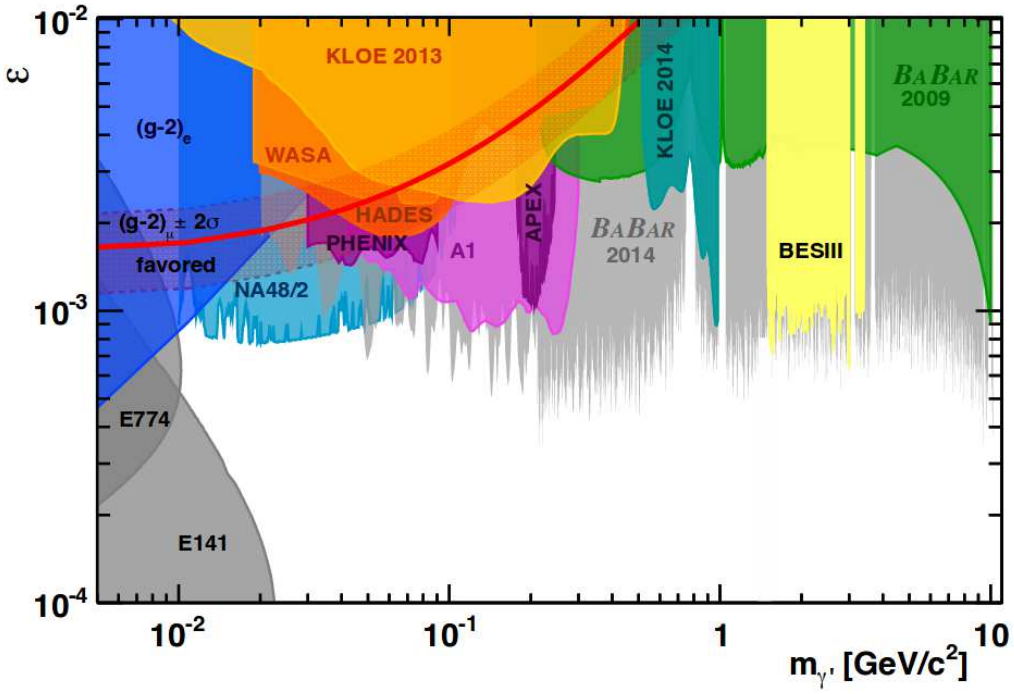

Figure 4.6: Exclusion limit plot for the searches of dark photon for different experiments extracted from the most recent work of BESIII on the topic [106]. The red band represent the 2σ expected region of mass and strength that can be used to justify the discrepancy between the Standard Model calculation [107] and the experimental value of the anomalous magnetic moment of the muon.

Chapter 5

Data Analysis

In this chapter we present the search for the hidden-strangeness pentaquark in $\Lambda_c \to p\phi\pi^0$. This analysis is performed using the data collected by the BESIII experiment at around 4.6 GeV. The data were analysed with the BES Offline Software System (BOSS), in which it is also possible to generate the physical events, simulate their passage through the detector, reconstruct and perform their analysis. The detector simulation is done using GEANT4 [108]. Both exclusive and inclusive Monte Carlo (MC) samples are produced by means of BesEvtGen [109], an extension of EvtGen generator [110]. These samples are used to estimate the background, the efficiency and the systematical errors due to the difference between the real data and simulations.

5.1 Data samples

The available data sample is $\mathcal{L} = 567\,\mathrm{pb}^{-1}$. This sample was collected in 2014, and it is just few MeV above the $\Lambda_c\bar{\Lambda}_c$ threshold. It is the largest sample of four collected by the BESIII collaboration dedicated to the Λ_c baryon physics program. The inclusive Monte Carlo produced by the BESIII collaboration and it is composed by:

- $\Lambda_c\bar{\Lambda_c}$ (with no signal $\Lambda_c \to p\phi\pi^0$).
- $q\bar{q}$
- $D\bar{D}$
- ISR
- $\tau^+\tau^-$

For the purpose of this analysis, the decay mode of the process under study can be represented following this chain of two decays: $\Lambda_c \to P_s^+\pi^0$, $P_s^+ \to p\phi$. Throughout the

text, charge conjugation is implied. The ϕ meson is reconstructed via the decay mode $\phi \to K^+K^-$ (BR $= (48.9 \pm 0.5)\,\%$) [24] and the π^0 in the $\pi^0 \to \gamma\gamma$ decay.

Both the resonant and the non-resonant process are generated exclusively with BesEvtGen as follows:

- 50k (resonant) $e^+e^- \to \Lambda_c\bar{\Lambda}_c$, $\Lambda_c \to P_s^+\pi^0$, $P_s^+ \to p\phi$, $\phi \to K^+K^-$, $\bar{\Lambda}_c^-$ inclusive;
- 50k (resonant) $e^+e^- \to \Lambda_c\bar{\Lambda}_c$, $\Lambda_c \to P_s^+\pi^0$, $P_s^+ \to p\phi$, $\phi \to K^+K^-$, $\bar{\Lambda}_c^-$ semileptonic. (referred to in the text as signal shape exclusive MC);
- 200k (non-resonant) $e^+e^- \to \Lambda_c\bar{\Lambda}_c$, $\Lambda_c \to p\phi\pi^0$, $\phi \to K^+K^-$, $\bar{\Lambda}_c^-$ inclusive.

5.2 Event Selection

5.2.1 Analysis Strategy

Data just above a threshold opening offer different opportunity: the background production is kept under control and the environment is quite clean. In our case the kinematic allows only the production of the Λ_c pair, therefore it is possible to reconstruct only one side of the event, ignoring the other side. This approach is called *Single Tag*. This technique allows to keep a higher efficiency. In this particular case, it is possible to reconstruct the Λ_c^+ side, and neglect the $\bar{\Lambda}_c^-$ side, as depicted in Fig. 5.1.

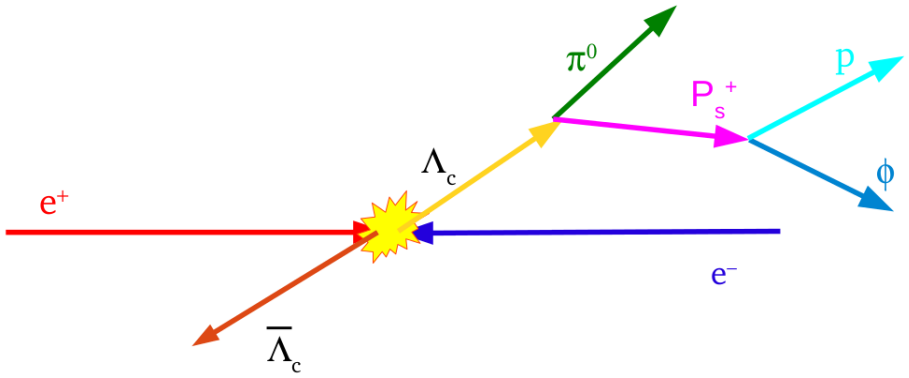

Figure 5.1: Pictorial representation of the single tag procedure. It is possible to "look" only in the Λ_c^+ side, neglecting what happens in the $\bar{\Lambda}_c^-$ side.

Two important variables, defined in the center of mass frame, are used to select the events and are here explained. The first one is named dE, that is defined as:

$$dE = E_{candidate} - E_{beam},$$

where E_{beam} is the energy of the beam and $E_{candidate}$ is the total energy of the reconstructed Λ_c candidate. The other one is called M_{bc}, mass beam constrained, is defined

as:

$$M_{bc} = \sqrt{E^2_{beam} - p^2_{candidate}},$$

where E_{beam} is again the energy of the beam, while $p_{candidate}$ is the three-momentum of the reconstructed Λ_c candidate. In the MC simulation, the value of E_{beam} is set at 2.3 GeV, while for real data the measured value of E_{beam} is extracted from the database. An example of how the M_{bc} signal shall appear against a background is shown in Fig. , where the green histogram is a signal MC, while the blue and the red ones are full background (in the $\Lambda_c \bar{Lambda}_c$ sample there is no signal).

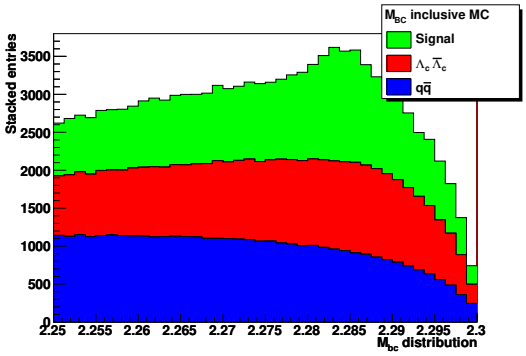

Figure 5.2: Distribution of the M_{bc} variable. It is possible to observe a clear separation between signal and background behaviour.

One of the results of this that can be derived from this analysis is the branching ratio (BR) of the process. The formula to extract the branching ratio is the following:

$$\mathrm{BR}(\Lambda_\mathrm{c} \to \mathrm{P_S}\pi^0) = \frac{N_{evt}}{\mathcal{L}\,\sigma(e^+e^- \to \Lambda_c^+\bar{\Lambda}_c^-)\,\varepsilon\,\mathrm{BR}(\phi \to \mathrm{K^+K^-})} \tag{5.1}$$

where N_{evt} is the number of the event in the real data, $\mathcal{L}$ is the luminosity, $\sigma(e^+e^- \to \Lambda_c^+\bar{\Lambda}_c^-)$ is the production cross section for a pair of Λ_c at the center of mass energy, ε is the efficiency extracted from the non resonant exclusive MC and $\mathrm{BR}(\phi \to \mathrm{K^+K^-})$ is the branching ratio for the decay of a ϕ into a pair of kaons.

5.2.2 General Selection

The analysis plan is to perform a single tag analysis. The focus of the selection is to keep the efficiency as large as possible.

It is possible to define a set of general selection criteria:

- at least 3 charged tracks;

  to be a good charged track:

  - $|\cos\theta| < 0.93$, where θ is polar angle,
  - $\mathrm{R_{xy}} < 1\,\mathrm{cm}$, where $\mathrm{R_{xy}}$ is the track vertex distance from the interaction point in the xy plane
  - $\mathrm{R_z} < 10\,\mathrm{cm}$, where $\mathrm{R_z}$ is the track vertex distance from the interaction point along the beam line direction
  - there must be at least 2 positive tracks (p and K) and at least 1 negative track (K).

- at least 2 good photons;

  a good photon is defined as:

  - $\mathrm{E_{raw}} > 25\,\mathrm{MeV}$ in barrel ($|\cos\theta| < 0.80$) and $E_{raw} > 50\,\mathrm{MeV}$ in end caps ($0.86 < |\cos\theta| < 0.92$), where E_{raw} is the energy deposit of the shower in the EMC crystals;
  - At least 5° between a shower in the electromagnetic calorimeter and the closest charged tracks.
  - $0 \leq \mathrm{t_{TDC}} \leq 14$, where t_{TDC} is the time of the arrival of the signal in unit of 50 ns.

these selections are used to suppress most of the events totally unrelated to the final state of interest.

The BESIII standard particle identification (PID) is used [111]. The particle identification capability is calculated with a likelihoo analysis. The K/π separation is around 95% and the contamination is about 5% for momenta up to 0.9 GeV/c. The dE/dx, $\mathrm{TOF_1}$, $\mathrm{TOF_2}$ and $\mathrm{TOF_E}$ systems are used in the procedure. The PID is used to distinguish between protons, kaons, and pions. To be identified as proton, the candidate must satisfy:

- Probability of being a proton is larger than 0.001 (Prob(p) > 0.001);
- Probability of being a proton is larger than probability of being a pion (Prob(p) > Prob(π));
- Probability of being a proton is larger than probability of being a kaon (Prob(p) > Prob(K)).

Similar selection criteria are used for the kaons. Only one of the two kaons (positive or negative) used at this stage is identified as a kaon by BESIII PID systems. The other one is a charged track with the mass hypothesis of being a kaon. This is meant to keep a higher efficiency level.

The channel $\Sigma^+\phi$ has the same final state as our channel. To reject the final state a cut over the mass of the $p\pi^0$ is applied: following what is done in other standard BESIII analyses, the region excluded is $[1174, 1200]\,\mathrm{MeV/c^2}$ [112].

5.2.3 Selection

A loop over all the γ pairs is performed, and all the possible candidates are stored. In order to find the best Λ_c candidate, all the possible combinations of π^0, K^+, K^- and p are used. The one that minimizes the dE variable is kept for further studies.

The signal region for the mass of the π^0 and ϕ are identified from exclusive measurements MC. The π^0 invariant mass is shown in Fig. 5.3 along with the fit. The sum of a Crystal Ball (CB) function plus a first order polynomial is used to fit the distribution. The usage of the Crystal Ball is suggested by the asymmetric radiative tail. The results of the fit are the following: mass $m_{\pi^0} = (133.4 \pm 0.2)\,\mathrm{MeV/c^2}$, width $\sigma_{\pi^0} = (2.7 \pm 0.2)\,\mathrm{MeV}$. The signal region is identified asymmetric in the range $[110.0, 150.]\,\mathrm{MeV/c^2}$.

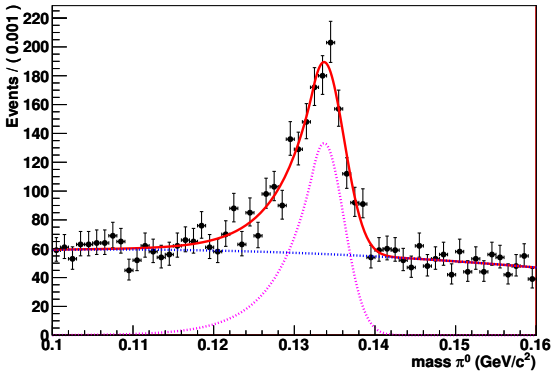

Figure 5.3: Invariant mass distribution of the γ pairs to form π^0 mass. The red line shows the fit, the black dots the exclusive resonant MC, while the magenta and the blue dotted lines represent the signal CB and the polynomial background respectively

In order to reduce the combinatorial background, only the events with the invariant mass of the kaon pairs m_{KK} around the ϕ mass known from the PDG [24] are kept, *i.e.* $0.98 < m_{KK} < 1.08$. Fig. 5.4 shows the invariant mass found. To fit the distribution, a sum of a convolution of a a non-relativistic Breit-Wigner (BW) and a Gaussian probability density function (PDF) for the signal and a first order polynomial for the combinatorial background is used. The convolution is used since takes in account both the natural width of the ϕ meson and the detector resolution, that are comparable in the ϕ meson case. The formula used for the non-relativistic Breit-Wigner is

$$\frac{1}{(E-M)^2 - (\Gamma/2)^2} \tag{5.2}$$

where E is the center of mass energy, M, Γ are the mass and the width of the resonance to be extracted in the fit respectively. In the fit, the width of the ϕ is fixed to the PDG value [24].

The results are found to be: mass $m_\phi = (1019.38 \pm 0.07)\,\mathrm{MeV/c^2}$, resolution $\sigma = (2.1 \pm 0.1)\,\mathrm{MeV}$. The signal region is identified as a symmetric interval around the mass, *i.e* $[0.999, 1.039]\,\mathrm{MeV/c^2}$.

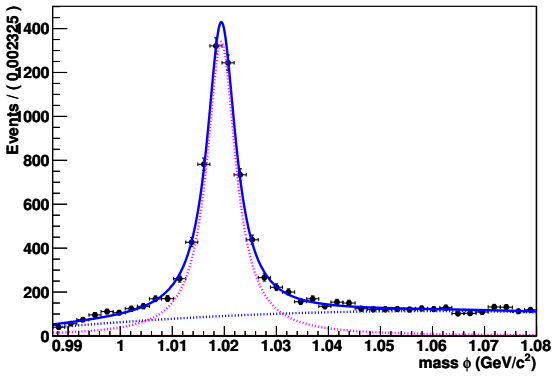

Figure 5.4: Invariant mass distribution of the KK pairs to form the ϕ mass. The blue line shows the fit, the black dots the exclusive resonant MC, while the magenta and the blue dotted lines represent the signal BW and the polynomial background respectively

After applying the cuts for the π^0 and ϕ, it is possible to define the M_{bc} signal region. The remaining events are shown in Fig. 5.5. The distribution is fitted to a convolution of the dedicated signal shape exclusive MC and a Gaussian to take for the detector resolution in account. The whole interval between $2.25\,\mathrm{GeV}/c^2$ and $2.3\,\mathrm{GeV}/c^2$ is taken as the signal region.

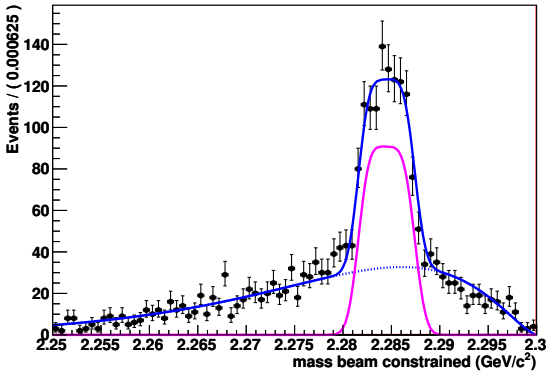

Figure 5.5: Invariant mass distribution of the M_{bc}. The blue line shows the fit, the black dots the exclusive resonant MC, while the magenta and the blue dotted lines represent the signal BW and the Argus background respectively

The last distribution analysed is the dE one. In order to define the signal region, a Crystal Ball (CB) convoluted with a Gaussian probability density function is used to

fit the exclusive MC. Fig. 5.6 shows the corresponding distribution. The solid blue line represents the fit, while the black dots are the events of the resonant exclusive MC simulation. The results of the fit are the following: mean $\mu_{dE} = (-2 \pm 2) \cdot 10^{-5}\,\mathrm{GeV}$ and sigma $\sigma_{dE} = (4.3 \pm 0.5) \cdot 10^{-3}\,\mathrm{GeV}$. The signal region is taken within the interval $[-2.02, 2.02] \cdot 10^{-2}\,\mathrm{GeV}$.

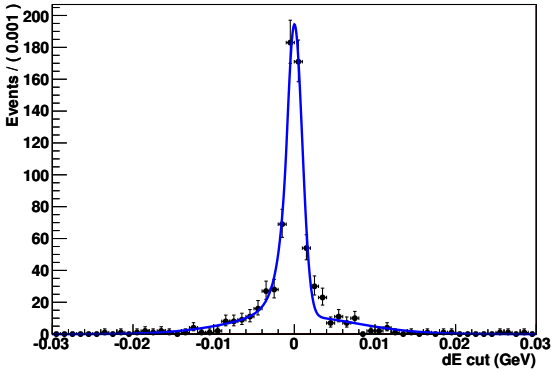

Figure 5.6: dE distribution for the exclusive MC. The blue line represent the BW fit and the black dots the exclusive resonant MC

In Tab. 5.1 a summary of the identified signal regions is shown.

Name	Selection (in σ)	Interval (in $\mathrm{MeV/c^2}$)
dE	$[-6\sigma, +6\sigma]$	$(-20.2, 20.2)\,\mathrm{MeV/c^2}$
π^0	standard BESIII selection	$(110, 150)\,\mathrm{MeV/c^2}$
ϕ	$[-3FWHM, +3FWHM]$	$(999, 1039)\,\mathrm{GeV/c^2}$
$\mathrm{M_{bc}}$	$[-3\sigma, +3\sigma]$	$(2270, 2300)\,\mathrm{MeV/c^2}$

Table 5.1: Summary table of the identified signal regions.

5.3 Exclusive MC studies

To study the expected mass resolution for the reconstructed signal a pentaquark state, decaying in $p\phi$, is generated as a dummy particle with $2.1\,\mathrm{GeV/c^2}$ mass and zero width using BesEvtGen generator. With this simulation it is possible to check if the applied cuts introduce a bias to the reconstruction. Fig. 5.7 shows the plot of the $p\phi$ invariant mass. The fit is a BW function; the results are: mass $m_{P_s^+} = (2099.58 \pm 0.05)\,\mathrm{MeV/c^2}$, width $\Gamma_{P_s^+} = (1.81 \pm 0.05)\,\mathrm{MeV}$. The mass is compatible with the generated one, thus no bias is introduced by the selections. The width is the expected mass resolution for the BESIII detector.

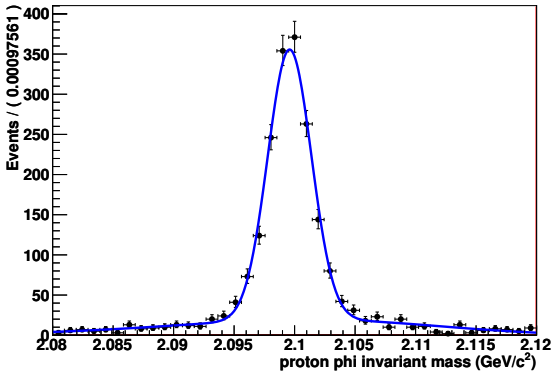

Figure 5.7: Invariant mass distribution of the P_s^+. The blue line shows the fit to the exclusive MC dummy generated particle, with a mass of 2.1 GeV/c^2

The finite resolution of the detector can affect the invariant mass distribution of the final state. In order to eventually correct for this effect, it is necessary to divide the final number of events in the mass distribution by the efficiency for each mass bin. To extract this information, the non resonant MC is used. Fig 5.8 shows the efficiency versus the $p\phi$ invariant mass. The plot ranges from 1.95 GeV/c^2 to 2.15 GeV/c^2, that are kinematic limits for the production of this particular final state in Λ_c decays. The efficiency increases with the $p\phi$, and has a drop at exactly 2.151 GeV/c^2 that is the maximum mass allowed for the pair to be produced along with π^0. The higher bin around 2.15 GeV/c^2 is caused by the limited number of events. This effect will be taken in account during the systematics discussion.

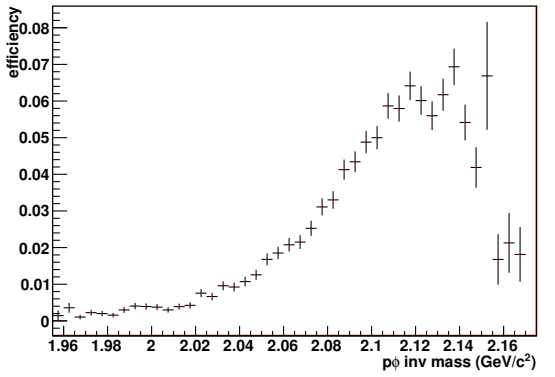

Figure 5.8: Efficiency as a function of the invariant mass of the $p\phi$ candidate in the non resonant exclusive process.

5.4 Background evaluation

The BESIII Charm analysis group has generated large inclusive MC samples for all the analyses. Since this is a search for a new possible state, the inclusive MC does not contain any signal, either the resonant or the non-resonant. The study of the inclusive MC sample aims to understand the level of background that will remain after the cuts, its shape, and to observe any peaking background.

5.4.1 Background studies with inclusive MC sample

In this part all the previously discussed distributions will be studied, using the inclusive MC samples provided by the charm group. For all the plots the interested signal region will be shown with all the aforementioned cuts already applied, except for the one being studied. Since for all the other background sources (*i.e.* $D\bar{D}$, ISR and $\tau^+\tau^-$) the final number of events is negligible, only $\Lambda_c\bar{\Lambda}_c$ and $q\bar{q}$ will be shown as the a red and blue stacked histograms respectively. The differences between the stacked histograms and the black dots represents the contributions of the other background sources.

Fig. 5.9 shows the π^0 invariant mass distribution: no structure compatible with a resonant π^0 mass is present. In Fig. 5.10 the ϕ invariant mass is shown. In Fig. 5.11 the M_{bc} distribution is reported. Also here no peaking Λ_c events survive the selections compatible with the fact that in inclusive MC there is no signal. Fig. 5.12 shows the $p\phi$ mass distribution. The level of background is limited, even though only one kaon from the ϕ is positevely identified through the PID.

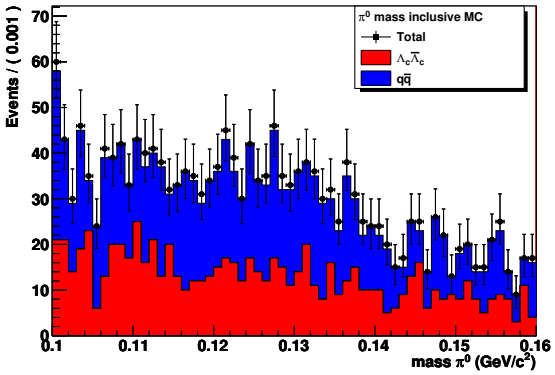

Figure 5.9: Inclusive MC studies. Invariant mass of π^0. The black dots represents the inclusive samples. Red histograms represents the Λ_c pair sample, while the blue one the contribution from the $q\bar{q}$

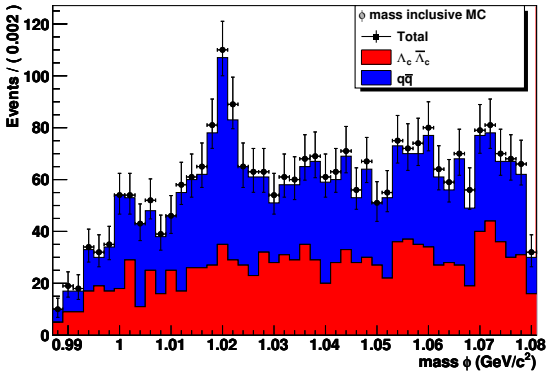

Figure 5.10: Inclusive MC studies. Invariant mass of ϕ. The black dots represents the inclusive samples. Red histograms represents the Λ_c pair sample, while the blue one the contribution from the $q\bar{q}$

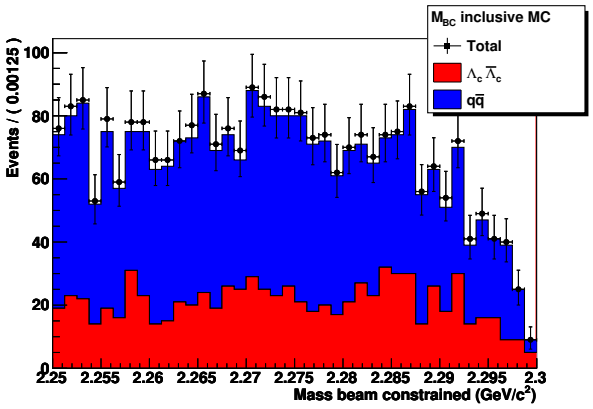

Figure 5.11: Inclusive MC studies. Distribution of M_{bc}. The black dots represents the inclusive samples. Red histograms represents the Λ_c pair sample, while the blue one the contribution from the $q\bar{q}$

5.5 Extraction of the signal events

The main goal of this work is to search for a pentaquark in the $p\phi$ invariant mass. Before coming to the real data it is necessary to discuss how to extract the signal events from the M_{bc} and ϕp spectra. A 2D-fit will be performed to extract the number of events, due to non-trivial shape of the distributions. The number of events found in the 2D-fit will be used for the further discussions.

For the M_{bc}, the function chosen is the sum of an Argus function for the background plus the MC signal shape extracted from the signal MC discussed in Sec. 5.2.2. The choice of the Argus function for the background comes naturally from to the definition

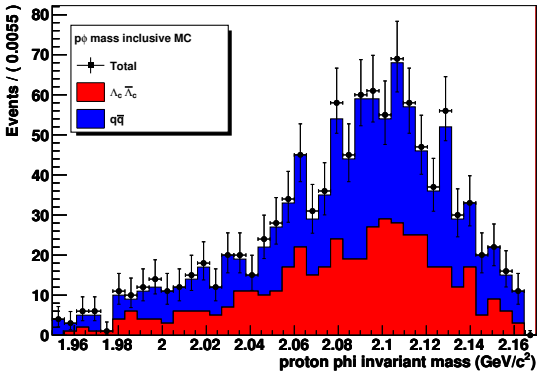

Figure 5.12: Inclusive MC studies. Invariant mass of $p\phi$ candidates. The black dots represents the inclusive samples. Red histograms represents the Λ_c pair sample, while the blue one the contribution from the $q\bar{q}$

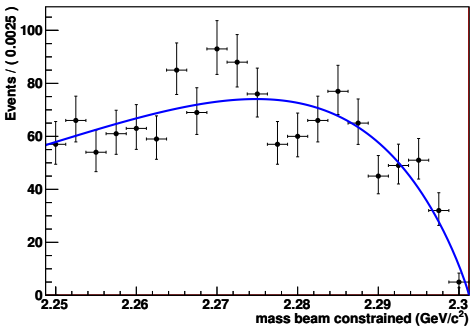

Figure 5.13: Fit to the inclusive MC shape of the M_{bc} variable. The blue line represents the Argus fit.

of the M_{bc} variable. In Fig. 5.13 the resulting fit is shown.

For what concerns the $p\phi$ invariant mass, the distribution shape is not trivial. In order to find the best function to perform the fit, the inclusive MC is tested with different functions, since the MC distributions of the ϕ, π^0, M_{BC} and $p\phi$ invariant mass fit well the corresponding real data. The best fit is determined to be again the Argus function and the plot is shown in Fig. 5.14.

The limited available phase space, that closes abruptly at $2.15\,\mathrm{GeV/c^2}$ due to associated π^0 production, seems to point in the direction of using an Argus function, associated to the reconstruction of a decaying particle in a continuum background.

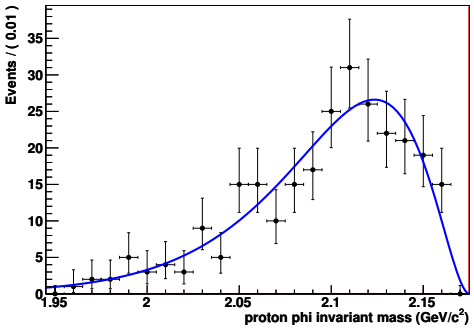

Figure 5.14: Fit to the inclusive MC shape of the $p\phi$ invariant mass. The blue line represents the Argus fit.

5.6 Results from real data samples

After the optimization of the cuts and the study of the level of the possible background, it is now possible to look at the data.

The following plots represent the distributions of the variables shown before. Fig. 5.15, Fig. 5.16, Fig. 5.17 and 5.18 show the π^0, ϕ , M_{bc}, $p\phi$ pair invariant mass respectively. The inclusive MC and the real data agree very well apart from three bins around $2.03\,\mathrm{GeV}/c^2$ in Fig. 5.18.

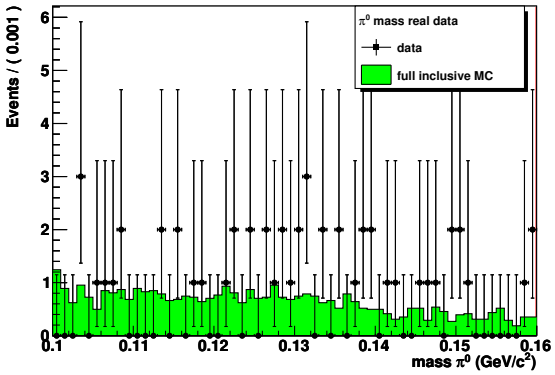

Figure 5.15: Real data studies. Invariant mass of π^0. All the available statistics is presented. The black dots represents the data. Green histograms represents the inclusive MC sample rescaled by the luminosity of the real data sample.

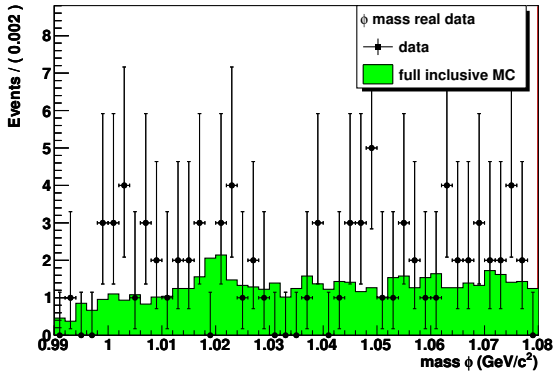

Figure 5.16: Real data studies. Invariant mass of ϕ. All the available statistics is presented. The black dots represents the data. Green histograms represents the inclusive MC sample rescaled by the luminosity of the real data sample.

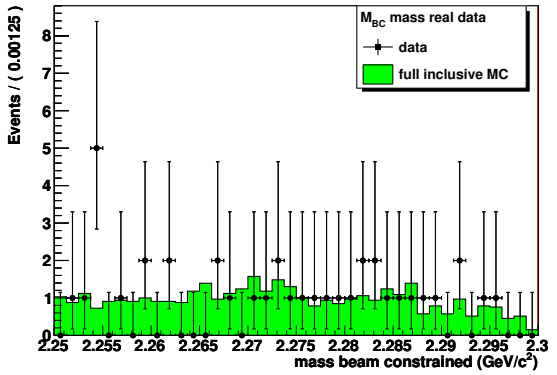

Figure 5.17: Real data studies. Distribution of M_{bc}. The black dots represents the data. Green histograms represents the inclusive MC sample rescaled by the luminosity of the real data sample.

5.6.1 $\Lambda_c^+ \to p\phi\pi^0$

It is possible to fit the M_{bc} invariant mass directly to extract the number of events of the non-resonant process $\Lambda_c^+ \to p\phi\pi^0$. The function discussed in the previous section is used to parametrize the background. The result of the fit is shown in Fig. 5.19.

The significance is extracted using the formula:

$$\sqrt{2 * (NLL_{null} - NLL_{signal})} \tag{5.3}$$

.

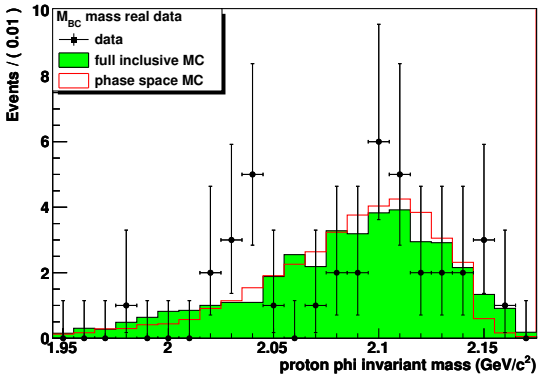

Figure 5.18: Real data studies. Invariant mass of $p\phi$. The black dots represents the data. Green histograms represents the inclusive MC sample rescaled by the luminosity real data sample. The red line represents the $\Lambda_c \to p\phi\pi^0$phase space sample.

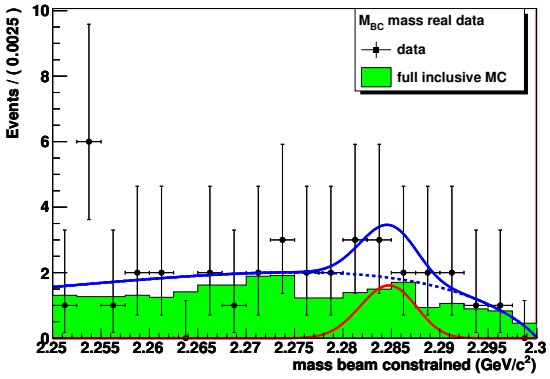

Figure 5.19: Real data studies. Invariant mass of M_{bc}.

where NLL_{null} represents the value of the negative log-likelihood of the hypothesys of only background and NLL_{signal} represents the value of the negative log-likelihook of the test hypothesys where there is signal of Λ_c baryon. Since the resulting significance is below 3σ, it is possible to extract the upper limit by using the formula:

$$UL = \frac{\mathrm{N}^{\mathrm{NR}}_{\mathrm{expected}}}{2N_{\Lambda_c}\varepsilon^{NR}\mathcal{B}(\phi \to K^+K^-)} \tag{5.4}$$

where $N^{NR}_{expected}$ is the number of the expected events from a profile likelihood calculation for at 90% confidence level (C.L.). Being $\varepsilon^{NR} = 1.01\%$ the efficiency calculated with exclusive non-resonant MC, N_{Λ_c} is taken from Ref. [89], the resulting upper limit is $U.L.(\mathcal{B}(\Lambda_c \to p\phi\pi^0) < 8.6 \cdot 10^{-3}$ at 90% C.L. considering also the systematics that will

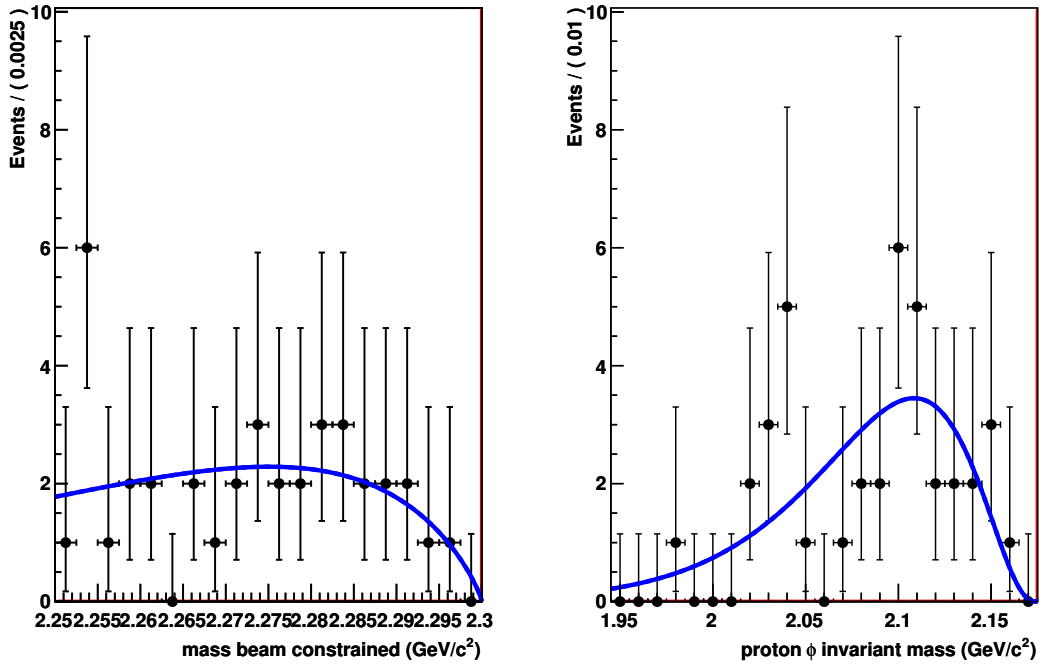

Figure 5.20: Projection of the 2D fit on M_{bc} (left) and $p\phi$ (right) distribution. The blue line shows the fit.

be discussed in Sec. 5.8.

5.6.2 $\Lambda_c^+ \to P_s^+ \pi^0$

The fitting functions discussed in the previous sections are used to parametrize the total fitting function for a 2D fit to extract the events in the $p\phi$ invariant mass. The parameters found are then fed to the fitting routine to extract the number of events. The results of such fit are shown in Fig. 5.20. However, three bins around $2.03\,\mathrm{GeV/c^2}$ may point slightly higher than the data.

Thus, a fit model with the Argus PDF plus a convolution of a Gaussian and a BW is applied to the data. The gaussian width is fixed to the measured resolution. The result is shown in Fig. 5.21. The mean and the width are:

- $M_{p\phi} = (2036 \pm 3)\,\mathrm{MeV}/c^2$
- $\sigma_{p\phi} = (4 \pm 3)\,\mathrm{MeV}/c^2$.

The use of the Gaussian function instead of the BW one is justified by the very low

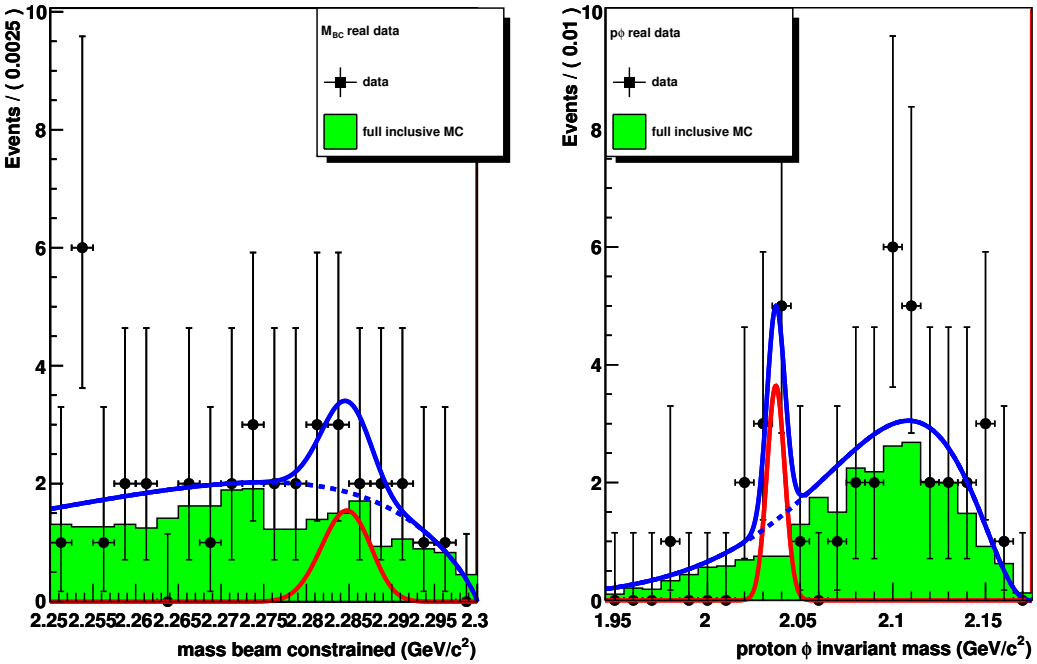

Figure 5.21: Projection of the 2D fit on M_{bc} (left) and $p\phi$ (right) distribution. The blue line shows the total fit. The red line represent the gaussian signal. The number of signal and backgrounds events is constrained to be the same in the two projections of the 2D fit. In this plot the green histograms represent the inclusive MC contribution.

statistics.

5.6.3 Study of the significance of the pϕ structure around 2.03 GeV/c^2

In order to estimate the significance of the small enhancement around 2.03 GeV/c^2, a negative log likelihood (NLL) function is created. The resulting value of NLL with the null hypothesis, *i.e.* the distribution is all Argus, is taken against the resulting value of the NLL with the signal hypothesis. The significance is then extracted usign the following formula in Eq. 5.6.1

The results of the two hypotheses are the following: $NLL_{null} = -166.157$, while the $NLL_{signal} = -171.568$, resulting in a total 2.57σ significance.

Toy MC consistency studies

Another possible way to estimate the significance of the bump around 2.03 GeV/c^2 is using a Toy MC. In this way it is possible to estimate how many times the background fluctuation can reproduce the number of signal events found. The procedure is the following:

- Extract the parameter of the background from the fitting function;
- run 10000 experiments in which 20 events are extracted from the fitting function just defined during the 2D fit;
- define the signal region to be one sigma around the central fit values;
- fit the 20 events of each experiment with the total fitting function (signal plus background);
- count in how many experiments the fitting function provides mean and width in the signal region defined with at least the same number of events that we have found in the analysis.

Of all the 10000 experiments, 107 pass the last selection point. Again, as it was found for the likelihood variation, the significance is below 3σ (that would have been 30 experiments, while 2σ would have been 500 experiments).

5.7 Discussion of the results

Since the statistical significance observed for the $\Lambda_c \to P_s\pi^0$ $P_s \to p\phi$ is below 3σ, the upper limit is calculated at 90% C.L., using the formula:

$$UL = \frac{\mathrm{N_{expected}}}{2N_{\Lambda_c}\varepsilon\mathcal{B}(\phi \to K^+K^-)} \tag{5.5}$$

where N_{Λ_c} is taken from Ref. [89], $\mathrm{N_{expected}}$ is calculated using the Profile Likelihood Method and the ε is the efficiency of each single final state calculated with exclusive MC simulation.

The resulting U.L. is $U.L.(\mathcal{B}(\Lambda_c \to P_s\pi^0) \times \mathcal{B}(P_s \to p\phi)) < 6.3 \cdot 10^{-3}$ at 90% C.L. considering also the systematics in Sec. 5.8. This result is compatible with the BELLE results even if it sets a less stringent limit.

5.8 Systematic uncertainties

The main sources can be divided in tracking, branching fractions, MC limited sample and signal parametrization.

- **Charged and neutral tracks** For each π^0 reconstructed, it is safe to quote 2% uncertainty, and 1% for each charged track as in Ref. [112].
- **dE signal region** The signal region is modified by $\pm 1\sigma$. The relative variation on the number of events is taken as systematic contribution.
- **Intermediate branching fractions** The error quoted from the PDG [24] on the BR of $\phi \to K^+K^-$ and $\pi^0 \to \gamma\gamma$ are taken as the systematic error for the upper limits determination.
- **MC generation** The number of events generated to estimate the efficiency for both the resonant and the non resonant process gives a systematic contribution that can be estimated as $\sqrt{1-\varepsilon) \cdot \varepsilon / N}$, where ε is the efficiency and N is the number of generated events.
- **Number of Λ_c** In the process of extracting the upper limit the number of Λ_c extracted from Ref. [89] is used. The error on the number determination is taken as systematic contribution.
- **ϕ selection** The ϕ signal region is modified by $\pm 1\sigma$. The maximum relative variation on the number of the events is taken as systematic contribution.
- **$\mathrm{M_{bc}}$ mass window** The signal region is shrunk by $10\,\mathrm{MeV}/c^2$ in the lower region. The relative variation on the number of events is taken as systematic contribution on the upper limit calculations.
- **$p\phi$ signal function** One more parameter at the time is fixed and the other one is left floating. The relative variation of the number of events is taken as systematic contribution.

One sources of systematic uncertainties is determined directly from the data, since it is related to the effect of the remaining low statistics.

- **$p\phi$ binning** Statistical fluctuations are very important when only few events survives. To address the uncertainty related to the choice of the binning size, two hypotheses with a smaller and a wider steps are taken. The ratio between the relative difference of the number of events found and the nominal results is taken as systematic uncertainty.

Tab. 5.2 provides a schematic summary of the investigated sources. Since all the single contributions can be considered uncorrelated, the total systematic contribution can be estimated by $\sqrt{(\Sigma_i^n \sigma_i)}$. The final number is 28.9%, mostly due to the shape of the $p\phi$ invariant mass.

Source	$\mathbf{\Lambda_c^+ \to p\phi\pi^0}$	$\mathbf{\Lambda_c^+ \to P_s^+\pi^0}$
Tracking Charged tracks	1% per track	1% per track
Pion selection	2% for pion	2% for pion
MC generation	negligible	negligible
Intermediate BR $\phi \to K^+K^-$	0.5%	0.5%
Intermediate BR $\pi^0 \to \gamma\gamma$	negligible	negligible
ϕ selection	10%	10%
M_{bc} mass window	3.5%	3.5%
$p\phi$ signal function	-	24.7%
$p\phi$ binning	-	10%
TOTAL	10.9%	28.9%

Table 5.2: List of the calculated systematics uncertainties.

Chapter 6

Final Remarks and Outlook

QCD is the best tool to try to unlock the misteries of the strong interaction. However, up to now, the proper way to describe the composition of the hadron masses directly from the lagrangian is still missing. While the Lattice QCD becomes more precise year by year, effective field theories are the only pratical tool to understand the QCD. The Quark Model is the simplest effective model to interpret the hadron spectrum: however this unsophisticated model cannot cope with a much more complicated picture.

The search for multiquarks states remains one of the most active fields in high energy physics. The study of the states compatible with exotic structures is growing with the results from different collaborations. The discovery of a single state is a great results per se, but only by keeping in mind the larger scheme it is possible to address the real goal of these searches: to provide indication for a better understanding of the strong interaction at its maximum strength.

The discrepancy between the conventional charmonium model and the experimental spectrum represents one of the most incontrovertable evidences. As experimentalist, our duty is to provide more and more precise observations of new states and transitions among the conventional hadrons and the exotic ones, and among the exotics themselves, to pin down their nature. The observation or the missing evidence of a particular state or transition can help in discriminating among the different models. BESIII plays a major role in the search for exotics in the charmonium spectrum, thanks to the possibility to directly access the 1^{--} states and using a clean enviroment to study the transitions.

The search for flavour partners of the existing structures is a good way to improve our understanding level of the underlying dynamics. The search for hidden-strangeness pentaquark is a good example and was investigated in this work. The possibility to produce Λ_c baryon pairs just above thresholds allows to keep high statistics with the single tag analysis, and to provide a clean, background-free environment if both sides are reconstructed are the main advantages of BESIII experiment.

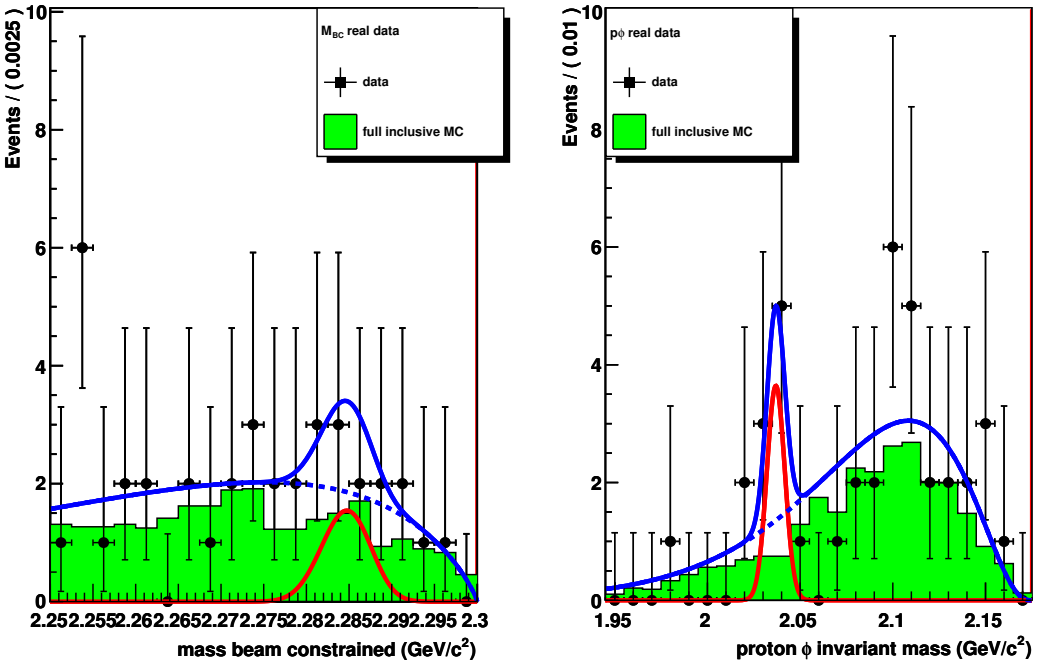

Figure 6.1: 2D fit to the M_{bc} and $p\phi$ invariant masses.

This work profits of the $567\,\mathrm{pb}^{-1}$ collected by BESIII in 2014 at 4.6 GeV. After removing the charged Σ baryon region, the data are analysed to search for the process $\Lambda_c \to P_s\pi^0$, $P_s \to p\phi$.

The first result is the upper limit for the process $\Lambda_c^+ \to p\phi\pi^0$. The resulting upper limit, once the proper systematics are considered, is $UL(\mathcal{B}(\Lambda_c \to p\phi\pi^0)) < 8.6 \cdot 10^{-3}$, compatible with the BELLE results, even if less stringent.

From the 2D fit to the mass beam constrained and the $p\phi$ invariant masses it is possible to see that a bump arises in $p\phi$ invariant mass around $2.03\,\mathrm{GeV}/c^2$ with significance less than 3σ. The resulting parameters are:

- $M_{P_s} = (2036 \pm 3)\,\mathrm{MeV}/c^2$
- $\sigma_{P_s} = (4 \pm 3)\,\mathrm{MeV}/c^2$.

and the fit results is shown in Fig. 6.1.

The upper limit found, considering the systematics, is $UL(\mathcal{B}(\Lambda_c \to P_s\pi^0) \times \mathcal{B}(P_s \to p\phi)) < 6.3 \cdot 10^{-3}$.

The BELLE collaboration published the result discussed in Sec. 2.3.2. Their upper limit is much more stringent than the results presented in this work thanks to a much

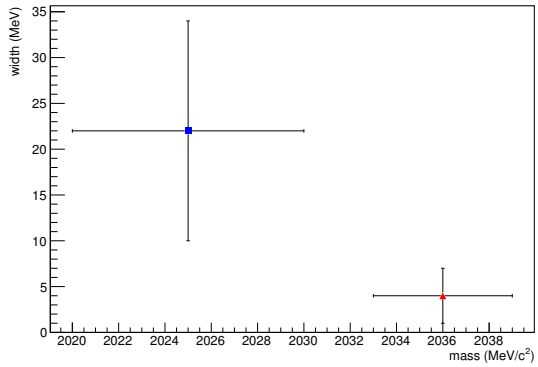

Figure 6.2: Mass and width of the P_s published results by BELLE (blue) and this work (red).

larger statistics. A comparison between the two enhancements properties is shown in Fig. 6.2.

The most important conclusion that we can draw is that the possibility to search for hidden-strangeness pentaquark in $p\phi$ invariant mass is real. In a near future, BESIII will collect $3\,\mathrm{fb}^{-1}$ at the Λ_c pairs threshold. This new dataset will help to shed new light to the hidden-strangeness pentaquark: an evidence or the discovery of another pentaquark candidate after the LHCb ones will be very helpful to continue to explore the features of the strong interaction.

Appendix A

Theoretical model

The following sections will present a brief review on the effective field theory used to describe the exotic XYZ state and their applications to the pentaquark. The aim is to provide a background from the theoretical point of view in order to understand the peculiarities of each model. For more detailed reviews, it is possible to read Ref. [113] and Ref. [114]. The last section will be dedicated to models that provide indication on the searches for hidden-strangeness partners of the P_c LHCb pentaquarks, and shall be considered the theoretical foundation of this work.

A.1 Models to explain exotics

A.1.1 Molecular state

The picture in which two mesons loosely bound to form a molecule resembles the well-know picture of the atomic physics, where two atoms bound together to form molecules. The paradigm is easy and straightforward to be followed: two color neutral mesons exchange a pion to form a molecule. This model has another advantage: using the color algebra, it is possible to form 2-quark 2-antiquark systems only in two possible independent ways, *e.g.* if we consider $c\bar{c}q'\bar{q}$ combination, they are $(c\bar{c})(q'\bar{q})$ or $(c\bar{q})(q'\bar{c})$. This means that the possible structures are indeed either the combination of a charmonium plus a light meson or the combination of two open charm mesons. This model is also usually used also to describe pentaquark states, where one of the mesons is substitute by a baryon. This will be discussed later.

As mentioned before in Sec. 2.1.1, the $X(3872)$ was the first state to be modeled to a molecular state due to the vicinity of the $D\bar{D}^*$ threshold. This, if it is the case, means that the $X(3872)$ state is very loosely bound, at least 10 times more weakly than the deuteron. The absence of isospin partners of the $X(3872)$ suggests that the meson exchange picture can hold, since, as for the $I = 0$ deuteron, the expected meson to be

exchanged is the $I = 1$ pion. In addition, to strengthen the π meson exchange model it is possible to notice the absence of dominant structures close to the $D^0\bar{D}^0$ threshold, which are not expected since the $D^0\bar{D}^0\pi$ couplings are forbidden by the strong interaction invariance under rotation plus parity.

A feature typical of the molecular state is the broadness of the radius. This become manifest studying the bound state wave function, that a large distance scales as $\exp(-\gamma r)/r$, where r is the distance between the constituent and γ is the typical momentum scale. γ depends on the binding energy $E_B = m_1 + m_2 - M$ and the reduced mass of the hadron pair $\mu = m_1 m_2/(m_1 + m_2)$, and it is usually defined as

$$\gamma = \sqrt{2\mu E_B}$$

The typical radius of the state is defined as $\sim 1/\gamma$. If $X(3872)$ is a molecule, its radius is the order of 10 fm (ten times larger than the typical proton size).

The extension to the other XYZ state is not particular fruitful. The $Z_c^+(3900)$ lies 20 MeV above the closest threshold and from the most recent measurements [49] have a large branching fraction in the $D\bar{D}^*$: this behaviour seems to go in the opposite direction with respect to the molecular hypothesis, since it is very unlikely that a bound state is formed out of components in which it can freely decay. Moreover, measurements of prompt production of $X(3872)$ in high energy collisions [29] seems to disfavour this model as unambiguous assignment even for the $X(3872)$.

A.1.2 Hadroquarkonium

Hadroquarkonium (or hadrocharmonium if the constituents are charmonia) models were originally proposed to explain why some exotic preferred to decay into pion pairs plus a charmonia rather than into open charm pairs, like the $Y(4260)$. The scheme is simple: a heavy quark pair forms a core around which the light quarks form a quantum-mechanical cloud [115],[116]. Two possible interpretations of this core-cloud combination appear in literature. In the first case, both the cloud and the core are in color-singlet configuration: in this way, the binding is provided by weak color van der Waals forces, as mentioned for the molecular state. In the second case, the cloud and the color live in the color-adjoint representation: in this latter case, the color binding is much stronger.

The hadroquarkonium is supported by the heavy-quark spin symmetry [117], a model in which the heavy quark degrees of freedom decouple to the light ones. Thus, the $c\bar{c}$ in the core should influence the final state spin and wave. This is used to justify the $Z_c(4430)$ [19], a heavier partner of the $Z_c(3900)$, that decay preferentially to $\psi(2S)$ rather than to J/ψ.

On the other hand, there are some conceptual difficulties that leave some questions unanswered: if the binding force is weak as described, it is not clear how long the bond

will persist; conversely, if it is sufficiently strong, it is not clear why the components should stay decoupled and not rearrange in open charm mesons.

A.1.3 Diquark models

Apart from the conventional $q\bar{q}'$ triplet-antitriplet combination, other more complex structures have attractive behaviour. The diquark model profits of the color SU(3) combination $\mathbf{3} \otimes \mathbf{3} = \bar{\mathbf{3}} \oplus \mathbf{6}$. The $\bar{\mathbf{3}}$ component is attractive, with a strength that is just half as strong as between a quark and an antiquark as it can be shown starting from Fig. A.1.

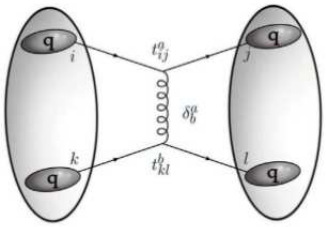

Figure A.1: Diquarks to form a tetraquark schematic example. In the model, the tetraquark is bound due to single gluon exchange.

In Fig. A.1 the leading diagram of single gluon exchange between two diquarks is presented. The product of the two vertices can be decomposed as

$$t^a_{ij} t^a_{kl} = -\frac{2}{3}(\delta_{ij}\delta kl - \delta_{il}\delta kj)/2 + \frac{1}{3}(\delta_{ij}\delta_{kl} + \delta_{il}\delta_{kj})/2$$

The first term represents the antisymmetric $\bar{\mathbf{3}}$ combination. The minus sign indicates an attractive strength and the coefficient the magnitude of the attraction. Similar calculation for conventional $q\bar{q}$ pairs give a factor $-4/3$. On the other hand, the symmetric $\mathbf{6}$ components is repulsive and cannot create bound states.

The diquark model was originally studied for baryons and for the light-quark scalar meson $a_0(980)$ and $f_0(980)$, but seems to work also for the exotics, especially for the $Z_c(3900)$, and for the $Z(4430)$ as its first radial excitation. In 2004 Maiani et al. [118] proposed a model to interpret the $X(3872)$ with the diquark picture and even the evidence that the transition $Y(4260) \to \gamma X(3872)$ [42] would be an allowed electric dipole transition [119].

This model has a very strong predictive power, and, even though many observed exotic states can be accommodated in the diquark pictures, many other predicted states are not observed.

A.1.4 Hybrids

One intriguing explanation for the exotics state observed rely on a configuration that was predicted at the beginning of the quark model: the hybrid, in which the at conventional $q\bar{q}$ degrees of freedom is added the gluonic one. The configuration $q\bar{q}g$ gives origin at a color singlet hadron, as shown in the following equation, following the color algebra $SU(3)_c$:

$$\mathbf{3} \otimes \bar{\mathbf{3}} \otimes \mathbf{8} = (\mathbf{1} \oplus \mathbf{8}) \otimes \mathbf{8} = \mathbf{27} \oplus \bar{\mathbf{10}} \oplus \mathbf{10} \oplus \mathbf{8} \oplus \mathbf{8} \oplus \mathbf{8} \oplus \mathbf{1}$$

. This model originates from QCD-inspired flux-tubes models [120]. Extensions to the hybrid picture, in which the gluonic degree of freedom dominates the state, are called glueballs.

The easiest way to identify a state as a hybrid would be to find that the spin-parity assignment cannot be created by a $q\bar{q}$ in a given orbital angular momentum wave, since of the 8 predicted state, 3 have this feature. Unfortunately, all the states that were discovered up to now have conventional spin-parity assignment.

Lattice-QCD calculations [121] predict the lightest charmonium hybrid at masses around 4.2 GeV/c^2, but with very high pion mass $m_\pi \sim 400\,\mathrm{MeV}/c^2$. For long time, the $Y(4260)$ [122], [123], [124] has been considered a viable candidate for the hybrid assignment. However, being the nature of the hybrid as *hadronic* as the conventional meson, it is quite complicated to have a firm observation without a proper theory predicting masses, width of the states. One useful test that can be used to test the $Y(4260)$ is to test the decay into $D^*\bar{D}_0^*(2460)$, where $\bar{D}_0^*(2460)$ is a $J^{PC} = 0^{++}$ $D\pi$ resonance. However This final state is very difficult to be observed, due to the broad ($\Gamma(D_0^*(2400)) = 267 \pm 40\,\mathrm{MeV}$) S-wave component, that could be easily disguised as non-resonant background.

A.1.5 Kinematic effects

Another possibility to describe these states relies not on quarks (or gluons) effect, but indeed, on some kinematic rescattering that may happen in the final state of the interaction (Final State Interaction, FSI). This effect shall be enhanced for those states which sit just a few MeV above some open flavour threshold: $Z_c(3900)$ $[D\bar{D}^*]$, $Z_c(4020)$ $[D^*\bar{D}^*]$, $Z_b(10610)$ $[B\bar{B}^*]$ and $Z_b(10650)$ $[B^*\bar{B}^*]$.

It is possible to understand more details of this effect at threshold considering a two-channel non-relativistic example. Considering $a \to a$ and $a \to b$ (where letters indicate states) scattering, it is possible to calculate the S matrix:

$$S = \begin{pmatrix} \sqrt{1-\rho^2}e^{2i\delta_a} & i\rho e^{i(\delta_a+\delta_b)} \\ i\rho e^{i(\delta_a+\delta_b)} & \sqrt{1-\rho^2}e^{2i\delta_b} \end{pmatrix} \tag{A.1}$$

Near an s-wave threshold, where $E = E_0$ (E_0 is the energy at threshold), $\rho^2 \approx 2ck$, where c is a constant and

$$k^2 = 2\mu_b(E - E_0)$$

It is then possible to calculate the cross section

$$\sigma(a \to a) \approx \frac{4\pi}{2\mu_a E}|\frac{(1-ck)e^{2i\delta_a} - 1}{2i}| \approx \frac{4\pi}{2\mu_a E}(1-ck)sin^2\delta_a$$

Approaching E_0 from above, the cross section $\sigma(E)$ is not problematic, but $d\sigma/dE \to -\infty$, that is an evidence of slope discontinuity. By continuing and passing E_0, this discontinuity can become manifest and appear as a *cusp*. This effect was pointed out by Wigner [125] in 1948 and later in Ref. [126] and in Ref. [127]. Since this effect can be related to a self-energy threshold singularity, this is also called *threshold effect*, *rescattering effect* or *cusp effect*: they all refer to the dynamics described above. This cusp can create a phase motion that can be similar to a Breit-Wigner amplitude, so this thresholds kinematic effect can be very tricky to be distinguished from a real state in PWA analyses.

A.2 Application to P_c pentaquarks

Following the description given in the last sections, it is possible to describe similar models for the P_c pentaquark observed at LHCb. If the Argand diagram of the $P_c(4450)$ shows a phase motion typical of a resonance, the $P_c(4380)$ requires more data. However, since the pentaquarks lie above different thresholds, there is no unambiguous description for both states. The $\Sigma_c^{*+}\bar{D}^0$ final state has the threshold of $(4382.3 \pm 2.4)\,\mathrm{MeV}/c^2$, close to the mass of $P_c(4380)$. The $P_c(4450)$ mass is just a few MeV/c^2 away from several thresholds:

- $\chi_{c1}p$, at $(4448.93 \pm 0.07)\,\mathrm{MeV}/c^2$
- $\Lambda_c^{*+}\bar{D}^0$, at (4457.09 ± 0.35)
- $\Sigma_c^{+}\bar{D}^{*0}$, at $(4459.9 \pm 0.9)\,\mathrm{MeV}/c^2$
- $\Sigma_c^{+}\bar{D}^{0}\pi^0$, at $4452.7 \pm 0.5)\,\mathrm{MeV}/c^2$.

Therefore, there are several models to explain these two states: baryoncharmonia ([128]); rescattering effect ([129] [130]); open charm-baryon and charm-meson bound states ([131], [132]); compact diquark-diquark-antiquark states [133].

A.2.1 Rescattering interpretation

As explained above, the presence of a threshold can produce peaking effects in the cross section. For the $P_c(4450)$ there are two possible effects: 2-point loop with 3-body production $\Lambda_b^0 \to K^- \chi_{c1} p$ followed by the rescattering $\chi_{c1} p \to p J/\psi$; triangular singularities in which the $K^- p$ are produced by the decay of a Λ^* and then the proton rescatters against the χ_{c1} to produce the final state of interest. The two models are depicted in Fig. A.2a and Fig. A.2b respectively.

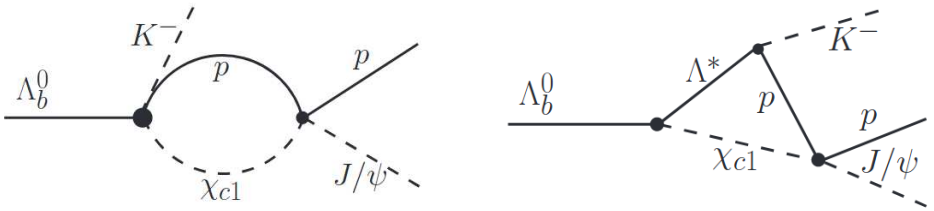

(a) Two point loop production of $Kchi_{c1}p$ decay and subsequently $p\chi_{c1} \to pJ/\psi$ rescattering.

(b) Triangular singularities to produce the $K^- pJ/\psi$ final state.

Figure A.2: Possible contributions for the rescattering process.

The triangle singularities requires P- and D-wave for the $\chi_{c1}p$ to describe the assigned quantum number, $3/2^-$ or $5/2^+$ respectively. However, the $\chi_{c1}p$ is at threshold, so the strength of this contribution seems not be able to account for the narrow peak.

The first contribution instead can be calculated in terms of a Green function

$$G_\Lambda = \int \frac{d^3q}{(2\pi)^3} \frac{\overrightarrow{q}^2 f_\Lambda(\overrightarrow{q}^2)}{E - m_p - m_{\chi_{c1}} - \overrightarrow{q}^2/(2\mu)}$$

,

that can be solved analytically [**?**] giving:

$$G_\Lambda(E) = \frac{\mu\Lambda}{(2\pi)^{3/2}}(k^2 + \Lambda^2/4) + \frac{\mu k^3}{2\pi} e^{-2k^2/\Lambda^2} \left[\mathrm{erfc}\left(\frac{\sqrt{2}k}{\Lambda}\right) - i \right]$$

The resulting phase motion is shown in Fig. A.3 compared to the Breit-Wigner amplitude, and has to compared to Fig. 2.17. This behaviour phase motion behaviour is due to the error function (erfc). The Breit-Wigner amplitude is preferred, but more data and final states are needed to understand the difference.

A.2.2 Molecular baryon-meson interpretation

Following the molecular interpretation of the $X(3872)$ it is possible to construct a similar composite molecule for the P_cs: the $P_c(4380)^+$ is identified with $\Sigma_c(2455)\bar{D}^*$ and the

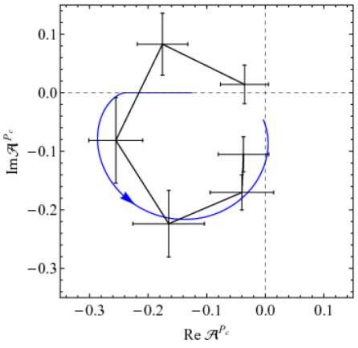

Figure A.3: Comparison between the cusp model (in blue) and Breit-Wigner (as black dots) phase motion of Ref. [129] and Ref. [1] respectively.

$P_c(4450)^+$ with $\Sigma_c(2520)\bar{D}^*$. These states remain bound due to the meson exchange mechanism.

It is possible to build effective Lagrangians [134] and therefore predict the spin and isospin assignment of the states. In this model $P_c(4380)$ is a ($J = 3/2$, $I = 1/2$) molecule, and $P_c(4450)^+$ is a ($J = 5/2$, $I = 1/2$) one. Moreover, this model predicts two additional hidden-charm pentaquarks that are the isospin partners of the known states. These additional pentaquarks shall appears in the $\Delta(1232)J/\psi$ and $\Delta(1232)\eta_c$ final states. In addition to the hidden-charm pentaquarks, this model predicts a rich ensemble of new states with hidden-bottom, B_c-like nature with well defined isospin and spin. The presence of such large number of states makes this theory highly testable: in order to assess whether this model describes the real nature of the pentaquark it will be necessary to search these other states.

A.2.3 Compact diquark-diquark-antiquark states

As mentioned earlier, the diquark combination appears as a $\bar{3}$ color anti-triplet. To yield a color singlet that has five quarks is thus necessary to combine two diquark plus an antiquark.

In order to reproduce the mass difference, in Ref. [133], the two LHCb pentaquark are identified with the following quantum numbers: $P_c(4450) = \{\bar{c}[cu]_{s=1}[ud]_{s=0};\ L_{P_c} = 1,\ J^P = \frac{5}{2}^+\}$ and $P_c(4380) = \{\bar{c}[cu]_{s=0}[ud]_{s=1}; L_{P_c} = 0,\ J^P = \frac{3}{2}^-$. In the paper a critical assumption is made, that the two contribution shown in Fig. A.4a and Fig. A.4b shall be considered to have the same probability. The contribution in Fig. A.4a follows a more traditional view for the baryons weak decay, in which the $[ud]$ diquark of the Λ_b^0 goes directly in the pentaquark: thus the spin 0 $[ud]$ diquark is kept in the pentaquark. On the other hand, in the second contribution, depicted in Fig. A.4b, the $[ud]$ diquark is shared among the pentaquark and a meson. In this case, the $[ud]$ diquark it can be

generated with either spin 0 or 1.

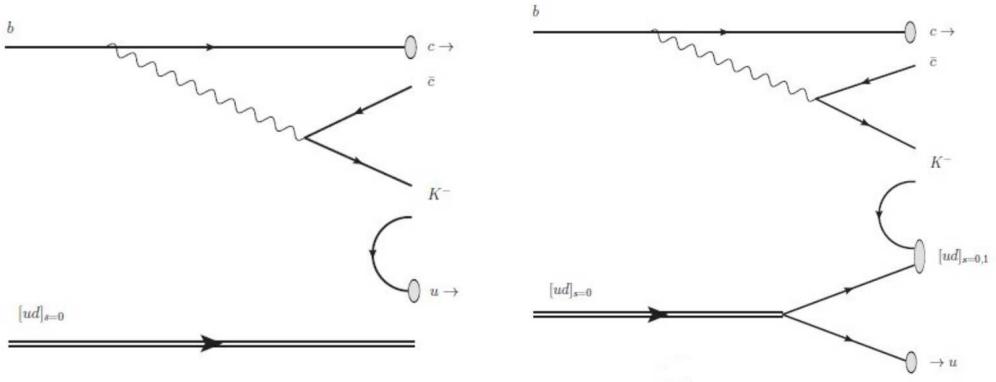

(a) Production mechanism in which the diquark $[ud]$ is directly transferred to the pentaquark

(b) Production mechanism in which the diquark $[ud]$ is shared among the final state pentaquark and meson.

Figure A.4: Two contributing mechanism in the diquark model from Ref. [133].

Starting from this single expression, it is possible to build a more complex Hamiltonian that give raise to different new states. As mentioned before for the molecule interpretation, the existence of a predictive theory helps in understanding and create connections.

Final comments on the theoretical review

The previous sections detailed what was clear also from the experimental point of view: QCD is a complex theory, transitions and states cannot be easily grouped into one single model, but each has its own feature. As the non-existence of exotic multiquark, and especially pentaquark, was compelling in 2006, as it crystal clear that we are now in verge of a new spectroscopy. The urgency of find new connection between known states, or find new states, it is not a merely collection of badges; instead it is the foundation of a more dignified goal: to shed a new light on the complexity of the quark-quark and quark-gluon interaction and provide a better understanding of fundamental piece of the matter.

Bibliography

[1] R. Aaij et al. (LHCb Collaboration), *Observation of $J/\psi p$ Resonances Consistent with Pentaquark States in $\Lambda_b^0 \to J/\psi K^- p$ decays*, Phys. Rev. Lett. **115** (2015) 072001

[2] R.F. Lebed, *Do the P_c^+ Pentaquarks Have Strange Siblings*, Phys. Rev. **D92** 114030 (2015)

[3] J.J. Xie and F.K. Guo, *Triangular singularity and a possible ϕp resonance in $\Lambda_c^+ \to \pi^0 \phi p$ decay*, ArXiv:1709.01416.

[4] M. Gell-Mann, *A schematic model of baryons and mesons*, Phys. Lett. **8** (1964) 214.

[5] G. Zweig, *An SU_3 model for the strong interaction symmetry and its breaking*, CERN-TH-401, 1964.

[6] M.Y. Han and Y. Nambu, *Three Triplet Model with Double SU(3) Symmetry*, Phys. Rev. **139** (1965) B1006

[7] S.L. Glashow, J. Iliopoulos, L. Maiani, *Weak Interaction with Lepton-Hadron Symmetry*, Phys. Rev. D **2** (1970) 1285-1292

[8] S. Godfrey and N. Isgur, *Mesons in a Relativized Quark Model with Chromodynamics*, Phys. Rev **D32** (1985) 189

[9] D.S. Hwang and D.W. Kim, *Mass of $D_{sJ}^*(2317)$ and coupled channel effect*, Phys. Lett. **B 601** (3-4):137-143

[10] N. Brambilla, *NRQCD and Quarkonia*, arXiv:hep-ph/0702105

[11] V. Koch, *Introduction to Chiral Symmetry*, arXiv: nucl-th/9512029

[12] M. Dine, *Goldstone Bosons and Chiral Symmetry Breaking in QCD*, web:*http* : *//scipp.ucsc.edu/ dine/ph222/goldstone$_l$ecture.pdf*

[13] Z. Fodor and C. Hoelbling, *Light Hadron Masses from Lattice QCD*, arXiv: 1203.4789

[14] H. Georgi, *Heavy Quark Effective Field Theory*, web: *http : //www.people.fas.harvard.edu/ hgeorgi/tasi.pdf*

[15] L.D. Roper, *Evidence for a P_{11} Pion-Nucleon Resonance at 556 MeV*, Phys. Rev. Lett. **12** (1964) 340

[16] S.L. Olsen, T. Skwarnicki, D. Zieminska, *Non-Standard Heavy Mesons and Baryons, an Experimental Review*, arXiv: 1708.040112v1 [hep-ph]

[17] A. Ali, J.S. Lange, S. Stone, *Exotics: Heavy Pentaquarks and Tetraquarks*, arXiv: 1706.00610

[18] T. Barnes, S. Godfrey, and E.S. Swanson, *Higher Charmonia*, Phys. Rev. **D72** (2005) 054026

[19] BELLE Collaboration (S.K. Choi et al), *Observation of a resonance-like structure in the $\pi^{\pm}\psi'$ mass distribution in exclusive $B \to K\pi^{\pm}\psi'$ decays*, Phys. Rev. Lett **100** (2008) 142001

[20] R. Aaij et al. (LHCb Collaboration), *Observation of the resonant character of the $Z(4430)^{-}$ state*, Phys. Rev. Lett. **112** (2014) 222002

[21] B. Aubert et al. (BaBar Collaboration), *Search for the $Z(4430)^{-}$ at BaBar*, Phys. Rev. D **79** (2009) 112001

[22] BELLE Collaboration (S.K. Choi et al), *Observation of a narrow charmonium-like state in exclusive $B^{\pm} \to K^{\pm}\pi^{+}\pi^{-}J/\psi$ decays*, Phys. Rev. Lett. 91 (2003) 262001

[23] BELLE Collaboration (S.K. Choi et al), *Bounds on the width, mass difference and other properties of $X(3872) \to \pi^{+}\pi^{-}J/\psi$ decays*, Phys. Rev. **D84** (2011) 052004

[24] C. Patrignani et al. (Particle Data Group), *The Review of Particle Physics (2017)* Chin. Phys. C, **40** 100001 (2016) and 2017 update.

[25] R. Aaij et al. (LHCb Collaboration), *Determination of the X(3872) meson quantum numbers*, Phys. Rev. Lett. **110** (2013) 222001

[26] R. AAij et al. (LHCb Collaboration), *Quantum numbers of the $X(3872)$ state and orbital angular momentum in its $\rho^{0}J/\psi$ decay*, Phys. Rev. **D92** (2015) 011102

[27] E.J. Eichten, K. Lane, and C. Quigg, *New states above charm threshold*, Phys. Rev. **D73** (2006) 014014 [Erratum: Phys. Rev. **D73**(2006) 079903]

[28] P. Artoisenet and E. Braaten, *Production of the $X(3872)$ at the Tevatron and the LHC*, Phys. Rev. **D81** (2010) 114018

[29] S. Chatrchyan et al. (CMS Collaboration), *Measurement of the $X(3872)$ production cross section via decays to $J/\psi\pi\pi$ in pp collision at $\sqrt{s} = 7\,\text{TeV}$*, JHEP **04** (2013) 154

[30] BELLE Collaboration (K. Abe et al.), *Evidence for* $X(3872) \to \gamma J/\psi$ *and the sub-threshold decay* $X(3872) \to \omega J/\psi$, arXiv:hep-ex/0505037

[31] P. el Amo Sanchez et al. (BaBar Collaboration), *Evidence for the decay* $X(3872) \to J/\psi\omega$, Phys. Rev. **D82** (2010) 011101

[32] V. Bhardwaj et al. (BELLE Collaboration), *Observation of* $X(3872) \to J/\psi\gamma$ *and search for* $X(3872) \to \psi'\gamma$ *in B decays*, Phys. Rev. Lett. **107** (2011) 091803

[33] B. Aubert et al (BaBar Collaboration), *Search for* $B^+ \to X(3872)K^+$, $X(3872) \to J/\psi\gamma$, *Phys. Rev.* ***D74*** *(2006) 071101*

[34] B. Aubert et al. (BaBar Collaboration), Evidence for $X(3872) \to \psi(2S)\gamma$ *in* $B^\pm \to X(3872)K^\pm$ *decays, and a study of* $B \to c\bar{c}\gamma K$, *Phys. Rev. Lett.* ***102*** *(2009) 132001*

[35] R. Aaij et al (LHCb Collaboration Evidence for the decay $X(3872) \to \psi(2S)\gamma$, Nucl. Phys. **B886** (2015) 665

[36] E.S. Swanson, *Diagnostic decays of the* $X(3872)$, Phys. Lett. **B590** (2004 209

[37] B. Aubert et al. (BaBar Collaboration), *Observation of a broad structure in the* $\pi^+\pi^- J/\psi$ *mass specrum around 4.26-GeV/*c^2, Phys. Rev. Lett **95** (2005) 142001

[38] C.Z. Yuan et al. (BELLE Collaboration), *Measurement of* $e^+e^- \to \pi^+\pi^- J/\psi$ *cross section via initial state radiation at Belle*, Phys. Rev. Lett. **99** (2007) 182004

[39] J.Z. Bai et al. (BES collaboration), *Measurements of the cross-section for* e^+e^- *to hadrons at center-of-mass-energies from 2-GeV to 5-GeV*, Phys. Rev. Lett. **88** (2002) 101802

[40] X.L. Wang et al (BELLE Collaboration), *Observation of Two Resonant Structures in* $e^+e^- \to \pi^+\pi^-\psi(2S)$ *via Initial State Radiation at Belle*, Phys. Rev. Lett **99** (2007) 142002

[41] B. Aubert et al (BaBar Collaboration), *Evidence of a braod structure at an invariant mass of 4.32- GeV/*c^2 *in the reaction* $e^+e^- \to \pi^+\pi^-\psi_{2S}$ *measured at BaBar*, Phys. Rev. Lett. **98** (2007) 212001

[42] M. Ablikim et al. (BESIII Collaboration), *Observation of* $e^+e^- \to \gamma X(3872)$ *at BESIII*, Phys. Rev. Lett. **112** (2014) 092001

[43] M. Ablikim et al. (BESIII Collaboration), *Precise measurements of the* $e^+e^- \to \pi^+\pi^- J/\psi$ *cross section at center-of-mass energies from 3.77 to 4.60 GeV*, Phys. Rev. Lett. **118** (2017) 092001

[44] J.P. Lees et al (BaBar Collaboration), *Study of the reaction* $e^+e^- \to J/\psi\pi^+\pi^-$ *via initial-state radiation at BaBar*, Phys. Rev. **D86** (2012) 051102

[45] M. Ablikim et al. (BESIII Collaboration), *Observation of a Charged Charmoniumlike Structure in* $e^+e^- \to \pi^+\pi^- J/\psi$ *at* $\sqrt{s} = 4.26\,GeV$, Phys. Rev. Lett. **110** (2013) 252001

[46] M. Ablikim et al (BESIII Collaboration), *Observation of* $Z_c(3900)^0$ *in* $e^+e^- \to \pi^0\pi^0 J/\psi$, Phys. Rev. Lett. **115** (2015) 112003

[47] M. Ablikim et al (BESIII Collaboration), *Observation of a Neutral Structure near the* $D\bar{D}^*$ *Mass Threshold in* $e^+e^- \to (D\bar{D}^*)^0\pi^0$ *at* $\sqrt{s} = 4.226$ *and* 4.257 *GeV*, Phys. Rev. Lett. **115** (2015) 222002.

[48] M. Ablikim et al (BESIII Collaboration), *Observation of a Charged* $(D\bar{D}^*)^{\pm}$ *Mass Peak in* $e^+e^- \to \pi D\bar{D}^*$ *at* $\sqrt{s} = 4.26\,\text{GeV}$, Phys. Rev. Lett. **112** (2014) 022001

[49] M. Ablikim et al. (BESIII Collaboration), *Determination of the Spin and Parity of the* $Z_c(3900)$, Phys. Rev. Lett **119** (2017) no.7, 072001

[50] D. Santel et al (BELLE Collaboration), *Measurements of the* $\Upsilon(10860)$ *and* $\Upsilon(11020)$ *resonances via* $\sigma(e^+e^- \to \Upsilon(nS)\pi^+\pi^-$, Phys. Rev. **D93** (2016) 011101

[51] A. Bondar et al (BELLE Collaboration), *Observation of two charged bottomonium-like resonances in* $\Upsilon(5S)$ *decays*, Phys. Rev. Lett. **108** (2012) 122001

[52] M. Karliner and J.L. Rosner, *New Exotic Meson and Baryon Resonances from Doubly-Heavy Hadronic Molecules*, Phys. Rev. Lett. **115** (2015) 122001

[53] T.G. Trippe et al (Particle Data Group), *Review of Particle Properties*, Rev. Mod. Phys. **48** (1975) No. 2 part II

[54] I. Montanet et al. (Particle Data Group), *Review of Particle Properties*, Phys. Rev. **D50** (1994) 1173

[55] G. Trilling, *Pentaquark Update - Part of Review of Particle Properties*, J. Phys. G **33** (2006) 1.

[56] K.A. Olive et al. (Particle Data Group), *The Review of Particle Physics*, Chin Phys. C **38** (2014) 090001

[57] R. Aaij et al. (LHCb Collaboration), *Model-indipendent evidence for* $J/\psi p$ *contributions to* $\Lambda_b^0 \to J/\psi p K^-$ *decays*, Phys. Rev. Lett. **117** (2016) 082002

[58] R. Aaij et al. (LHCb Collaboration), *Evidence for exotic hadron contributions to* $\Lambda_b^0 \to J/\psi p \pi^-$ *decays*, Phys. Rev. Lett. **117** (2016 082003 [Addendum: Phys. Rev. Lett. 117, no.10, 109902 (2016)]

[59] B. Pal et al (BELLE Collaboration), *Search for* $\Lambda_c^+ \to \phi p \pi^0$ *and measurements of* $\Lambda_c^+ \to K^-\pi^+ p\pi^0$ *decays*, arXiv: 1707.00089

[60] E. Oset and A. Ramos, *Dynamically generated resonances from the vector octet-baryon octet interaction* Eur. Phys. J. A **44**, 445 (2010)

[61] C. Zhang, G.X. Pei for the BEPCII Team, *BEPCII - the second phase construction of Beijing electron positron collider*, Proc. of 2005 Particle Accelerator Conference, Knoxville, Tennesse (2005) 131-135

[62] BESIII Collaboration, *The construction of the BESIII experiment*, Nucl. Instr. Meth. A **598** (2009) 7-1100000

[63] <http://bes3.ihep.ac.cn/talk/talks/phipsi09b_mhx.pdf>

[64] <https://phys.org/news/2016-04-bepcii-luminosity-world-11033cm2s.html>

[65] X.F. Li, Q. Ji, L. Wang, L.F. Zheng, *Design and cooling of BESIII beryllium beam pipe*, Nucl. Instr. and Meth. A **585** (2008) 40-47

[66] BESIII Collaboration, *BESIII Preliminary Design Report*, 2004 <http://bes.ihep.ac.cn/bes3/design05/design/design1.htm>

[67] T. Ning et al., Plasma Sci. Technol. 7 (5) (2005) 3065 (Oct).

[68] D.G. Cassel et al., Nucl. Instr. and Meth. A (1986) 325.

[69] L.H. Wu, High Energy Physics Nucl. Phys. 29 (5) (2005) 476 (in Chinese)

[70] M. Savrié, M.Y. Dong, internal BESIII note.

[71] F. Sauli, *GEM: a new concept for electron amplification in gas detector*, Nucl. Instr. and Meth. A **386** (1997) 531-534.

[72] S. Bachmann et al., *Discharge studies and prevention in the gas electron multiplier (GEM)*, Nucl. Instr. and Meth. A **479** (2002) 294

[73] M. Alexeev et al., *Development and Test of a* μTPC *Cluster Reconstruction for a Triple GEM Detector in strong Magnetic Field*, Conference RECORD, Nuclear Symposium and Medical Imaging Conference (NSS/MIC) IEEE (2016)

[74] A. Amoroso et al., *A cylindrical GEM detector with analog readout for the BESIII experiment*, Nucl. Instr. and Meth. A **824** (2016) 515-517

[75] S. Balla et al., *The cylindrical GEM detector for the KLOE-2 Inner Tracker*, JINST **9 C01014** (2014)

[76] http://www.rohacell.com/product/rohacell/en/about/pages/default.aspx

[77] M.D. Da Rocha Rolo et al., *A custom readout electronics for the BESIII CGEM detector*

[78] D. Bettoni et al., *A Cylindrical GEM detector with analog readout for the BESIII experiment*, PoS(TIPP2014) 292 (2014)

[79] David W.G.S. Leith, Nucl. Instr. and Meth. A **494** (2002) 389

[80] M. Artuso et al., Nucl. Instr. and Meth. A **461** (2001) 545

[81] J. Zhang et. al, Nucl Instr. and Meth. A **540** (2005) 102.

[82] D.M. Asner et. al, *Physis at BES-III*, arXiv: 0809.1869v1

[83] J.J. Aubert et. al (E598 Collaboration), *Experimental Observation of a Heavy Particle J*, Phys. Rev Lett **33** (1974) 1404-1406

[84] J.E. Augustin et al. (SLAC-SP-017 Collaboration), *Discovery of a Narrow Resonance in e^+e^- Annihilation*, Phys. Rev. Lett. 33 (1974) 1406-1408

[85] G.S. Abrams et al., *The Discovery of a Second Narrow Resonance in e^+e^- Annihilation*, Phys. Rev. Lett **33** (1974) 1453-1455

[86] M. Ablikim et al. (BESIII Collaboration), *Branching fraction measurements of $\psi(3686)$ radiative transitions*, Phys. Rev. D **96**, (2017) 032001

[87] M. Ablikim et al. (BESIII Collaboration), *Study of J/ψ and $\psi(3686) \to \Lambda\bar{\Lambda}$ and $\Sigma_0\bar{\Sigma}^0$ decays*, Phys. Rev. D **95** (2017) 052003

[88] M. Ablikim et al. (BESIII Collaboration), *Observation of $\psi' \to e^+e^-\chi_{cj}$ and $\chi_{cj} \to e^+e^-J/\psi$*, Phys. Rev. Lett. **118** (2017) 221802

[89] M. Ablikim et al. (BESIII Collaboration), *Measurements of absolute hadronic branching fraction of Λ_c^+ baryon*, Phys. Rev. Lett **116**, 052001 (2016)

[90] M. Ablikim et al. (BESIII Collaboration), *Observation of $\Lambda_c^+ \to nK_S^0\pi^+$*, Phys. Rev. Lett. **118**, 112001 (2017)

[91] G. Ecker, *Status of chiral perturbation theory for light mesons*, PoS CD15 (2015) 011

[92] D. Schildknecht, *Vector Meson Dominance*, Acta Phys. Plon. B **37** 595-608

[93] D. Mohler, *Recent results on the meson and baryon spectrum from lattice QCD*, EPJ Web Conf. **137** (2017) 05018

[94] M. Ablikim et al. (BESIII Collaboration), *An amplitude analysis of the $\pi^0\pi^0$ system produced in radiative J/ψ decay*, Phys. Rev. D **92**, 052003 (2015)

[95] M. Ablikim et al. (BES Collaboration), *Observation of a resonance X(1835) in $J/\psi \to \gamma\pi^+\pi^-\eta'$*, Phys. Rev. Lett. **95** 262001 (2005)

[96] M. Ablikim et al., *Confirmation of X(1835) and observation of resonances X(2120) and X(2370) in $J/\psi \to \gamma\pi^+\pi^-\eta'$*, Phys. Rev. Lett. **106** 072002 (2011)

[97] J.Z. Bai et al (BES Collaboration), *Observation of a Near-Threshold Enhancement in the $p\bar{p}$ Mass Spectrum from Radiative $J/\psi \to \gamma p\bar{p}$ Decays*, Phys. Rev. Lett **91**, 022001 (2003).

[98] M. Ablikim et al. (BESIII Collaboration), *Observation of a $p\bar{p}$ mass threshold enhancement in $\psi' \to \pi^+\pi^- J/\psi(J/\psi\gamma p\bar{p})$ decay*, Chyn. Phys. C **34**, 421 (2010)

[99] J.P. Alexander et al. (CLEO Collaboration), *Study of $\psi(2S)$ decays to $\gamma p\bar{p}$, $\pi^0 p\bar{p}$ and $\eta p\bar{p}$, and search for $p\bar{p}$ threshold enhancements*, Phys. Rev. D **82** 092002 (2010)

[100] M. Ablikim et al (BESIII Collaboration), *Observation of an Anomalous Line Shape of the $\eta'\pi^+\pi^-$ Mass Spectrum near the $p\bar{p}$ Mass Threshold in $J/\psi \to \gamma\eta'\pi^+\pi^-$*, Phys. Rev. Lett **117**, 042002 (2016)

[101] M. Ablikim et al. (BESIII Collaboration), *Observation of Dalitz decay $\eta' \to \gamma e^+e^-$*, Phys. Rev. D **92** 012001 (2015)

[102] M. Ablikim et al. (BESIII Collaboration), *Measurement of the Matrix Elements for the decays $\eta \to \pi^+\pi^-\pi^0$ and $\eta/\eta' \to \pi^0\pi^0\pi^0$*, Phys. Rev. D **92**, 012014 (2015)

[103] M. Ablikim et al. (BESIII Collaboration), *Precision measurements of the mass of the τ lepton*, Phys. Rev. D **90**, 012001 (2014)

[104] M. Arkani-Hamed, D.P. Finkbeiner, T.R. Slatyer, and N. Weiner, *A Theory of Dark Matter* Phys. Rev. D **79** 015014 (2009)

[105] B. Holdom, *Two U(1)'s and Epsilon Charge Shifts*, Phys. Lett. B **166** (1986) 196-198

[106] M. Ablikim et al. (BESIII Collaboration), *Dark Photon Search in the Mass Range Between 1.5 and 3.4 GeV/c^2*, arXiv: 1705.04265 [hep-ex]

[107] M. Pospelov, *Secluded U(1) below the weak scale*, Phys. Rev. D **80** (2009) 095002

[108] S. Agostinelli et al (GEANT4 Collaboration), Nucl. Instrum. Methods Phys. Res. Sect. A **614**, 345 (2010)

[109] R.G. Ping, *An exclusive event generator for e^+e^- scan experiment*, Chin Phys. C **32**, 599 (2008)

[110] D.J. Lange, Nucl. Instrum. Methods Phys. Res. Sect. A **462**, 152 (2001)

[111] Y.K. Henh, IEEE Nucl. Sci. Symp. Conf. Rec. (2007) 53

[112] BESIII Analysis Memo 254 (internal note).

[113] A. Esposito, A. Pilloni, A.D. Polosa., *Multiquark Resonances*, arXiv: 1611.07920

[114] R.F. Lebed, R.E. Mitchell, E.S. Swanson, *Heavy-Quark QCD Exotica*, arXiv: 1610.04528

[115] M. Voloshin, *Charmonium*, Prog. Part. Nucl. Phys. **61** (2008) 455

[116] S. Dubynskiy, M. Voloshin, *Hadro-Charmonium*, Phys. Lett. **B666** (2008) 334

[117] A. Manohar, M. Wise, *Heavy Quark Physics*, Cambr. Monogr. Part. Phys. Nucl. Phys. Cosmol. **10** (2000) 1

[118] L. Maiani, F. Piccinini, A.D. Polosa and V. Riquer, *New look at scalar mesons*, Phys. Rev. Lett. **93** (2004)

[119] H.-X. Chen, L. Maiani, A.D. Polosa, and V. Riquer $Y(4260) \to \gamma X(3872)$ *in the diquarkonium picture*, Eur. Phys. J. **C75** (2015) 550

[120] C. Meyer, E. Swanson, *Hybrid Mesons*, Prog. Part. Nucl. Phys. **82** (2015), 21.

[121] S.M. Ryan, *Hadron spectroscopy from lattice quantum chromodynamics*, EPJ Web Conf. **130** (2016) 01002

[122] S.-L. Zhu, *The Possible interpretations of* $Y(4260)$, Phys. Lett. **B625** (2005) 212

[123] F.E Close and P.R. Page, *Gluonic charmonium resonances at BaBar and Belle?*, Phys. Lett. **B628** (2005) 215

[124] E. Kow and O. Pene, *Suppressed decay into open charm for the* $Y(4260)$ *being an hybrid*, Phys. Lett. **B631** (2005) 164

[125] E. Wigner, *On the Behaviour of Cross Sections Near Thresholds*, Phys. Rev. **73** (1948) 1002

[126] A. Baz', L.Okun', *On the* Λ*-Hyperon Creation Cross Section Near the* Σ*-Hyperon Creation Threshold* Soviet. Phys. JETP **8** (1959) 757

[127] M. Naunenberg, A. Pais, *Correlations between Cusps in Differential Cross Sections and in Polarizations*, Phys. Rev. **123** (1961) 1058.

[128] V. Kubarovsky, M.B. Voloshin, *Formation of hidden-charm pentaquarks in photon-nucleon collisions*, Phys. Rev. **D92** (3) (2015) 031502

[129] F.-K. Guo, U.-G. Meissner, W. Wang, Z. Yang, *How to reveal the exotic nature of the* $P_c(4450)$, Phys. Rev. **D92** (7) (2015) 071502

[130] M. Mikhasenko, *A triangle singularity and the LHCb pentaquark*, arXiv:1507.06552

[131] H.-X. Chen, W. Chen, X. Liu, T.G. Steele, S.-L. Zhu, *Towards exotic hidden-charm pentaquarks in QCD*, Phys. Rev. Lett **115** (17) (2015) 172001

[132] K. Azizi, Y. Sarac, H. Sundu, *Analysis of* $P_c^+(4380)$ *and* $P_c^+(4450)$ *as pentaquark states in the molecular picture with QCD sum rules*, Phys. Rev. **D95** (9) (2017) 094016

[133] L. Maiani, A.D. Polosa, V. Riquer, *The new pentaquarks in the diquark model*, Phys Lett. **B749** (2015) 289-291.

[134] R. Chen, X. Lliu, X.-Q. Li, S.-L. Zhu, *Identifying exotic hidden-charm pentaquarks*, Phys. Lett. **115** (13) (2015) 132002